CONTROLLABLE THREE-DIMENSIONAL STRAIN, MICROSTRUCTURE, AND FUNCTIONALITIES IN SELF-ASSEMBLED NANOCOMPOSITE THIN FILMS

by

Xing Sun

A Dissertation

Submitted to the Faculty of Purdue University

In Partial Fulfillment of the Requirements for the degree of

Doctor of Philosophy

School of Materials Engineering

West Lafayette, Indiana

August 2019

THE PURDUE UNIVERSITY GRADUATE SCHOOL
STATEMENT OF COMMITTEE APPROVAL

Dr. Haiyan Wang, Chair
School of Materials Engineering
Dr. Maria Okuniewski
School of Materials Engineering
Dr. John Blendell
School of Materials Engineering
Dr. Xinghang Zhang
School of Materials Engineering

Approved by:
Dr. David Bahr
Head of the Graduate Program

Dedication to my husband and my parents

ACKNOWLEDGMENTS

I would like to strongly express my sincere gratitude to my advisor, Dr. Haiyan Wang for her great guidance and unconditional support in my PhD study, research and also my personal life. Her passion and optimistic attitudes inspire me to move forward and pursue high-quality of research. She always encourages me not only to work hard and more importantly to work smart. She taught me how to do research effectively and how to transfer the problems into breakthroughs. Her patience and faith accompanied me to go through the struggling days of my research and overcome the difficulties on my pathway. Dr. Wang is not only the guide light of our research and also a young mother of the group. We have a big group of twenty students who are closely bonded like a family because of her. She truly cares about us and organizes entertainment activities to release our stress from the final exams. She has a generous kind heart and set a great role model for us to contribute to the community and society. I feel so lucky to be her student and part of the group.

I want to thank my committee members, Dr. Xinghang Zhang, Dr. John Blendell, and Dr. Maria Okuniewski for serving on my dissertation committee, encouraging me, and giving great suggestions on my research projects. I also thank Dr. Neil Dilley from Birck nanotechnology center for his training and help on PPMS and MPMS. I would like to send my special appreciation to Dr. Hongcai Zhou at Texas A&M University for his full support and belief.

I thank my collaborators Dr. Judith MacManus-Driscoll at University of Cambridge and Dr. Ping Lu at Sandia National Laboratories for the fruitful collaboration and great help on TEM.

I would like to send my special appreciation to my teammates: Dr. Jijie Huang, Dr. Jie Jian, Dr. Meng Fan, Han Wang, Xingyao Gao, Bruce Zhang, Megan Kephart, Robynne Paldi, Matias Kalaswad and Di Zhang for their kind help and friendship. I also want to thank all my friends and colleagues at Texas A&M University and Purdue University.

I cannot thank enough my parents, Ms. Xia Zhang and Mr. Guoqiang Sun, and my husband Qiang Li, for their unconditional love, sacrifice and support. I am so blessed to have them!

TABLE OF CONTENTS

LIST OF TABLES

LIST OF FIGURES

ABSTRACT

Author: Sun, Xing. PhD
Institution: Purdue University
Degree Received: August 2019
Title: Controllable Three-dimensional Strain, Microstructure, Functionalities in Self-assembled Nanocomposite Thin Films
Committee Chair: Haiyan Wang

Vertically aligned nanocomposite (VAN) configuration has been recognized as the state-of-the-art architecture in the complex oxide epitaxial thin films, which are constructed by two immiscible phases simultaneously and vertically growing on a given substrate and forming various columnar microstructures, such as nanopillars embedded in matrix, nanomaze, and nanocheckboard. Due to its architectural features, VAN structure enables a powerful control on the multifunctionalities via vertical strain engineering, microstructural variations, and interfacial coupling. It provides flexibility in complex oxide designs with various functionalities (e.g., electrical, magnetic, optical, etc.), as well as a platform to explore the correlations between strain, microstructure, and multifunctionalities of the nanocomposite thin films.

In this dissertation, integrated VAN systems with multilayer configuration have been constructed as a new three-dimensional (3D) framework, e.g., inserting 1-3 layers of CeO_2 (or LSMO) interlayers into the $La_{0.7}Sr_{0.3}MnO_3$ (LSMO)-CeO_2 VAN system and forming 3D interconnected CeO_2 (or LSMO) skeleton embedded in LSMO matrix. This new VAN 3D framework enables both lateral and vertical strain engineering simultaneously within the films and obtains highly enhanced magnetotransport properties, such as the record high magnetoresistance (MR) value of ~51-66%, compared with its VAN single layer counterpart. In order to demonstrate the flexibility of this design, other systems such as 3D ZnO framework embedded in LSMO matrix have been constructed to explore the thickness effects of the ZnO interlayers on the magnetotransport

properties of the LSMO-ZnO system. The maximum MR value is obtained at the ZnO interlayer thickness of ~2 nm, which enables the optimal magnetoresistance tunneling effect. Meanwhile, the significance of the interlayer selection in the microstructure and magnetoresistance properties of the LSMO-ZnO system has been investigated by varying the interlayer materials yttria-stabilized zirconia (YSZ), CeO_2, $SrTiO_3$, $BaTiO_3$, and MgO. The formed 3D heterogeneous framework provides a new dimension to tailor the microstructure, strain and functionalities within the films. Moreover, a new strain engineering approach with engineered tilted interfaces has been demonstrated by multilayering different VAN layers with various two phase ratio and creating a hybrid nanodumbbell structure within the LSMO-CeO_2 VAN thin films. The nanodumbbell structure accomplishes a more efficient strain engineering and exhibits highly enhanced magnetic and magnetoresistance properties, compared with its VAN single layer and interlayer counterparts. These examples presented in the thesis demonstrate the flexibility and potential of 3D strain engineering in complex VAN systems and a higher level of property control, coupled with unique microstructures and interfaces. Beyond perovskites, these 3D designs can be extended to other material systems for a broader range of applications, such as energy conversion and storage related applications.

CHAPTER 1. INTRODUCTION

This chapter introduces the background, motivation and goals of the research in this dissertation. Strain engineering has been widely recognized as a powerful tool to modify crystal lattice and physical responses of complex oxide thin films. Recently, vertically aligned nanocomposite (VAN) structure has become the state-of-the-art research interest and enabled more efficient strain engineering, variable microstructure, and highly enhanced multifunctionalities of the complex oxide nanocomposite thin films.

1.1 Complex Oxide Thin Films

Functional complex oxide materials have brought an acceleration in development of the society and industry in the past decades, and play a critical role in both fundamental science studies and the future technologies. The complex oxide materials have exhibited a rich spectrum of enchanting functionalities, including chemical reactivity from active to inert, optical behaviors from UV to visible, electronic behaviors from superconducting to insulating, magnetic behaviors from ferromagnetic to antiferromagnetic, and dielectric behaviors from ferroelectric to piezoelectric. The richness in the functionalities of the complex oxides is due to their chemical and physical complexities, enabling that the complex oxides are heavily applied in environmental, medical, catalysis, electronic, and information fields.[1]

1.1.1 Overview of Complex Oxides

Consisting of one or more metal cations bonding with oxygen anions by typical ionic bonds, complex oxides encompass an astonishing array of crystal structures and exhibit diverse intriguing functionalities, such as electrical, magnetic, optical, catalytic, and more. These functionalities are

derived from the interplay between the metal and oxygen ions, orbital, charge, spin, degrees of freedom. These are quite sensitive to the bond length and angles in the complex oxides, which can be modulated through either the chemistry or the crystal structures. Complex oxides provide a great platform for the fundamental studies regarding the inorganic materials and solid matter physics, and also diverse ideal candidates for the application-oriented research in the advancement of the current technology.[2-5]

Complex oxides represent a quite broad and diverse range of functional metal oxides and can be classified according to different criteria. From the property perspective, complex oxides contain insulators, semiconductors, semimetals, superconductors, and more. From the metal ion species, complex oxides could accommodate only one type of metal ions (also called binary oxides) or more than one types of metal ions.

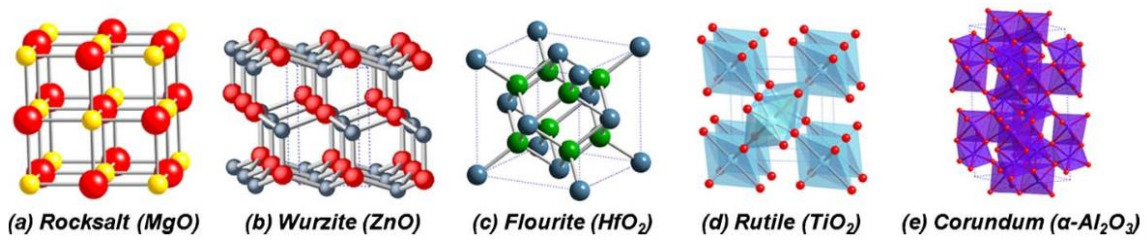

Figure 1.1 Schematic drawing of the following crystal structures:(a) rocksalt (MgO), (b) wurzite (ZnO), (c) fluorite (HfO_2), (d) rutile (TiO_2), and (e) corundum (Al_2O_3).[3]

Binary oxides are usually in the following forms—MO, MO_2, and M_2O_3 in which M represents metal ions. They have the crystal structures of rock salt, fluorite, wurtzite, rutile, and corundum as shown in Figure 1.1. The monoxides of rock salt structure (e.g., MgO, NiO, CaO, and MnO) have the metal cation and oxygen anion in octahedral coordination with strong ionic feature of the bonds, exhibiting large band gaps and insulating behaviors (Figure 1.1 (a)). But the monoxides of wurtzite structure such as ZnO are hexagonal and have the cations and anions in tetrahedral coordination and thus exhibit typical semiconducting behaviors as well as quite high

carrier mobility (Figure 1.1 (b)). In addition, like LaO, NbO, EuO, some monoxides MO also can reveal metallic, superconductive, and magnetic behaviors. As shown in Figure 1.1 (c) and (d), dioxides MO_2 usually have rutile (e.g., MoO_2, TiO_2 and WO_2) and fluorite (e.g., HfO_2, ZrO_2 and CeO_2) structures, corresponding to semiconducting and insulating behaviors, respectively. Most of trivalent oxides M_2O_3 have corundum or bixbyite structures and show insulating behaviors with strong ionic bonds, such as Al_2O_3, V_2O_3, Mn_2O_3 and La_2O_3 (Figure 1.1 (e)).[3, 5]

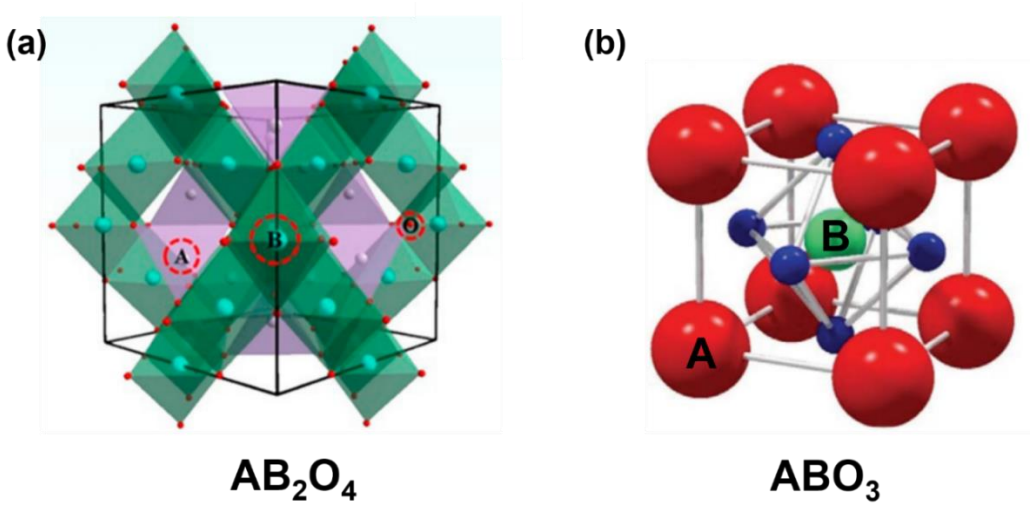

Figure 1.2 Schematic illustration showing the crystal structures of (a) spinel structure (AB_2O_4) and (b) perovskite structure (ABO_3).[5, 6]

For the complex oxides which accommodate more than one type of metal ions, spinel (AB_2O_4) and perovskite (ABO_3) are the two most common structures. With a formula of AB_2O_4 (A and B represent different types of metal ions), spinel structure consists of a FCC packing of oxygen ions and one-eighth of the tetrahedral interstices occupied by divalent and trivalent cations (Figure 1.2 (a)), such as $MgAl_2O_4$, $NiFe_2O_4$, and $CoFe_2O_4$. The materials of spinel structure demonstrate multiple functionalities including various electrical, magnetic, optical and catalytic properties. The practical performances of spinel materials can be easily tuned by precisely control the chemistry or crystal structures. Therefore, the spinel oxides have played a relatively significant

role in biotechnology, data storage, electronics, sensor, laser, energy conversion and storage system, and more fields.[2, 6]

As one of the most popular complex oxides, perovskite oxides have been deeply influencing our daily life and the advancements of science and technology in the past a few decades. Perovskite oxides have a chemical formula of ABO_3 (e.g., $SrTiO_3$, $CaTiO_3$, $BaTiO_3$, $BiFeO_3$, $LaMnO_3$, $La_{0.7}Ca_{0.3}MnO_3$, $La_{0.7}Sr_{0.3}MnO_3$, $SrRuO_3$, etc.), which is composed of A cations and corner-sharing BO_6 octahedral units with the B cation coordinated by six oxygen ions (Figure 1.2 (b)). The ABO_3 perovskite oxides have very large flexibility in chemistry and are able to allow a very large diversity of combinations of A and B cations with different oxidation states such as $A^{+2}B^{+4}O_3$, $A^{+3}B^{+3}O_3$, and $A^{+1}B^{+5}O_3$. Thus, perovskite oxides exhibit a broad span of impressive multifunctionalities including superconductive, half-metallic, piezoelectric, ferroelectric, ferromagnetic, multiferroic, catalytic, optical properties, and more. Moreover, perovskite oxides have relatively high sensitivity of the physical properties to the structural variations, and also exhibit excellent chemical/structural compatibility with other inorganic materials of different crystal structures. Therefore, perovskite oxides have been well studied as an ideal candidate for the investigations of strain tuning, interfacial coupling, defects and microstructural effects in fundamental materials science. They also play a dramatically essential role in the application-oriented research and provide more possibilities to customize their physical properties for the modern electric and magnetic devices.[3-5, 7-12]

1.1.2 From Bulk to Thin Films

The studies on the bulk functional oxide materials have been very mature and obtained a significant progress in property enhancement by tailoring the chemistry and microstructure of the materials. Moreover, to fulfill the requirements of device integration, thin film form of the

functional oxides is more suitable and flexible for multiple practical applications such as high-energy memories, spintronics, sensors, electromechanical system, fuel cells, batteries, etc. Therefore, increasing scientists and engineers have been endeavoring to study various types of thin films, such as polycrystalline, epitaxial, nanocomposite thin films, etc., and seeking the ideal candidates to optimize the ultimate performances of devices.[13, 14]

Compared with bulk form, thin films have exhibited many unbeatable priorities especially epitaxial thin films. For example, thin films are able to have different phases uniformly combined and mixed from atomic level, control the distribution of some domains or interfacial defects, achieve expected architectural designs, and precisely tailor the lattice couplings. These may not be accessible in bulk materials or necessarily affect the bulk properties. But they are quite beneficial to acceleration of understanding thin films at small scale and quite significant for the property enhancements in thin films. [13, 15, 16] Also, thin film form can modify the chemical and physical performances more efficiently, enable extra degrees of freedom in materials design than bulk materials, and provide more convenient pathways to achieve high-level materials control such as strain, microstructure and interfacial engineering.[17] For example, bulk materials cannot tolerate large strain which can be input into thin films and enables obvious lattice distortion for property improvements. There are a rich spectrum of strain engineering approaches, which will be discussed in detail in the later session. Moreover, the thin film growth can be customized according to the specific requirements, which helps to realize the researchers' original ideas and provides more opportunities for the various new electronics in practical applications.[4]

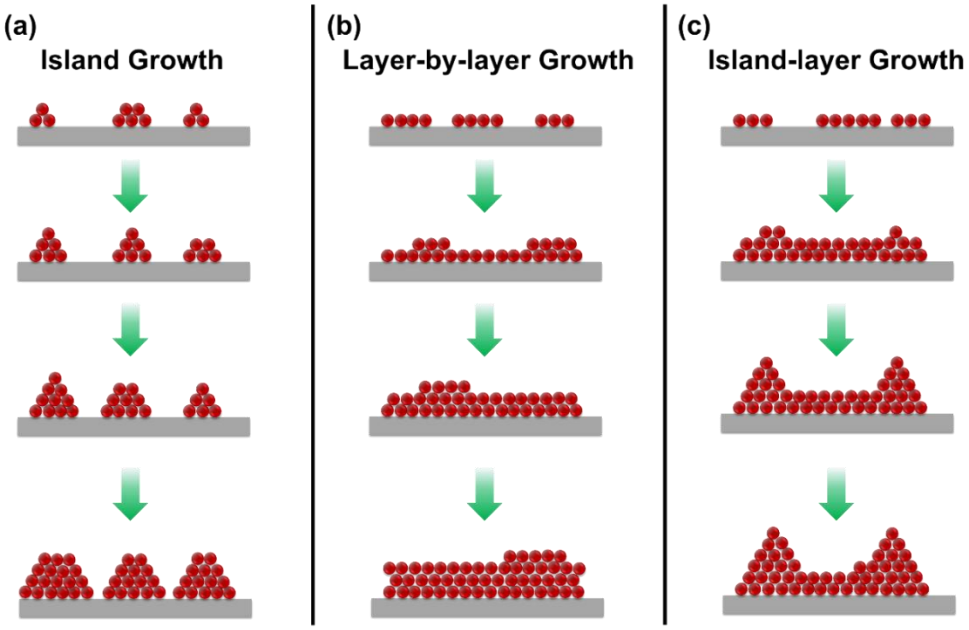

Figure 1.3 Schematic diagrams showing the three growth modes of thin films: (a) island growth (Volmer-Weber), (b) layer-by-layer growth (Frank-van der Merwe), and (c) island-layer growth (Stranski-Krastanov).

The thin film growth plays a dominant role in determining the crystal structure and ultimate performances of the resultant electronics. Figure 1.3 shows the three growth modes of thin films, which are island (Volmer-Weber) growth, layer-by-layer (Frank-Van der Merwe) growth, and island-layer (Stanski-Krastanov) growth, respectively. When the atoms or molecules of a film prefer bonding with the atoms (or molecules) of its own materials over substrate, the island growth mode occurs and has the film clusters accumulating together laterally and vertically into three-dimensional individual islands distributed on the substrate surface (Figure 1.3 (a)). When the film and substrate are different materials, the film usually grows into islands such as cobalt film grown on $SrTiO_3$ substrates.[18] When the bonding between the substrate and growing phase is much stronger than that between the film atoms (or molecules), the film clusters grow laterally into two-dimensional planar sheets covering the substrate surface and then stack on top of each other as shown in Figure 1.3 (b). This is the layer-by-layer growth mode. The island-layer growth mode is

a hybrid combination of the previous two growth modes, in which the formation of the three-dimensional islands become energetically favorable and dominates after the initial several layers of two-dimensional layer-by-layer growth (Figure 1.3 (c)). These different growth modes are driven by the competition of surface/interfacial energies between each phase and the ultimate effect is the minimization of the overall system energy.[3, 16, 18]

The nucleation process can be thermodynamically described by the following Young's equation[3, 19]:

$$cos\theta = \frac{\gamma_{s-v} - \gamma_{f-s}}{\gamma_{f-v}} \quad (1\text{-}1)$$

where γ_{s-v}, γ_{f-v}, and γ_{f-s} represent the surface energies of the substrate and film, and interfacial energy between substrate and film, respectively. θ corresponds to the wetting angle. As shown in Figure 1.4, when γ_{s-v} is larger than $(\gamma_{f-v} + \gamma_{f-s})$, the wetting angle θ is 0 and the film grows in layer-by-layer fashion. When γ_{s-v} is smaller than $(\gamma_{f-v} + \gamma_{f-s})$, the wetting angle θ is bigger than 0 and the film grows in island growth. In some cases of the layer-by-layer growth, with increasing film thickness, the enhanced supersaturation and accumulating strain energy result in the film growth mode switching to island growth. This corresponds to the island-layer growth mode.

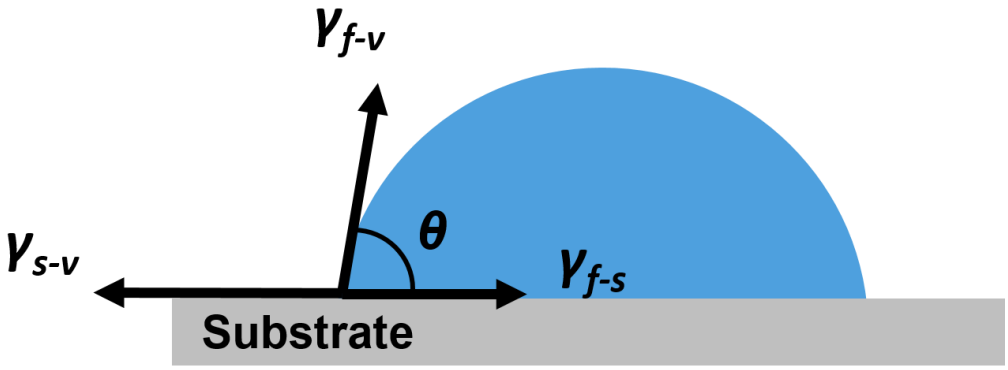

Figure 1.4 Schematic illustration describing a nucleation process of a film on a substrate with wetting angle θ. The γ term corresponds to surface/interfacial energies and the subscripts *s*, *f*, and *v* represent the substrate, film and vapor phases.

1.1.3 Perovskite Oxide Thin Films

As the most popular and significant class of complex oxides, perovskite oxides (ABO_3) have present an astonishing array of technologically significant functionalities, such as ferroelectricity, ferromagnetism, multiferroicity, metal-insulator transition, superconductivity, piezoelectricity, and electrochemical properties.[17, 20] These properties are enabled by the charge, spin, orbital, and lattice degrees of freedom as well as their interplay in the perovskite oxides, which are closely associated with the bond length, angles and the BO_6 octahedral building blocks.[5] As shown in Figure 1.5 (a), the perovskite oxide lattice is mainly constructed by the corner-sharing BO_6 octahedral units connected with each other in a simple cubic fashion. Each BO_6 octahedral unit accommodates one metal cation B coordinated with six oxygen ions, and is recognized as the dominant functional building blocks of the perovskite oxides. A minor change in the chemistry and geometric structure (e.g., size, shape and connectivity) of the BO_6 octahedral units can lead to profound influence on the physical performances of the perovskite materials, such as magnetic, electric, thermal, optical, and mechanical properties (Figure 1.5 (b)).[8] Therefore, control on structural distortion and chemistry of the perovskite oxide lattices is the most efficient path to the functionality tuning and improvements. With the chemistry of ABO_3 settled, the structural distortion is quite hard to accomplish in bulk form. However, the thin film form provides more opportunities to achieve the desired performances of perovskite oxides by lattice distortion especially epitaxial thin films. As the epitaxial thin film growth is a thermodynamically and kinetically controlled non-equilibrium process in which the lattice arrangement can be controlled with atomic-scale precision. Many approaches have been studied to achieve efficient structural control in perovskite thin films, such as strain engineering, interface engineering, microstructural control and more. They are able to efficiently tailor the functional performances of perovskite

oxide thin films and even bring unprecedented properties which are not found in their bulk form.[8, 21-24]

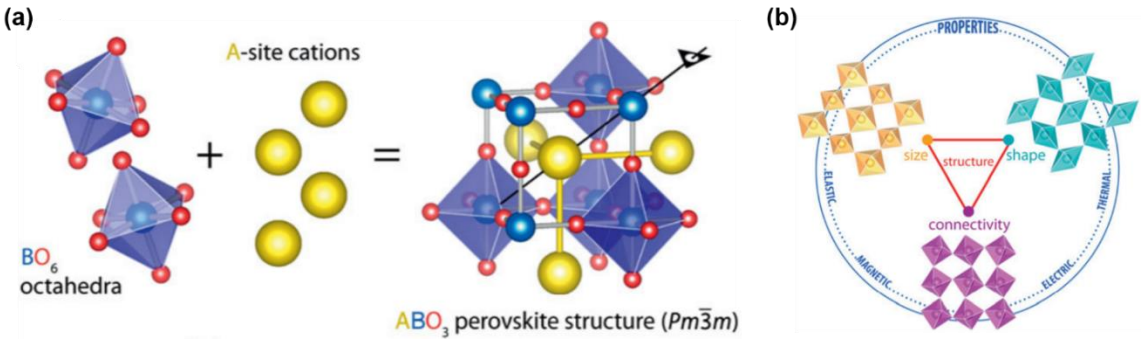

Figure 1.5 (a) Schematic illustration of the perovskite oxide (ABO_3) crystal structure. (b) The interplay between the structural distortions of the octahedral unit BO_6 (such as size, shape and connectivity) and the functional properties of the perovskite oxides.[8]

1.2 Functionalities of Perovskite thin films

The perovskite oxide thin films have been at the heart of the scientific community due to its enormous value in the fundamental materials science study and also the technological significance in the electronic devices. For fundamental research interest, perovskite oxides have excellent chemical/structural tolerance, high sensitivity of structural distortion to physical performances, and multiple tunabilities such as strain, interface, and architecture. In technological and practical aspect, the perovskite oxide thin films have exhibited an amazing variety of interesting functionalities, including ferromagnetism, ferroelectricity, multiferroicity, superconductivity, ion conductivity, piezoelectricity, electriochemical properties and more. All those intriguing functionalities enable the perovskite oxide thin films outstanding candidates for the next generation of technological devices, e.g., transducers, magnetic sensors, information storage systems, spintronics, and more.[13, 15, 25, 26]

Within such a rich spectrum of properties in the perovskite oxide thin films, this session mainly focus on the magnetoresistance property discussion. Magnetoresistance (MR) is the

relative electrical resistance/resistivity variation of a material before and after an applied external magnetic field. This property have enabled the ferromagnetic perovskite oxides well applied in data storage, spintronics, and magnetic sensors. The magnitude of MR in industry was quite low (~2%) at room temperature for the anisotropic magnetoresistive materials. Many researchers have delivered inspiring studies to the scientific research community. Tunneling magnetoresistance was revealed in a magnetic tunnel junction (MTJ), in which two ferromagnetic layers are isolated by a thin insulating barrier layer such as MgO and Al_2O_3.[27-29] Giant magnetoresistance (GMR) of ~ 50% was reported in metal multilayer stacked nanostructures at low temperature.[30] Colossal magnetoresistance (CMR) effect was reported in perovskite oxides with a resistivity change of nearly 100% under few teslas. However, the requirement of a large external magnetic field up to several teslas hinders the practical application of CMR. Very recently, the low field magnetoresistance (LFMR) effect, driven by the grain boundaries in perovskite oxides, has drawn considerable interest due to large MR effect at a magnetic field lower than one tesla.[31]

1.2.1 Giant magnetoresistance

Giant magnetoresistance (GMR) effect was first discovered in 1988 in a metallic ferromagnetic/nonmagnetic (Fe/Cr) multilayer nanostructure, where magnetic Fe thin layers are separated by of non-magnetic Cr layers.[30] This giant magnetoresistance is induced by the spin-dependent transmission of the conduction electrons across the thin Cr layers between Fe layers. The magnetoresistance magnitude heavily depends on the Cr layer thickness—higher Cr layer thickness reduces the magnetoresistance value. This effect was subsequently found to occur in a number of magnetic multilayer systems and the related devices have been widely commercialized.[32-34]

The GMR effect needs to flip the relative magnetization orientations or directions between adjacent magnetic layers. The GMR effect requires the layer thickness to be lower than the mean free path of the electrons.[34] There are two types of conduction electrons: those whose spin is parallel to the local magnetization and those whose spin is antiparallel, corresponding to the electrical resistance $R_{\uparrow\uparrow}$ and $R_{\uparrow\downarrow}$ respectively. The GMR value can be calculated by the following equation,

$$GMR = {(R_{\uparrow\downarrow} - R_{\uparrow\uparrow})}/{R_{\uparrow\uparrow}} \times 100\% \quad (1\text{-}1)$$

1.2.2 Tunneling magnetoresistance

Tunneling magnetoresistance (TMR) is discovered in the multilayer structures where a relatively thin insulating layer (e.g., CeO_2, MgO, Al_2O_3 and $SrTiO_3$) separates two ferromagnetic layers (e.g., Fe and Co).[28, 35] Those insulating layers are called magnetic tunneling junctions (MTJ). The insulating layers have to be very thin (<5 nm) so that the electrons are able to tunnel through the barrier under the application of a bias voltage. The TMR effect results from the spin-dependent tunneling phenomena. In a MTJ structure, the tunneling current depends on the magnetizations orientation between the two ferromagnetic layers, which can be switched by an external magnetic field. When the magnetization orientations of the two ferromagnetic layers are parallel, it is easier for the electrons to tunnel through the insulating barrier than the case when the magnetization orientations are antiparallel. Thus, the junction is switched between low and high electrical resistances. The TMR value is calculated by the following equation,

$$TMR = {(R_{ap} - R_p)}/{R_p} \times 100\% \quad (1\text{-}2)$$

R_{ap} and R_p represent the electrical resistance when the magnetization directions are anti-parallel and parallel, respectively. Recently MgO has been used as the tunneling barrier with several

thousand percent of TMR in Fe/MgO/Fe sandwiches structures. In addition, a MTJ with Fe/MgO/FeCo (001) have been experimentally demonstrated of showing a significant TMR in this structure. Further enhancement of TMR has been reported to be ~600% in CoFeB/MgO/CoFeB junctions. As mentioned above, half-metal perovskite oxides are ferromagnetic such as LSMO and LCMO, which can be used in the metal-oxide hybrid based MTJs.

1.2.3 Colossal magnetoresistance

Colossal magnetoresistance (CMR) is involved with a phase transition from ferromagnetic to paramagnetic. The CMR compound is generated from the parent perovskite oxide $LaMnO_3$. When La ions are substituted by Ca or Sr ions, the resultant oxide compound transfers from a high-temperature paramagnetic insulator to a low-temperature ferromagnetic metal. Relatively high MR value is observed close to the transition temperature. The perovskite oxides with this behavior have been widely used in magnetic recording systems.[36]

In the MnO_6 octahedra of $LaMnO_3$, the Mn ion is surrounded by the six nearest-neighbor oxygen ions. These highly symmetric ideal cubic MnO_6 octahedra induce cubic crystal fields for Mn ions. The Mn^{3+}-O-Mn^{3+} chains in $LaMnO_3$ result in antiferromagnetic coupling and the strong electronic repulsion in $LaMnO_3$ result in the insulating nature. When Mn^{4+} ions is introduced via hole doping. The electrons in e_g orbitals will be delocalized and hop around. The e_g orbitals of Mn^{3+} are overlapped with O_{2p} orbitals and e_g electron could hop to the unoccupied e_g orbitals of Mn^{4+} through the O_{2p} orbitals. Mn^{3+}-O-Mn^{4+} with both electrons in t_{2g} orbitals spin up. The electron in the e_g orbitals of Mn^{3+} with spin up could hop to the orbitals of O_{2p}, which only has one down spin. It can be seen that a hopping process of the electron in the e_g orbitals with Mn^{3+}-O-Mn^{4+} configuration. Different from its mother materials $LaMnO_3$, doping by Ca or Sr on La sites will produce mobile holes in the perovskite oxides. CMR can be well explained by the double-exchange

interaction in conjunction with Jahn-Teller effect. Large CMR is usually observed at the temperatures close to the T_{MI} and T_c of the materials.[36]

1.2.4 Low-field magnetoresistance

In the CMR effect of perovskite oxides, the requirement of large external magnetic field prevents their further applications. Therefore, people started trying to search alternative pathways to further intensify the CMR effect. Later, large magnetoresistance at relative low magnetic field was discovered in doped $LaMnO_3$ thin films (e.g., LCMO and LSMO).

The spin-dependent scattering of polarized electrons at the grain boundaries serves as pinning centers for the magnetic domain walls, which is mainly used to explain the LFMR phenomena. Later, it was found that the LCMO or LSMO single crystal and epitaxial films only display CMR effect at large magnetic fields. Their MR responses at low magnetic field were weak. However, the polycrystalline LCMO or LSMO exhibit strong MR effect at very low magnetic field. Thus the grain boundaries in the polycrystalline is responsible for the LFMR effect. The LFMR is calculated by the equation below,

$$LFMR = {(R_0 - R_H)}/{R_0} \times 100\% \quad (1\text{-}3)$$

where R_0 and R_H correspond to the electrical resistances before and after the application of external magnetic field, respectively. LFMR effect can be further improved by addition of different secondary phase. Many materials have been incorporated into composites to enhance the LFMR including metals, semiconductors, and insulators.

1.3 Strain Engineering

1.3.1 Overview of Strain

To fulfill the rapidly growing demands of the current and future technologies, some researchers are attempting to create brand-new materials through chemistry. Others are exploring the deepest potentials within the well-known materials and doing their best to improve the performances of the materials in practical applications. Strain engineering has been systematically investigated for years and well recognized as a relatively efficient approach to tailor the structures and physical responses in a rich variety of materials.

Strain is described as the structural deviation of the matter from its original state. In crystalline thin films, strain corresponds to the lattice distortion or the relative displacement compared with its ideal bulk lattice or the reference state. It can be generated by the mechanical, chemical, electrical, magnetic, and other forces from the surrounded crystals.[37] Strain is achieved through interfacial coupling in thin films, which could be compressive or tensile. Different strains represent different lattice distortions, bond length and angles, defects and stoichiometry, which affect the physical performances of the materials profoundly. Thin films can accommodate much larger strain than the bulk counterparts and exhibit more obvious strain engineering effect on the physical properties.

Multiple approaches have been reported to achieve strain engineering, such as mechanical stretching/bending, helium implantation, and lattice mismatch.[38-42] The mechanical operations (e.g. stretching, bending, buckling, etc) are usually used to strain the two-dimensional materials such as graphene and transition metal dichalcogenides (e.g. MoS_2), and modulate their electronic structure as well as their optoelectronic performances for the future flexible electronics.[39, 43] Compared with helium implantation, lattice mismatch induced strain engineering is a much more

popular and convenient way to strain complex oxide materials and obtain highly improved physical properties, or even unprecedented performances.[8, 40, 44] Multiple physical properties have been demonstrated to be efficiently manipulated by strain engineering of lattice mismatch induced, including super conductivity, ionic conduction, magnetic anisotropy, magnetoresistance, ferroelectricity, and more.[45] Strain engineering of lattice mismatch has been accomplished by epitaxial in core-shell nanostructures and epitaxial thin films.[46-48] This work mainly focus on the epitaxial thin films.

In heteroepitaxial films, the biaxial strain of the film is generated due to the coherent growth and the lattice parameter difference between substrate and film. This biaxial strain is calculated by equation (1-4),

$$\varepsilon = \frac{a_s - a_f}{a_f} \times 100\% \quad (1\text{-}4)$$

where a_s and a_f are the bulk lattice parameter of the substrate and film, respectively. In addition, the different thermal expansion coefficients between substrate and film also can impose extra strain onto the film during the cooling-down process to room temperature.[49] If the biaxial strain $\varepsilon \approx 0$, it means either homoepitaxy or heteroepitaxial film having a perfect lattice match with the substrate. For most of heteroepitaxial films the biaxial strain is usually in the range from -7% to +7%, which is so large that the corresponding bulk counterpart cannot tolerate. If the strain is too large or the film thickness is over the critical thickness (around tens of nanometers), dislocation defects become energetically favorable to reduce the whole system energy. The unintentional defects are usually detrimental to the physical performances of the films and limit their further applications in real devices.

If the film and substrates are not simple cubic structure or the film-substrate lattice difference is too large ($|\varepsilon|$>7%) to accommodate lattice mismatch along the interfaces, domain

mismatch is more favored. In this case, m unit cells of the film phase couple with n unit cells of the substrate. The strain on the film is calculated as equation (1-5)

$$\varepsilon = \frac{n \times a_s - m \times a_f}{m \times a_f} \times 100\% \quad (1\text{-}5)$$

where a_s and a_f correspond to the bulk lattice parameters of the substrate and film. m and n are integers. For example, when LSMO and CeO_2 lattices are coupled together and form vertical interface, the interfacial relation is theoretically estimated to be either 3-2 or 4-3 between LSMO and CeO2 unit cells as shown in Figure 1.6 (a). In fact, the TEM and its fast-Fourier filted images demonstrate that both of 3-2 and 4-3 relations occur and alternates periodically, leading to the overall domain mismatch relation between LSMO and CeO_2 is 7-5 (Figure 1.6 (b-d)).[50] The domain mismatch coupling has been observed not only along the oxide-oxide interfaces (such as TiO_2-Ti_2O_3, ZnO-Al_2O_3 and LSMO-ZnO) and also the nitride-related interfaces (such as TiN-Si and AlN-Si).[51, 52] Those scenarios of domain mismatch are resulted from the large unrelaxed strain energy of 1-1 lattice mismatch and minimization of the overall system energy. Domain mismatch is also favored when the crystal structures of two phases are not similar such as perovskite-spinel composite systems.[52]

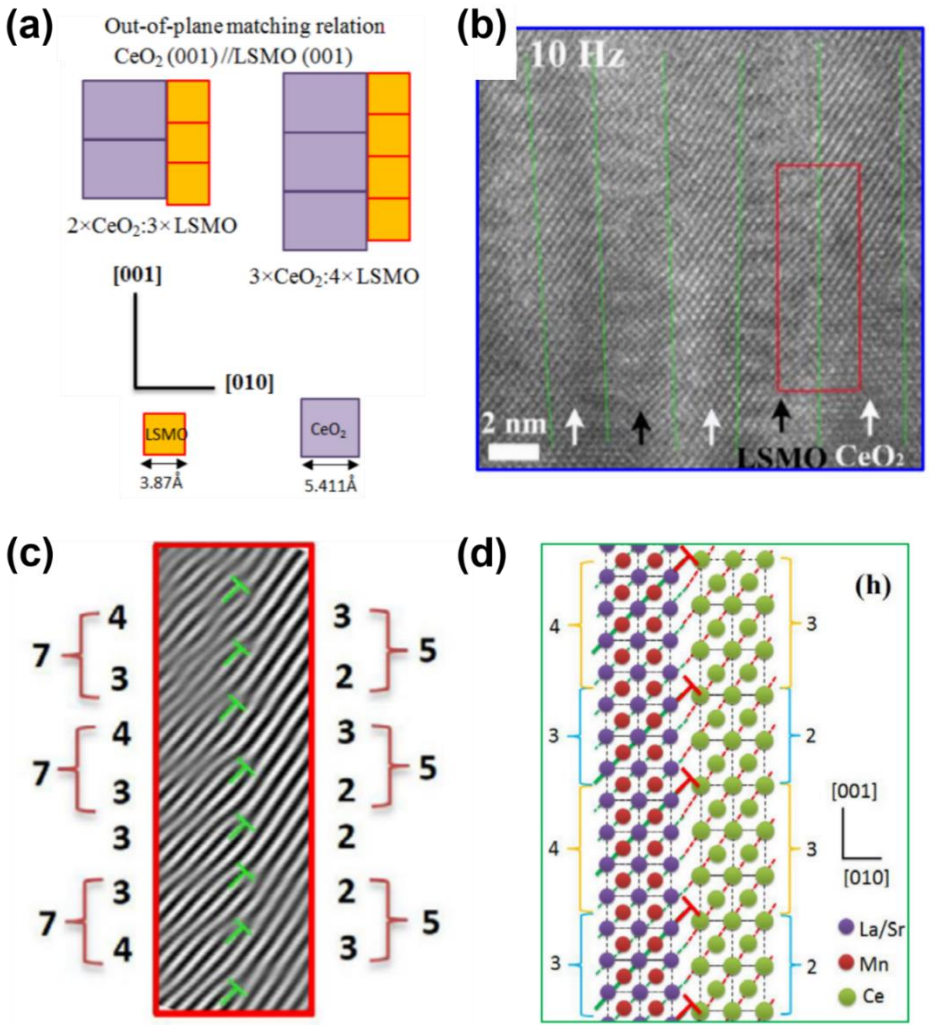

Figure 1.6 (a) Schematic illustration of domain mismatch relation along vertical LSMO-CeO_2 interface. (b) Cross-sectional TEM image of LSMO-CeO_2 nanocomposite thin film. (c) Fast-Fourier filtered image of the rectangular region marked by the red frame in (c), showing the domain mismatch relation of 5-7 between CeO_2 and LSMO unit cells. (d) Crystallographic drawing of the domain mismatch relation of (c).[50]

The strain engineering has been well acknowledged as a powerful tool to tailor the physical responses of perovskite oxide thin films, including superconductive, ferromagnetic, ferroelectric, and multiferroic properties since the strain not only adjusts the crystal structure of the perovskite oxide thin films and also reconstruct the spin, charge, and orbitals at the heterointerfacial region. With the strain engineering approach evolving from single-phase epitaxial thin films to the recent

vertically aligned nanocomposite films, scientists and engineers are gaining deeper understanding and more efficient manipulation on the relations between strain, microstructure and the enabled properties.

1.3.2 Epitaxial thin films

Initially people input strain into crystalline films by growing single-phase epitaxial thin films on a given crystalline substrate. Epitaxial growth represents that the single-crystal films maintain the same lattice registration as their single-crystal substrates. With similar lattice parameters or crystal structures, the epitaxial thin films usually "mimick" the same growth orientation as the substrates. When the lattice difference between film and substrate is quite large, the unit cells of the epitaxial film would go over a certain rotation to fit with the substrate lattice. For example, CeO_2 unit cell matches with the $SrTiO_3$ (001) substrate after a 45º in-plane rotation. Therefore, good chemical/structural compatibility between film and substrate and proper growth condition control are very critical to fabricate high-quality epitaxial films.

Epitaxial films are classified into homoepitaxial and heteroepitaxial films. Homoepitaxial films mean that the films and substrates are the same materials, such as $SrTiO_3$ film grown on $SrTiO_3$ substrates. The substrate and film are perfectly matched due to their identical crystal structure and lattice parameter (Figure 1.7 (a)). Heteroepitaxial films mean that the films and substrates are different materials, such as $SrRuO_3$ film grown on $SrTiO_3$ substrate. Since the lattice parameters of film and substrate are quite different, the film undergoes lattice distortion and is strained to match the substrate as shown in Figure 1.7 (b). When the lattice parameter difference between film and substrate is too large, the strain on the film is released by generation of dislocation defects (Figure 1.7 (c)).

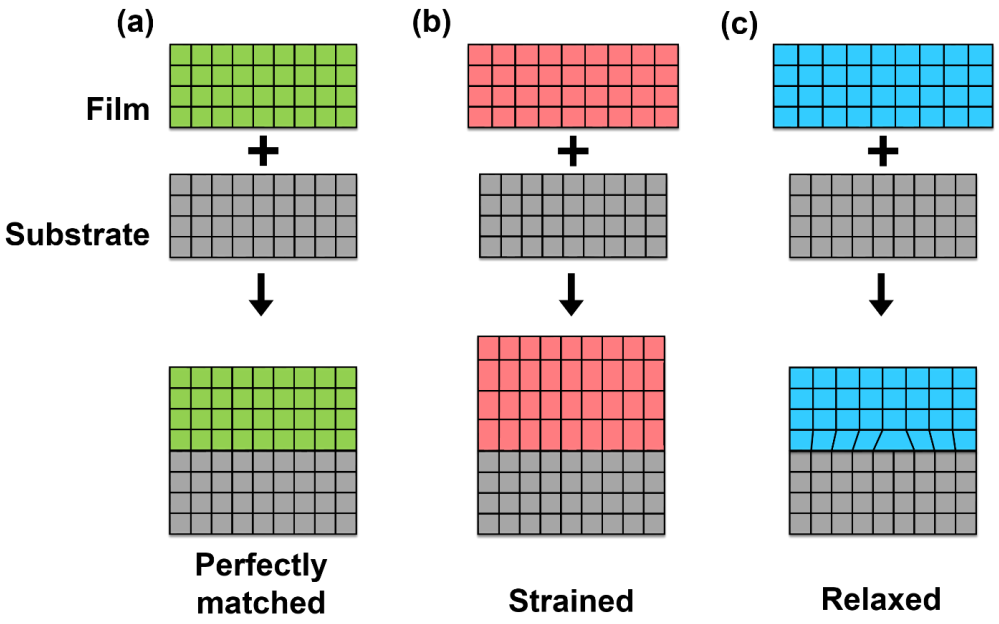

Figure 1.7 Schematic illustration of different epitaxial growth types: (a) perfectly lattice matched, (b) strained, (c) relaxed epitaxial thin film growth.

People have made use of the substrate-clamping effect and input various biaxial strains into perovskite epitaxial thin films by adopting different substrates (e.g. $SrTiO_3$, $LaALO_3$, $DyScO_3$, $LaLuO_3$, etc.) as shown in Figure 1.8 (a). The goal is to modify the crystal structure and further enhance the multifunctionalities of the perovskite thin films for the next generation of electronic, optical, and magnetic devices. It was previously reported that epitaxial strain is able to successfully increase the mobility of semiconductors as well as the transition temperature of ferroelectric and superconducting materials.[26, 48] The transition temperature can be increased enhanced for hundreds of degrees by strain tuning in the epitaxial ferroelectric perovskite oxide thin films compared with the bulk single-crystal counterpart.[53] Although the traditional ideal is that the best ferroelectric performances are usually discovered in the single-crystal forms of that material, the high-quality epitaxial growth of ferroelectric films on appropriate substrates can explore deeper and magnify the potential of the ferroelectric crystals superior the bulk forms. This type of property

improvement was usually realized by changing the chemistry of the materials.[9] Hundreds of degrees' improvement in transition temperature has been observed in the strained ferroelectric $SrTiO_3$, $PbZrO_3$, $BiFeO_3$, and $BaTiO_3$ thin films. Strain in film is usually caused by the lattice parameter difference or different thermal expansion behaviors from the underlying substrate. Large difference in lattice parameters would probably cause generation of defects during film growth and degrade the film performances. Therefore, high-quality substrates are required for the coherently strained thin films.

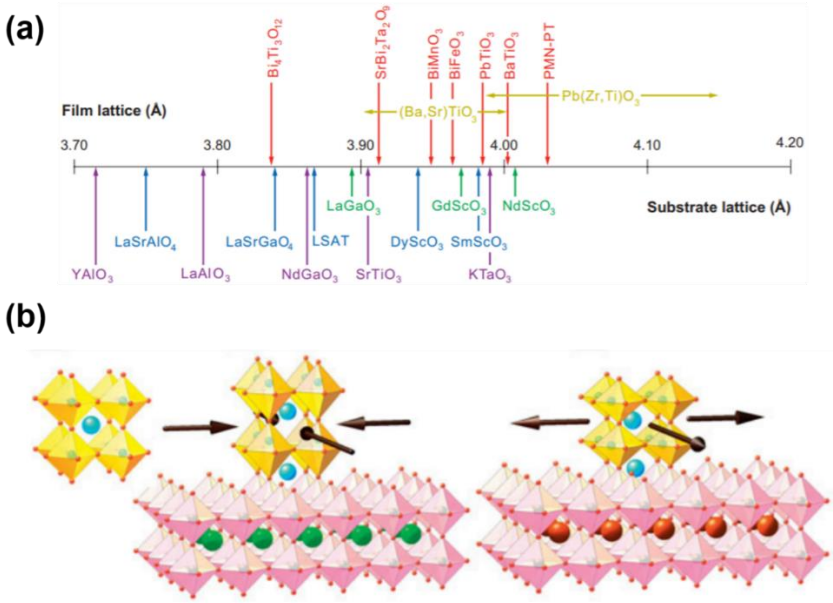

Figure 1.8 (a) Schematic drawing showing the pseudotetragonal or pseudocubic a-axis lattice constant (in angstroms) of some perovskites of current interest and the perovskite-related substrates which are commercially available. (b) Schematic illustration showing the process that unstrained crystal is implemented compressive or tensile strain via the substrate-clamping effect.[40]

In ferromagnetic perovskite oxide thin films, epitaxial strain is able to induce Jahn-Teller effect and to cause rotation and elongation of the oxygen octahedral units (BO_6). The size, shape and connectivity between the octahedrons directly influence the electronic structure of the ferromagnetic perovskite oxide films and accordingly tailor their physical performances when

applied in devices. The relation between physical properties and strain has been reported in epitaxial LSMO films on different substrates. For instance, the strain effect on the magnetic anisotropy has been explored in the epitaxial LSMO films deposited on $SrTiO_3$ (001) and $LaGaO_3$(001) substrates. The strain influence on the magnetic and magnetotransport properties are investigated in LSMO thin films by selecting different substrates and tetragonal distortions. Wu *et al.* demonstrated the improvement of magnetotransport properties in compressively strained LSMO films. Yang *et al.* compared the $La_{0.67}Sr_{0.33}MnO_3$ films grown on different substrates including $SrTiO_3$, $LaAlO_3$, $DyScO_3$, $GdScO_3$, and $(LAO)_{0.3}(SATO)_{0.7}$ (LAST) substrates especially their magnetic performances. Increasing the tensile tetragonal distortion in the LSMO thin films is able to successfully reduce the saturation magnetization, increase the electrical resistivity by several orders of magnitude, and efficiently tune the resistivity-temperature curves as well as the magnetoresistance performances. More recently, Adamo *et al.* conducted a detailed study on the biaxial strain effect on the physical properties of epitaxial LSMO (001) thin films. Their results show that the Tc and electrical transport data of the ~22 nm LSMO films strongly depends on substrate-induced biaxial strain.

1.3.3 Limitations of substrate-induced strain engineering

Strain engineering has been well-acknowledged as a powerful way to tune and manipulate the physical properties and even empower the known materials with new functionalities. Strain engineering by substrate-clamping effect has been well investigated in the past two decades. Numerous successful examples have been observed with tunable functionalities. However, the drawbacks of this conventional approach are noticed to have hindered the further development of the strain and property tuning as well as in real applications.

As discussed above, when the lattice difference is too large or the film thickness is above the critical thickness, dislocation defects are generated driven by the minimization of the overall system energy and degrade the film performances in reality. The critical thickness is only a few or tens of nanometers. In devices, the perovskite oxide films are usually above 50 nm or even ~100 nm, which evidently relaxes the strain imparted in the films and diminish the strain effect. Therefore, substrate-clamping strain is only used in thin films and hard to be encouraged in the thicker films for practical devices. Moreover, the film-substrate interfacial area is limited as well as the tuning efficiency.

1.4 Self-assembled Nanocomposite Thin Films

To pursue further improvement, more researchers have started to assemble nanocomposite thin films and highly enhanced interfacial area within the films by introducing secondary phase into the film matrix. There are three types of architectured nanocomposite films: (1) nanoparticles of a secondary phase embedded in the film matrix (so-called 0-3 type), (2) multilayer stacked thin films (so-called 2-2 type), and (3) vertically aligned nanocomposite thin films (1-3 type). The nanocomposite configurations combine the advantages from each phase and even exhibit novel phenomenon derived from the new microstructure, interfacial coupling and their interplay.

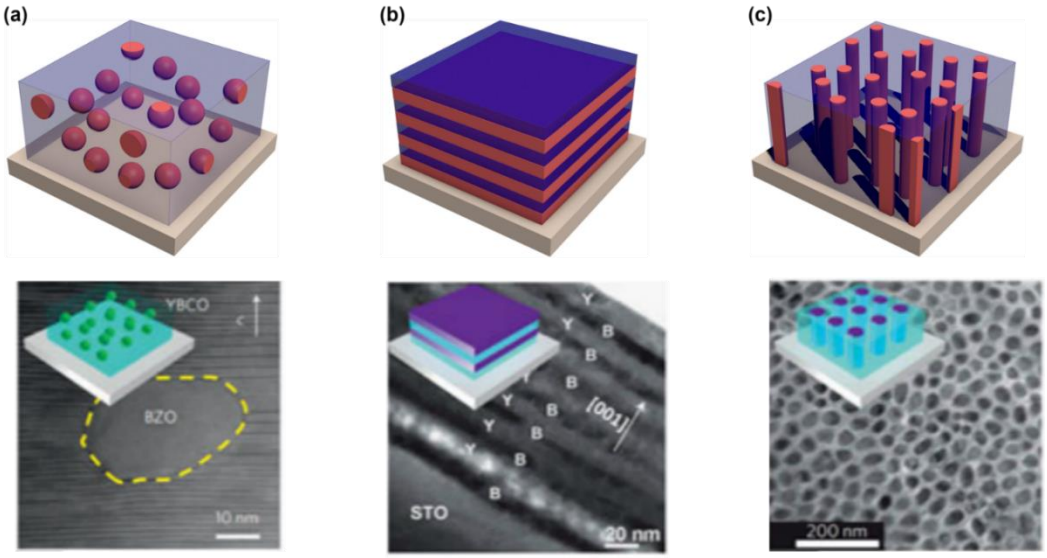

Figure 1.9 (a) A typical 0-3 type nanocomposite with an example of $BaZrO_3$ nanoparticles in $YBa_2Cu_3O_7$ matrix. (b) A typical 2-2 type (multilayer) nanocomposite films with alternating layers of $YBa_2Cu_3O_7$ (Y) and $BaZrO_3$ (B) in the example below. (c) A 1-3 type of nanocomposite and its example of Sm_2O_3 nanopillars distributed in $BaTiO_3$ matrix.[54]

1.4.1 Nanocomposite thin films (0-3)

To promote the strain engineering application in thick films as well as multifunctional devices, many materials scientists and engineers started to assemble nanocomposite thin films, starting from embedding nanoparticles of a secondary phase into the primary matrix and forming the 0-3 type configuration. In this way, more interfaces are introduced within the films and could potentially overcome the critical thickness barrier in the epitaxial single-phase films. The advantages and properties can be simultaneously combined within the same film based on reasonable materials selection. By changing the size, morphology and distribution of the nanoparticles in matrix, the microstructure, interfacial coupling, and strain states can be controllable to researchers.

The design of 0-3 was realized in $La_{0.67}Ca_{0.33}MnO_3$ (LCMO)-MgO system with the manganite nanoparticles discretely embedded in the three-dimensional insulator matrix based on

the core-shell LCMO-MgO composite powders. The size of the spherical LSMO is controlled uniform and uniformly distributed in the MgO matrix. Changing the relative ratio between LCMO and MgO displaces LSMO under a tensile strain. The metal-insulator transition temperature is reduced and the magnetotransport perforamcnes are advanced with the enhancing MgO amount. The 0-3 configuration is demonstrated to be a promising way by this work.[55] Artificial pinning centers of $BaZrO_3$ nanoparticles strained the $YBa_2Cu_3O_7$ matrix and caused an outstanding vortex-pinning enhancement for the superconductor applications.[56]

Although the 0-3 type configuration has improved the properties of film matrix by embedding nanostrained particles, the drawback of this configuration still cannot be overcome. In this configuration the interfaces is confined with limited area. Too many nanoparticles of secondary phase in the matrix will suppress the overall mechanical performances of the films.

1.4.2 Multilayer nanocomposite thin films (2-2)

Based on the conventional epitaxial thin film, the 2-2 type nanocomposite films is constructed by depositing thin epitaxial layers of two phases alternately, stacking them on top of each other, and forming the layer-by-layer configuration. Compared with the conventional epitaxial film, the lateral interfacial area is highly enlarged and dislocation density is constrained since each layer is very thin. The interplay between layers is mutual and the strain tuning effect is heavily intensified.

The multilayer nanocomposite contains bilayer, trilayer, and more layered configurations, which are designed according to the property demands. For instance, one ferromagnetic layer Mn_3O_4 was epitaxially grown on top of a ferromagnetic layer $La_{0.7}Sr_{0.3}MnO_3$ (LSMO) layer forming a bilayer microstructure grown on $SrTiO_3$ (001) substrate. Instead of tensile strain in LSMO epitaxial films, the addition of Mn_3O_4 layer flips the strain state of LSMO layers to

compressive and can continuously intensify the compressive strain through Mn_3O_4 layer thickness, inducing tetragonal distortion of LSMO and enhance the saturation magnetization below 50 K. This combination of ferromagnetic and ferromagnetic layers demonstrates the benefits of the multilayer stacking configuration.[57] A $BaTiO_3/SrRuO_3/SrTiO_3$ trilayer structure was constructed in a heteroepitaxial film deposited on STO (001) substrate via pulsed laser deposition for the exploration of the oxygen pressure dependence on the microstructure and ferroelectric properties.[58] This trilayer configuration has been used to study the tunneling magnetoresistance by sandwiching a thin layer of MgO as tunneling barrier with two layer of Fe.

Although multiple heteroepitaxial layers are vertically stacking on top of each other, their applications are still constrained by the substrate-film clamping effect. When a multilayer film grows thick enough, the strain on it is slowly relaxed similar to epitaxial single-phase films.

1.5 Vertically Aligned Nanocomposite (VAN) Thin Films

1.5.1 Overview of VAN

Aiming for higher tunability on the functionalities of complex oxide films, a new microstructure—vertically aligned nanocomposite (VAN) has been systematically investigated and attracted dramatic attention due to its more efficient strain engineering in thick films. In general, these nanocomposite films have two immiscible phases vertically aligned next to each other, forming the columnar microstructure and numerous vertical heterointerfaces. The vertical strains are the collective results of the lattice constant mismatch along the heterointerfaces, elastic constant mismatch, thermal expansion, synthesis conditions and many other factors. VAN have been intensively studied to obtain a deeper understanding of the microstructure, interfacial coupling, strains, and defects. The VAN architecture have been used to strengthen the following

functionalities such as superconductivity, ferroelectricity, ferromagnetism, antiferromagneticsm, multiferroicity, and ion conduction. This design benefits multifunctional devices in electric, magnetic, optical and energy storage fields.

The first VAN microstructure was demonstrated in $La_{0.7}Ca_{0.3}MnO_3$ (LCMO)-MgO system by a solution based synthesis, demonstrating a phase transition as well as the tunable magnetotransport performances in the LCMO-based nanocomposite films.[59, 60] Later more VAN thin films were prepared through PLD in other systems, such as BTO-CoFe2O4, LSMO-ZnO, BFO-Sm2O3, and more. Most of the VAN thin films are achieved in perovskite-based systems. Recently some new combinations starts to draw more research interest for plasmonic and optical applications, such as oxide-nitride, oxide-metal, and nitride-metal.

The VAN systems have exhibited tremendous potentials in manipulating strain vertically in thick films. The vertical strain engineering is a new modulation tool different from the previous lateral interfacial coupling in epitaxial and multilayer films. In VAN thin films, vertical interfacial area is way much larger than the lateral film-substrate interfacial area. Therefore, the vertical strain engineering dominates the overall performances of the film. The substrate-clamping effect is diminished with the increasing film thickness. In contrast, the vertical strain effect in VAN configuration is not influenced or suppressed by the increased film thickness. Due to its microstructure feature, the vertical strain engineering is strengthened periodically and the tunability on properties become more efficient and flexible. Meanwhile, it is also noted that an ideal self-assembled VAN composite films even with spontaneous ordered microstructure can be achieved after a reasonable materials selection and careful deposition exploration.

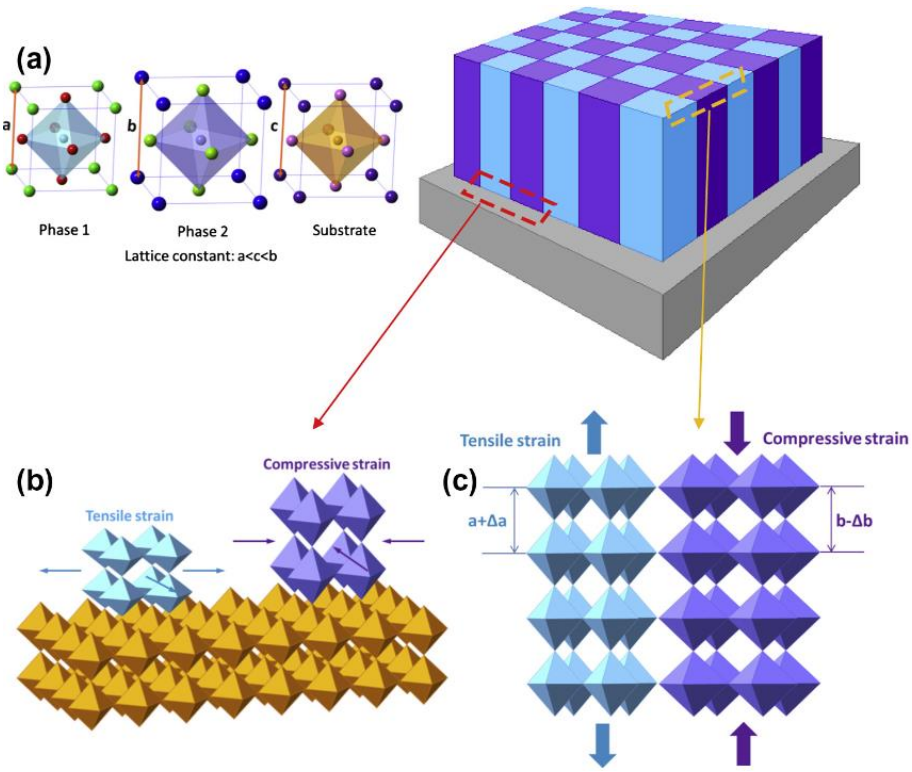

Figure 1.10 Schematic illustration of lattice mismatch in the VAN microstructures: (a) unstrained unit cells of the film phases and substrate, (b) biaxial strain effect on the film derived from the substrate-clamping effect, and (c) vertical strain coupling between the two phases within the VAN film, resulting in phase 1 and 2 under the opposite strain states.[61]

Therefore, the emerging VAN systems provide a solution for effective strain engineering in thicker films since the vertical strain is insensitive to the film thickness up to hundreds of nanometers or even micrometers. This enables the VAN designs more suitable for electronic devices in reality. The conventional substrate clamping effect cannot constrain the VAN designs' applications since the total lateral contact area between the nanocolumns with substrate is much less than the vertical interfacial area within the nanocomposite films. This highly enhanced vertical interfacial area provides a better platform for fundamental studies on interfacial-, strain-, microstructure-enabled tunability and more oriented applications. The epitaxial strain derived from

lattice mismatch along vertical interfaces can rise above 10% recently when two phases of highly dissimilar structures are combined together into VAN epitaxial thin films.[62]

1.5.2 VAN growth mechanisms

It has been reported that the VAN thin films have three major crystal growth mechanisms: (1) nucleation and growth, (2) spinodal decomposition and (3) pseudo-spinodal decomposition mechanisms.[63] Here the latter two are combined together for discussion since they are similar and both leads to checkerboard microstructure with spontaneously ordering.

The nucleation and growth mechanism is most commonly used to explain the VAN thin film growth when the two film phases immiscible. It involves the following three major steps: (1) adatom diffusion on substrate surface, (2) nucleation and island growth, and (3) columnar growth of islands into pillars or rods (Figure 1.11). In the initial nucleation stage, atoms or clusters of difference species arrive at the substrate surface and diffuse laterally. After the defects or pits on the substrate surface trap the atoms or clusters forming numerous, more atoms or clusters prefer attaching onto them, agglomerating, and forming individual islands to reduce the interfacial energy. It was claimed that the adatoms energetically favor to attach on the islands of their identical composition in the previous reports.[64, 65] These small islands are randomly located and distributed on the substrate surface. With increasing deposition time, more adatoms accumulate together and accelerate the islands' further growth into pillars in the columnar growth period. After the deposition process, VAN thin films are formed with various microstructures such as checkerboard, nanopillars-in-matrix, nanomaze and more. The geometric feature and dimensions such as the diameter and shape of nanopillars strongly depend on the growth kinetic conditions, such as deposition temperature, laser energy, frequency, etc. These will be discussed in the later session in detail. Those microstructural features are closely associated with the strain state of each

phase and ultimate performances of thin films. The nucleation and growth mechanism can be used to describe the growth of most VAN thin films. Basically the two immiscible phases grow simultaneously and separately and generating the vertical interfaces. The final microstructure and physical properties are determined by the intrinsic feature of the two phases and also the growth conditions, which will be discussed in detail in latter session.

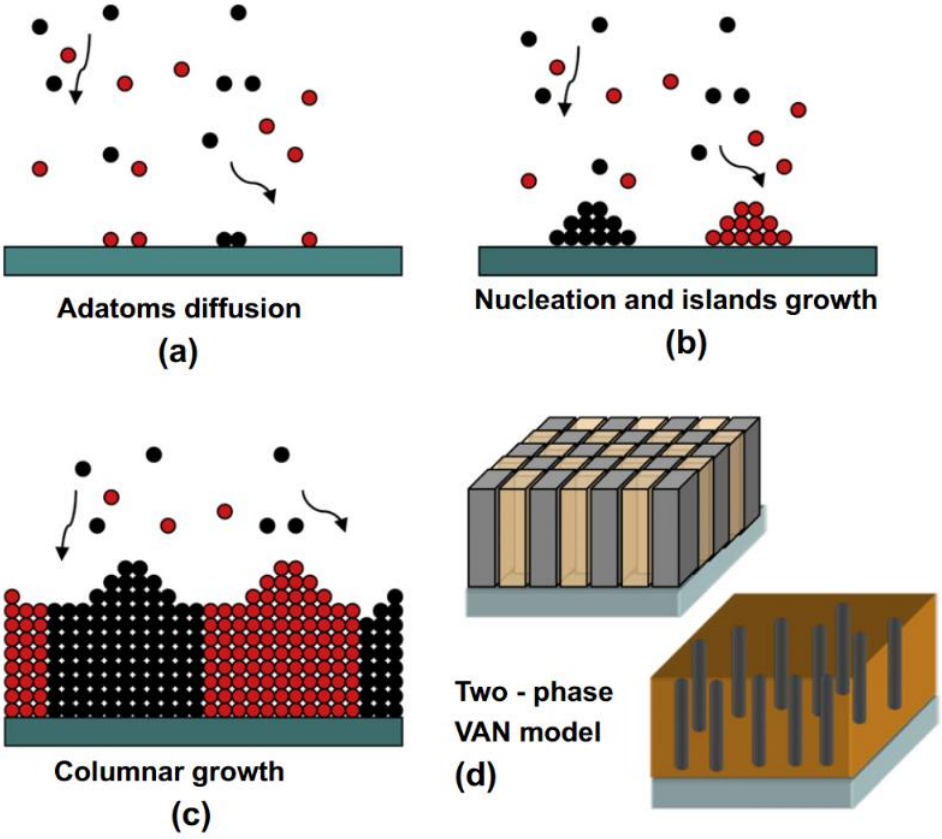

Figure 1.11 Schematic illustration showing the nucleation and growth mode of a VAN thin film: (a) adatoms diffusion, (b) nucleation and island growth, (c) columnar growth and (d) forming the VAN films with the microstructure of checkerboard or nanopillars-in-matrix.[64]

Both spinodal and pseudospinodal decomposition lead to the well-ordered checkerboard structure of smaller spatial features. Pseudospinodal decomposition is a combination between spinodal decomposition and nucleation-growth mechanisms.[63] The well-known spinodal decomposition growth mechanism occurs a solid solution system formed at high temperature tends

to naturally separate during cooling down process. The whole transition from miscible to immiscible is driven by minimization of the overall system energy and results in checkerboard microstructure with high level of spontaneous ordering. Thus, the geometric feature of the spontaneously ordered microstructure is naturally created and around several to tens of nanometers, which is way much smaller than the artificially templated ordering of nanocomposite thin films. This phenomena is usually observed in the solid solution containing multiple species of metal cations whose crystal structure is unable to still accommodate those cations at low temperature.[66] The materials with Jahn-Teller distortion also prefer spinodal decomposition and congregate into ordered domains with different stoichiometries. For example, $ZnMnGaO_4$ thin film is easily decomposed into a checkerboard structure with alternating domains of orthorhombic structure and tetragonal structures, corresponding to Mn-rich and Mn-poor regions (Figure 1.12 (a-c)).[67] The checkerboard BFO-Sm_2O_3 VAN film in Figure 1.12 (d) is driven by reduction of the strain energy of the system.[68]

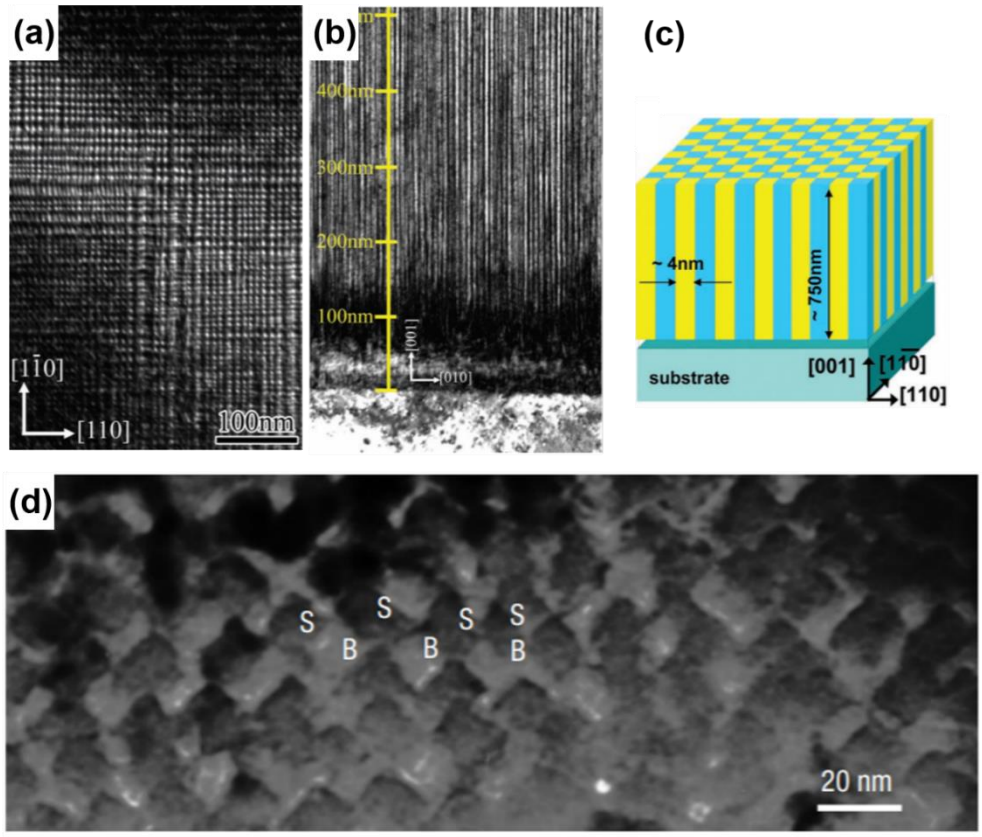

Figure 1.12 (a) Plan-view and (b) cross-sectional TEM images of $ZnMnGaO_4$ thin film on MgO (001) substrate, with a (c) schematic illustration of the checkerboard microstructure.[67] (d) Plan-view TEM image of $BiFeO_3$-Sm_2O_3 VAN thin film showing a checkerboard microstructure.[68]

1.5.3 Microstructure control of VAN

The different crystal structures and growth conditions lead to a rich spectrum of VAN microstructures, such as nano-checkerboard, nanopillars or nanorods in matrix, nanomaze structures, etc. Worth to note that two major VAN systems have been attracting extraordinary attention and involved in the microstructure control studies: (1) LSMO-based VAN system coupled with a secondary phase M which is usually selected from insulators and semiconductors and (2) perovskite-spinel VAN system, such as BFO-CFO. Not only because these systems have tunable outstanding ferromagnetic and ferroelectric properties for the novel electronics, but also

they provide more possibilities and a larger playground for the interesting explorations on microstructure control and strain engineering. There are many approaches that have been systematically studied to tune the VAN microstructures, such as substrate selection, substrate orientation, buffer-layer, selection of the secondary phase, relative ratio between the film phases, and growth kinetics (e.g., deposition temperature, oxygen pressure, and laser frequency).

Selection of substrates with different lattice parameters have been heavily used to input tunable strains into the single-phase epitaxial films, induce corresponding electrical/crystal structure distortions, and further manipulate the functional performances of the single-phase epitaxial films. Evident difference between the substrate and film can even cause phase transition or different crystal growth orientation. When it is applied in the VAN epitaxial thin films, substrate selection demonstrates more dramatic effect not only on the crystal structure, growth orientation and strain of each phase, but also on the interplay and coupling between the two film phases. Thus, substrate selection has a more efficient tuning on the VAN epitaxial films and even a minor lattice parameter difference may cause evident modulations on the crystal structure, growth orientation, or surprising phenomena. Take $BiFeO_3$ (BFO)-$CoFe_2O_4$ (CFO) VAN films as an example. As shown in Figure 1.13, BFO-CFO VAN films are epitaxially grown on the following substrates—$LaAlO_3$ (LAO), $LaNiO_3$-buffered LAO, $SrTiO_3$ (STO), $MgAl_2O_4$ (MAO), and MgO substrates. The corresponding in-plane lattice matching distance of the aforementioned substrates is 3.79 Å, 3.86 Å, 3.91 Å, 4.02 Å, and 4.21 Å, respectively, The distinct strain effects from those substrates induce a phase transition of BFO from tetragonal structure (T-BFO grown on LAO substrate) to rhombohedral structure (R-BFO grown on LNO and STO substrates). However, when the matching distance of substrate keeps rising up to 4.02 Å and 4.21 Å, the BFO phase decomposes on MAO and MgO substrates.[62] Figure 1.14 gives another example of different substrates

affecting the strain and growth orientation of film phase. Different substrates $NdGaO_3$ (NGO), STO and $DyScO_3$ (DSO) are used for the growth orientation of CFO phase in the BFO-CFO VAN thin films, corresponding to the in-plane matching distance of 3.85 Å, 3.90 Å and 3.94 Å, respectively. Driven by the strain difference on the films, CFO nanopillars are grown on along (111), (001) and (110), while the BFO matrix is consistently maintained along (001). Therefore, the resultant CFO nanopillars are in different morphologies—triangular platform, pyramid, and roof, respectively. It enables the tunability of the magnetic anisotropies in the aforementioned VAN films accordingly.[69]

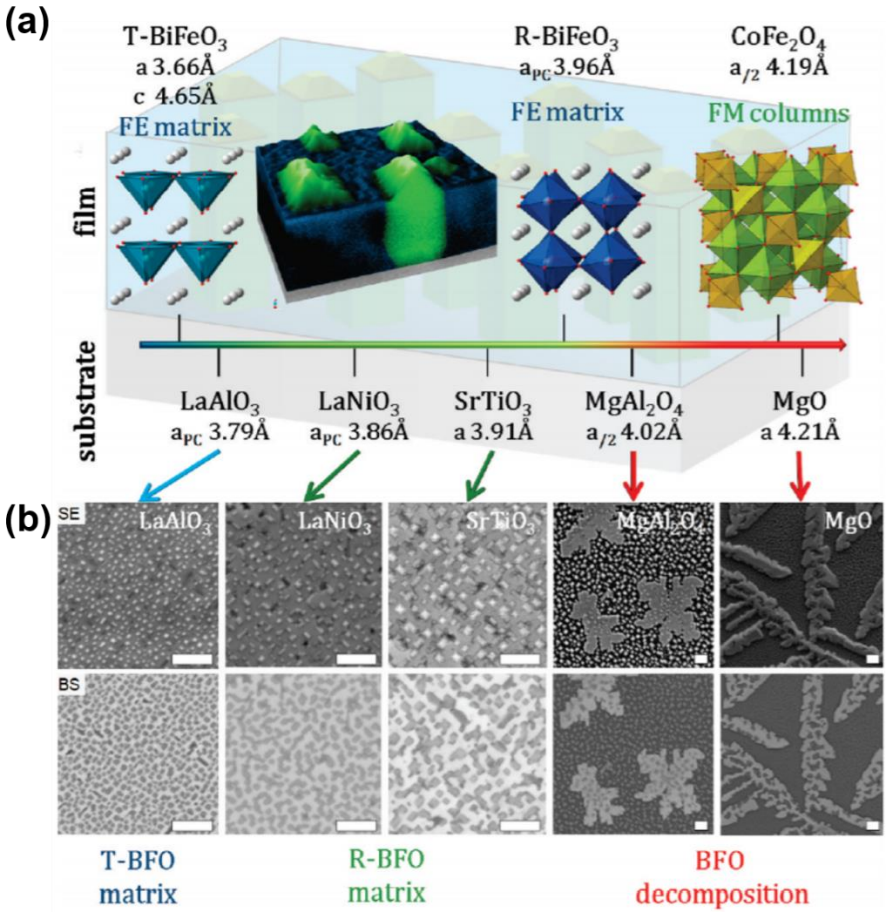

Figure 1.13 (a) Schematic illustrations of tetragonal $BiFeO_3$, rhombohedral $BiFeO_3$, and $CoFe_2O_4$ crystal structures, as well as the matching distance variation in $LaAlO_3$, $LaNiO_3$, $SrTiO_3$, $MgAl_2O4$, and MgO substrates. (b) Scanning secondary electron (SE) and backscattered electron (BS) images of the $BiFeO_3$-$CoFe_2O_4$ films grown on the aforementioned substrates with the matching distance increasing from 3.79 Å to 4.21 Å.[62]

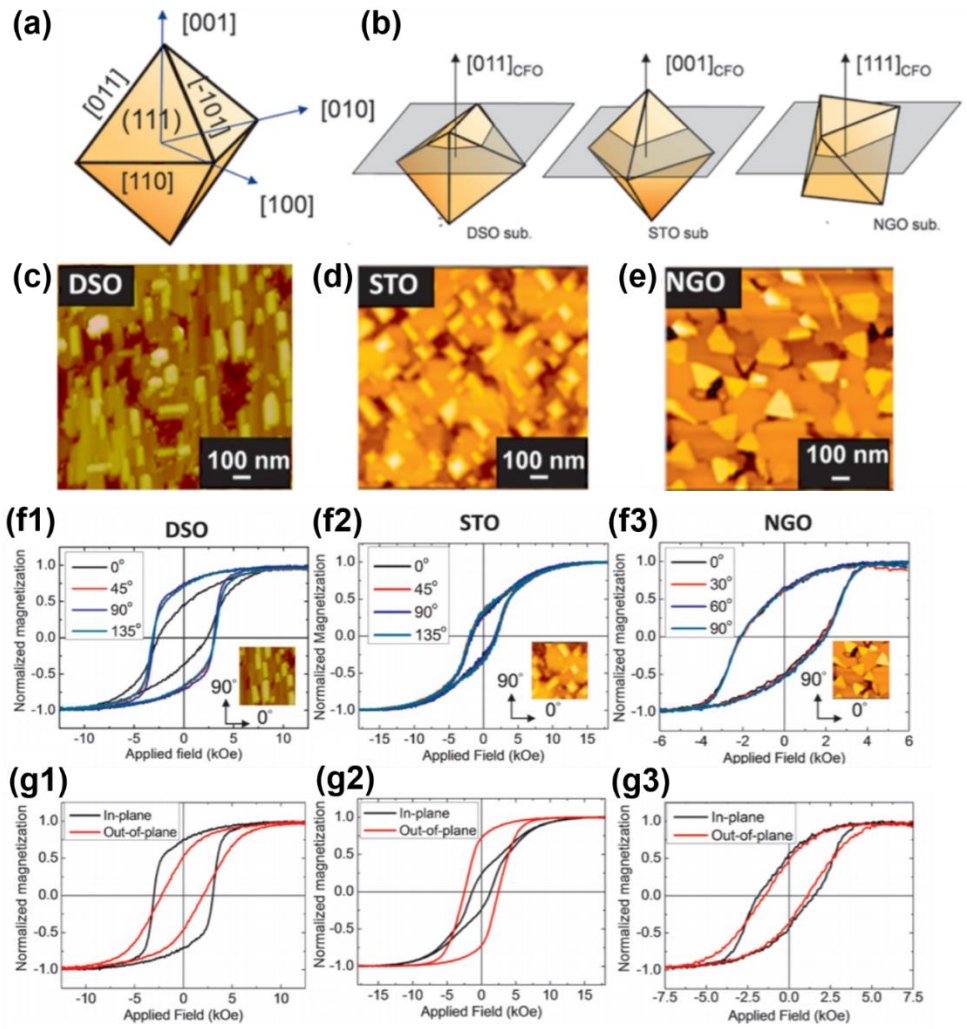

Figure 1.14 Schematic illustration of (a) the lowest energy surfaces of CFO crystal, and (b) crystal orientation of CFO grown on top of the different substrates. (c-e) AFM images of BFO-CFO films grown on the DSO, STO, NGO substrates. Magnetic hysteresis loops of BFO-CFO VAN thin films grown on different substrates: (f1-f3) along different in-plane directions and (g1-g3) along in-plane and out-of-plane directions. [69]

When the substrate chemistry is settled, substrate orientation is able to successfully manipulate the growth orientation, microstructures and physical responses of the VAN thin films because of the anisotropic surface energy, stress and diffusivity.[70-73] Zheng *et al.* still used BFO-CFO system as the prototype and studied the influence of substrate orientation on the VAN structures.[70] Due to the different crystal structure, surface/interface energy, and wetting ability,

CFO and BFO display different growth behaviors on differently oriented substrates. As shown in Figure 1.15, the BFO-CFO VAN films exhibit quite different microstructures grown on STO (001), (111), and (110) substrates, respectively. CFO favors to wet the STO (111) surface and BFO prefers the STO (001) surface. When grown on STO (001) substrate, BFO can easily wet the substrate surface and exhibits a layer-by-layer growth mode. CFO only can partially wet the substrate surface and reveals the island growth mode. Therefore, the BFO-CFO VAN shows the CFO nanopillars embedded in BFO matrix (Figure 1.15 (a)). On STO (111) substrate, CFO can fully wet the substrate surface and grows in the layer-by-layer fashion, while BFO grows into nanopillars embedded in the CFO matrix (Figure 1.15 (e)). Both BFO and CFO display island growth on the STO (110) substrate, forming a nanomaze VAN microstructure in Figure 1.15 (i), since the STO (110) is not along either of the lowest-energy surface.

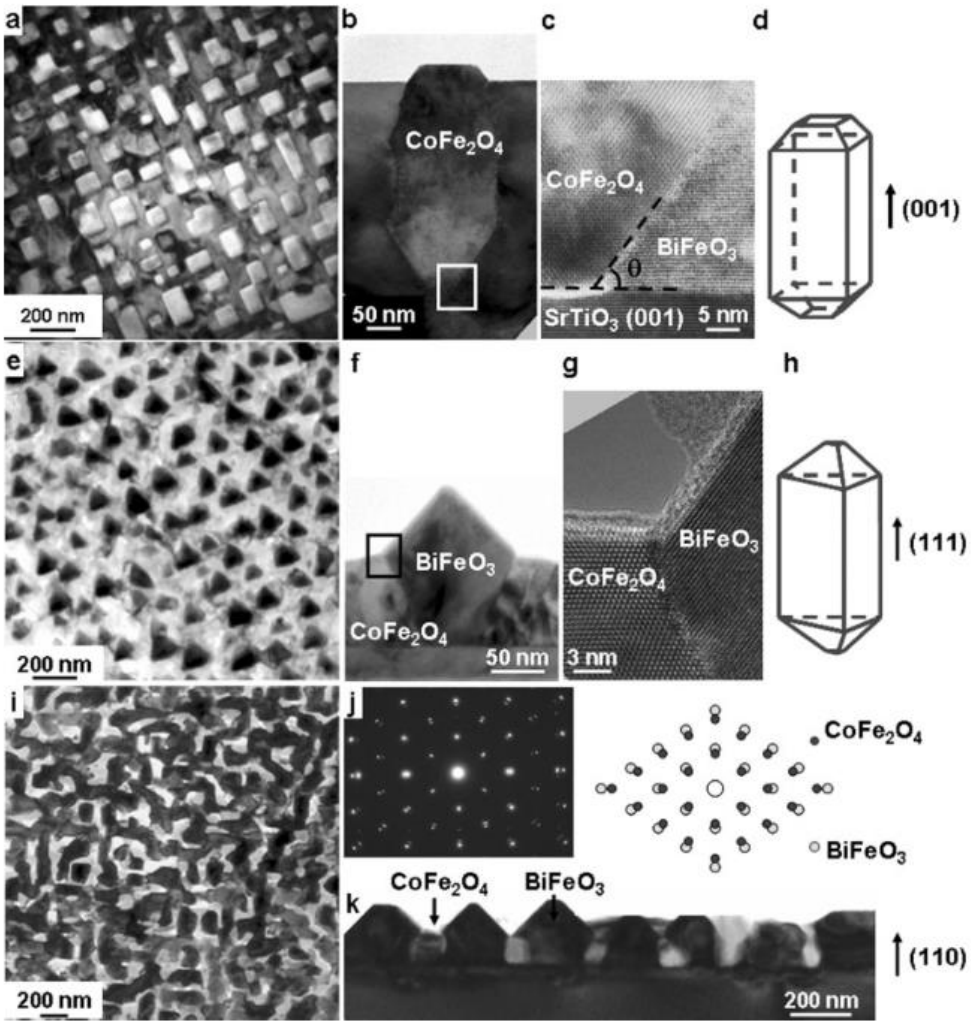

Figure 1.15 (a) Plan-view and (b) cross-sectional TEM images of the BFO-CFO VAN thin film grown on STO (001) substrate. (c) HRTEM image of the interfacial area corresponding to the area marked by a white rectangle in (b). (d) Schematic drawing of a CFO nanopillar. (e) Plan-view and (f) cross-sectional TEM images of the BFO-CFO VAN thin film grown on STO (111) substrate. (g) HRTEM image of the interfacial area corresponding to the area marked by a black rectangle in (f). (h) Schematic drawing of a $BiFeO_3$ nanopillar. (i) Plan-view TEM image, (j) SAED pattern, and (k) cross-sectional TEM image of the BFO-CFO VAN thin film on STO (110) substrate.[70]

Moreover, buffer-layer can be considered as a decoration on the substrate to achieve more precise control on the lattice parameter as well as desired chemistry compatibility. For example, different growth and morphologies of BFO-CFO thin films are observed once a buffer-layer of

LNO is added between the film and LAO substrate (Figure 1.16 (a-d)).[62] The geometric feature of NiO domains in NiO-$Sr_3A_2lO_6$ (SAO) tends to be ordered and aligned with the addition of NiO buffer-layer onto STO substrate (Figure 1.6 (e) and (f)).[74] The buffer-layer idea has also been well applied in silicon integration to obtain a good epitaxial growth of multiple oxide films and satisfactory performances which is unable to be accomplished previously in semiconductor industry.[75, 76] As the transition between the film and original substrate, buffer-layer enables more flexibility and benefits in fundamental study and industry.

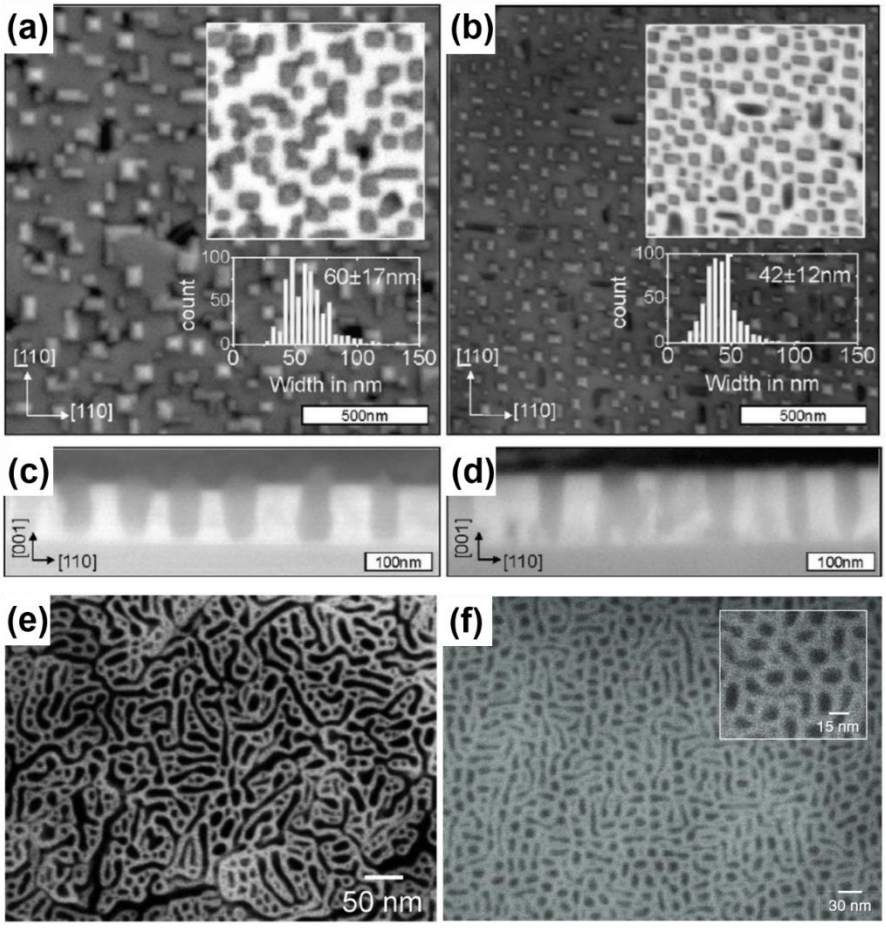

Figure 1.16 Top-view SEM images of the BFO-CFO films grown on (a) LNO-buffered LAO substrate and (b) LAO substrate. Cross-sectional backscattered electron images of the BFO-CFO films grown on (c) LNO-buffered LAO substrate and (e) LAO substrate.[62] Top-view SEM images of NiO-$Sr_3Al_2O_6$ (SAO) VAN thin films grown on (e) STO and (f) NiO-buffered STO substrates.[74]

The nanomaze microstructure of BFO-CFO VAN thin films can be further modified by changing the relative volume/molar ratio between the two phases. As shown in Figure 1.17 (a-c), with the volume ratio of BFO:CFO varying from 65:35 to 33:67, the feature of the nanomaze microstructure becomes smaller and the domains tend to be aligned, even though the growth mode of each phase doesn't change obviously. Actually, varying the relative ratio is a quite popular way to tailor the VAN microstructures.[64, 70, 73, 75, 77, 78] A precise and systematic microstructural tuning was observed in $YBa_2Cu_3O_7$ (YBCO)-$BaZrO_3$ (BZO) VAN systems—the BZO nanorods embedded in YBCO matrix is gradually transferred to horizontal nanoplates with the composition x of BZO increasing from 0.05 to 0.5 (Figure 1.17 (d-g)).[78]

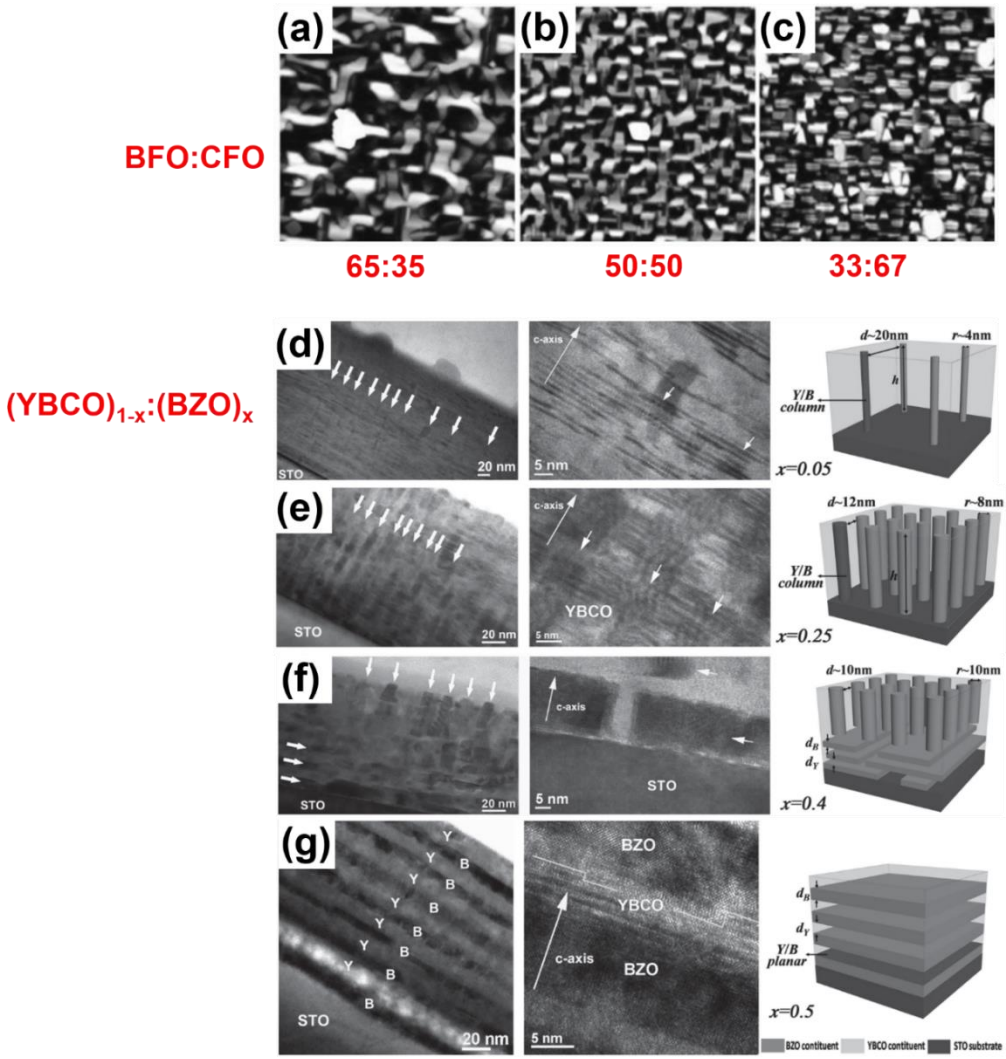

Figure 1.17 AFM images of BFO-CFM VAN thin films with different volume ratios of (a) 65:35, (b) 50:50, and (c) 33:67.[70] Cross-sectional TEM images and schematic illustrations of YBCO-BZO VAN thin films with the different compositions of x = (d) 0.05, (e) 0.25, (f) 0.4 and (g) 0.5.[78]

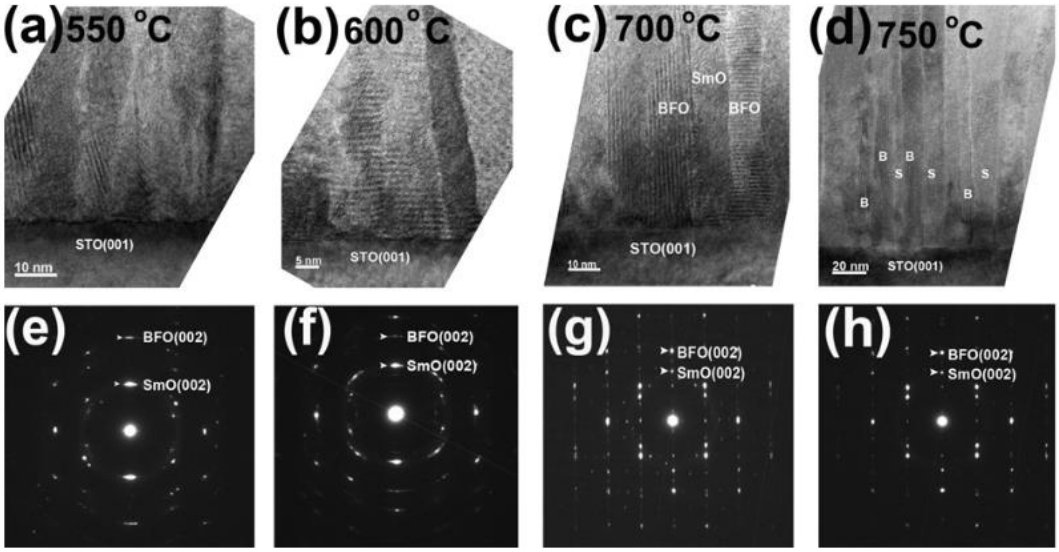

Figure 1.18 Cross-section TEM images of the BFO-Sm_2O_3 VAN thin films prepared at (a) 550 ºC, (b) 600 ºC, (c) 700 ºC and (d) 750 ºC, as well as their corresponding SAED patterns in (e-h).[64]

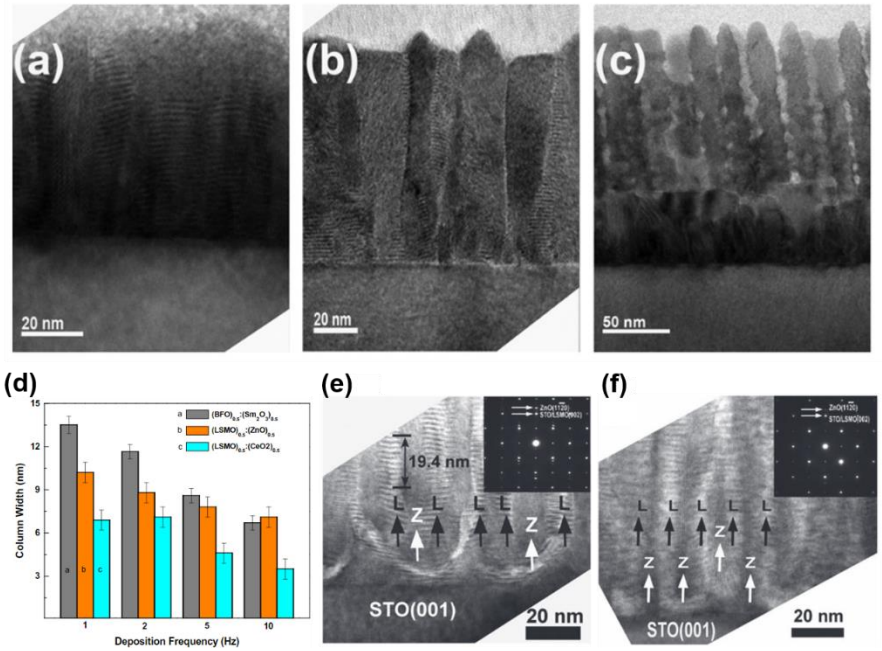

Figure 1.19 Cross-sectional TEM images of $BiMnO_3$-Sm_2O_3 VAN thin films prepared under the various O_2 pressures of (a) 50 mTorr, (b) 100 mTorr and (c) 200 mTorr. (d) Average column/domain width variation of the two phases in BFO-Sm_2O_3, LSMO-ZnO, and LSMO-CeO_2 nanocomposite thin films.[64] Cross-sectional TEM images of LSMO-ZnO VAN thin films deposited by laser frequencies of (e) 1 Hz and (f) 10 Hz.[31]

VAN microstructures are also closely dependent on the growth kinetics, including deposition temperature, oxygen pressure, laser frequency and more. Figure 1.18 shows the influence of different deposition temperature on the microstructure and crystallinity of BFO-Sm_2O_3 VAN films.[64] Although all these VAN films exhibit vertical columnar features with the deposition temperature increasing from 550 °C to 750 °C, high deposition temperature enables high quality of epitaxial growth (Figure 1.18 (e-h)), easy phase separation and better domain alignment with smaller pillar width (Figure 1.18 (a-d)). As the high deposition temperature provides sufficient energy for the adatoms' diffusion and relocation in crystal growth. However, the temperature cannot be too high, which could be detrimental to the VAN film growth and cause intermixing between phases. Oxygen pressure is also a critical key to tuning VAN microstructure. Figure 1.19 (a-c) reveal the microstructural evolution of BMO-Sm_2O_3 composite films prepared under the oxygen pressure increasing from 50 mTorr to 200 mTorr. At the oxygen pressure of 100 mTorr, the film achieves a very nice BMO-Sm_2O_3 VAN architecture with a clear phase separation and vertical interfaces. When the oxygen pressure reaches 200 mTorr, the film phases prefer island growth and exhibit roughened vertical interfaces. This could be explained by the unbalanced stoichiometry during the film growth. Moreover, the vertical domain size and spacing can be easily adjusted by changing the deposition frequency (Figure 1.19 (d-f)). Increasing deposition frequency can efficiently reduce the nanopillars' width and increase their aspect ratio as the higher deposition frequency allows shorter surface diffusion path and resting time of adatoms during the film growth and results in smaller nucleation islands and thinner pillars. Therefore, a decent VAN microstructure can be achieved through reasonable selection of film phases and substrates as well as careful deposition control.

Perovskite manganite LSMO has been well studied for decades due to its fascinating physical properties such as magnetic anisotropy, colossal magnetoresistance and spin-glass like behaviors. It has been used not only for the fundamental physics study but also for its potential application research. But the colossal magnetoresistance is usually constrained by the requirement of high magnetic fields. Recently the low field magnetoresistance phenomena is attracting more attention which is induced by the spin-polarized tunneling effect at the grain boundaries. It has provoked increasing interest due to the large magnetoresistance performances at low magnetic field. Not only grain boundaries, the nanodomains of insulators and semiconductors also serve as the energy barriers for the magnetotunneling effect. Therefore, increasing researchers are devoting to the LSMO-based thin films with the VAN microstructures. As shown in Figure 1.19, a variety of insulators and semiconductors have been attempted as the secondary phase in VAN structures, including MgO, ZnO, CeO_2, BFO, and NiO. The different crystal structure, lattice parameters, coupling relation and modulus give birth to different microstructures, such as circular nanopillars in matrix or rectangular nanopillars in matrix. However, from the cross-section view they are all vertically aligned nanopillars which are uniformly distributed in the matrix with clear phase separation.

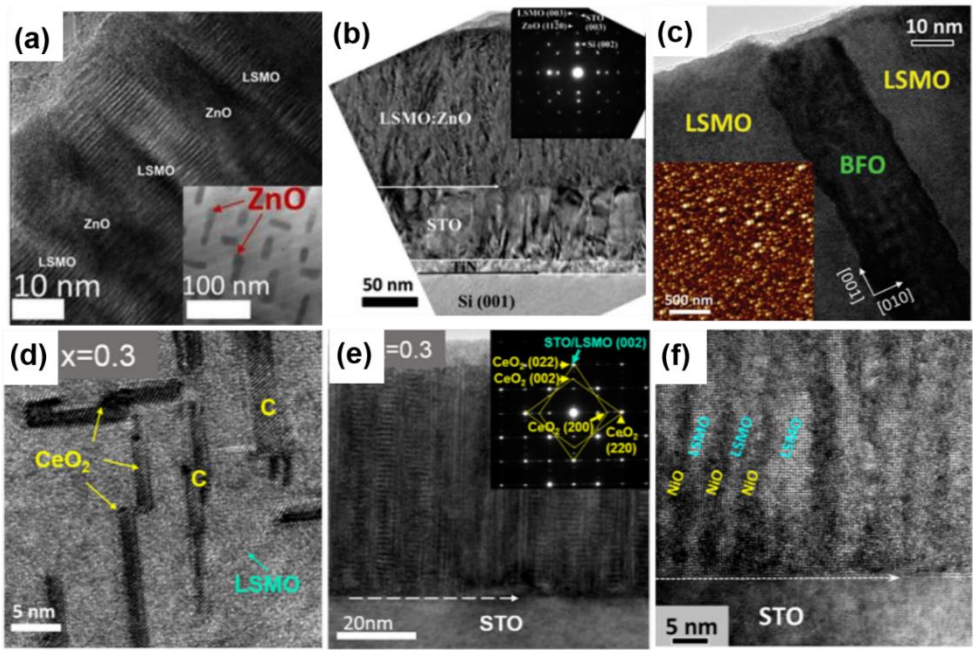

Figure 1.20 Cross-section TEM images of (a) LSMO-ZnO VAN thin film on LAO (001) substrate and (b) LSMO-ZnO VAN thin film integrated on Si (001) substrate.[75, 79] (c) Cross-section TEM image of LSMO-BFO VAN thin film with its top view AFM image as the inset.[80] (d) Cross-section and (e) plan-view TEM images of LSMO-CeO_2 VAN thin film grown on STO (001) substrate.[77] (f) Cross-section HRTEM image of LSMO-NiO VAN thin film.[81]

1.6 Future Prospects

Increasing efforts are devoted on studying the VAN systems, which have exhibited a broad spectrum of tunable and highly enhanced fascinating functionalites contributed by their unique microstructures and vertical strain engineering. The tuning approaches have been systematically studied in many material combinations. The VAN configuration has provide more opportunities and pathways to conduct fundamental studies and explore novel properties which the conventional form doesn't have.

Meanwhile, this VAN configuration still has a long way to be well understood and more precisely controlled. There are still some challenges and uncertain problems such as the microstructure control and the relation between the vertical strain engineering and property

modifications. Even the columnar architecture is not limited by the substrate-clamping effect and also increases the vertical interfacial area as well many magnetic or electrical properties. A breakthrough is further expected due to the rapid advancement of the modern technology and increasing demands from the community. For example, as mentioned above, LSMO has been coupled with many secondary phase (e.g. MgO, ZnO, NiO, CeO_2, etc) and formed VAN thin films with highly enhanced magnetotransport properties for spintronic applications. Compared with the original LSMO epitaxial films with magnetoresistance of ~5-10%, the reported LSMO-based VAN films have improved the magnetoresistance up to 40%. But there is space for more advancements.

Meanwhile, we have noticed that new strain engineering is always accompanied by microstructure and interface evolution. It has evolved from the epitaxial and multilayer films with lateral strain engineering to the VAN configuration with vertical strain engineering. Creative and complex microstructures with unique strain and interfacial engineering are expected.

CHAPTER 2. EXPERIMENTAL TECHNIQUES

Recently the rapid development of material synthesis and characterization methods has boosted a deeper understanding in the fundamentals and provoked an unprecedented growth of the complex oxide thin films in the novel multifunctional devices.

2.1 Pulsed Laser Deposition

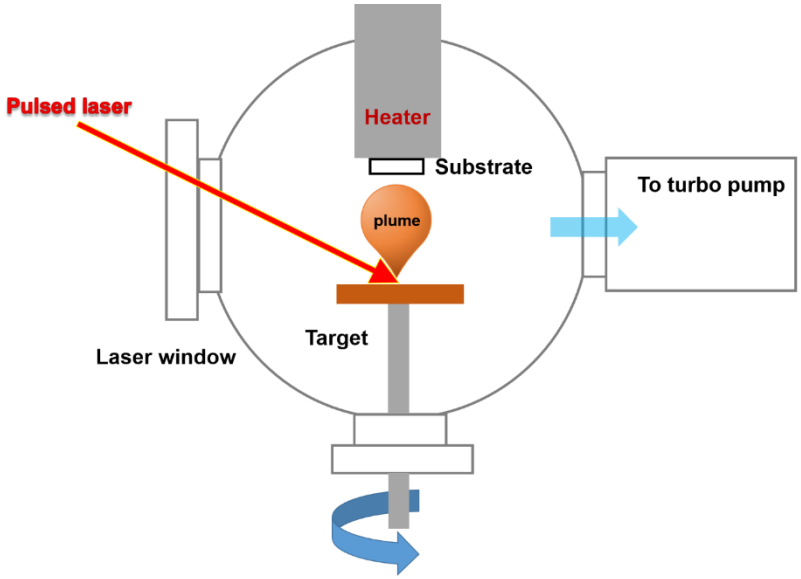

Figure 2.1 Schematic illustration showing a typical pulsed laser deposition system with one target in the chamber.

Thin film growth deposition plays the key role in the modern device production. Within the wide variety of thin film growth techniques, physical vapor deposition is quite suitable for complex oxide thin film growth as it offers stoichiometric deposition and is able to artificially create films by layering the compounds onto the substrates easily. During physical vapor deposition (PVD), the vaporized materials (e.g., various species such as electrons, ions, atoms,

molecules, clusters, and particulates) generated from the target are condensed onto the substrate surface and form polycrystalline or epitaxial thin films. Within the various PVD methods (e.g., molecular beam epitaxy, pulsed laser deposition, chemical vapor deposition, sputtering, etc.), pulsed laser deposition (PLD) has been attracting substantial interest for decades since it was used to prepare semiconducting, dielectric, and also high-quality superconducting films in 1980s.[4, 82-84]

PLD has been serving as an extraordinarily powerful and convenient tool to grow high-quality thin films under high oxygen background pressure for the scientific community as well as industry. It operates at nonequilibrium and provides a broad range of tunabilities and parameters for strain, microstructural, and interfacial engineering in the functional oxide film growth.[85]

Figure 2.1 presents the schematic set-up of a typical PLD system, which consists of a pulsed laser source, a substrate holder, a target holder and a vacuum chamber which is connected with a first level mechanical pump and a second level of turbo pump. The pulsed laser source switches the laser with respect to time in an alternating fashion of "on" and "off" modes. The substrate holder is attaching to a heater, which is able to heat the substrate up to ~800 °C. The vacuum chamber usually contains multiple target holders to accommodate multiple targets for the multilayer growth. The distance between substrate and target is mainly maintained at ~4.5 cm and the incident laser angle is ~45° in this thesis. The PLD chamber is usually pumped down to a base pressure lower than 10^{-6} mTorr by a turbo pump combined with a mechanical pump. After the evacuation, the substrate temperature is maintained at ~650-750 ˚C and the oxygen pressure at 200 mTorr in the chamber for film deposition. The pulsed laser beam with a wavelength of ~248 nm is focused on to the surface of the target by a series of external lenses during the deposition. The laser frequency is controlled at 1-10 Hz and the energy at ~420 mJ for the work in this thesis. Once

the laser is incident on the target surface, ablation of the target surface occurs due to the interaction between the high-energy laser and the target. This laser-target interaction is shown in Figure 2.2 with the electromagnetic energy of the laser pulse transferred into thermal energy which melts and vaporizes the target surface.[84, 86, 87] Then a plasma is created with small particles or clusters ejected from the target surface. The plasma plume travels in oxygen and condenses onto the substrate surface at the given growth condition, forming the thin film layer on top of the substrate. At this moment, the substrate temperature is maintained at ~650-750 ˚C, which is tunable and contributes to the surface diffusion of adatoms during the film growth. After sufficient laser pulses, the deposition is complete and the film is cooled down at 10 ˚C/min to room temperature under the oxygen pressure of 200 Torr.

This growth process reveals that the deposition parameters are essential to determine thin film quality and structure, including substrate temperature, oxygen pressure, distance between substrate and target, laser energy, laser frequency, and cooling rate. These deposition parameters are able to directly influence the stoichiometry, structures, crystallinity and roughness of the as-prepared thin films and further contributed to the physical performances of the films.[88] Moreover, the substrate selection and its structural compatibility with the film are also considerably critical for obtaining the desired films.[48]

Therefore, the PLD provides us the ability to control the film growth and design the film structure according to the practical application needs. Besides the tunability, PLD also exhibits many priorities compared with other deposition techniques (e.g., MBE and CVD). For example, PLD can deliver a stoichiometry transfer from the target to the deposited film since the plume is generated and transferred immediately on to the substrate. This enables PLD widely employed in a rich spectrum of materials, such as oxides, nitrides, metals, and so on. Also, the PLD can grow

thin films very efficiently at a high growth rate which doesn't have to require extremely high vacuum condition. PLD is applied as the film growth approach in this work. Moreover, increasing companies have used the industrial scale PLD in their chip or device fabrication especially for semiconductors, indicating the big transition of this technique from research labs to practical applications for large production in industry.

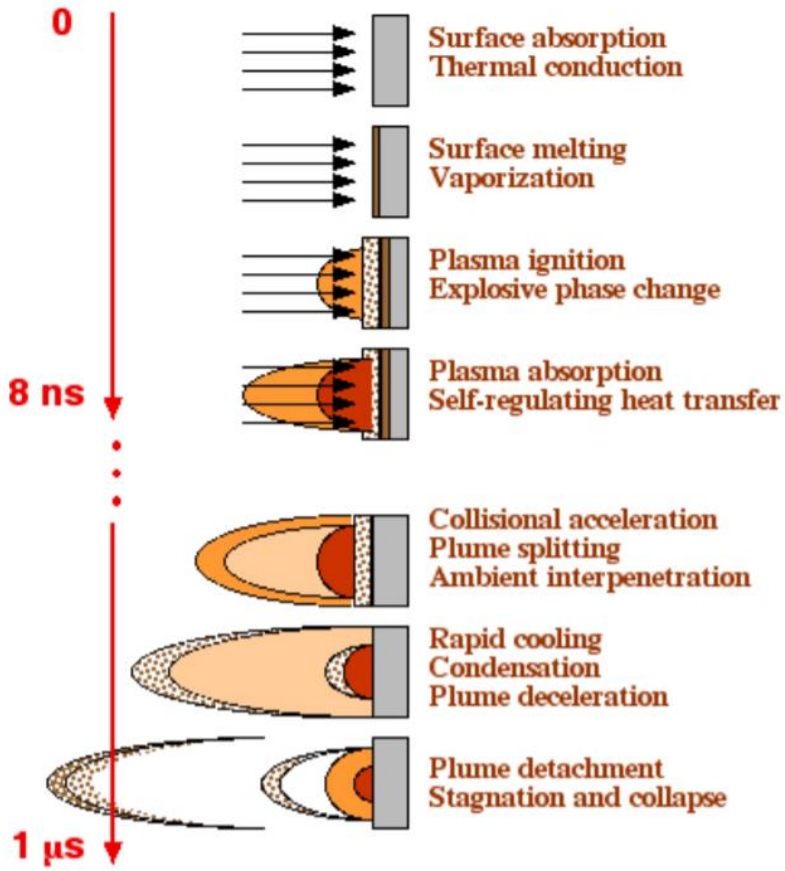

Figure 2.2 Schematic illustration of the laser-target interaction during short pulsed laser period, including plume creation, expansion and condensation.[86]

2.2 Structural Characterization

2.2.1 X-ray diffraction

X-ray diffraction (XRD) is one of the most popular structural characterization tools in materials science and has been widely used in powder samples, polycrystalline materials, single crystals, thin films and devices. It is nondestructive, efficient and reliable to provide crystallographic information such as phase, crystal structure, lattice parameter, crystallinity, growth orientation, size, spacing of the lattice, and more.[89] Those information can be directly drawn or calculated from the experimental results.

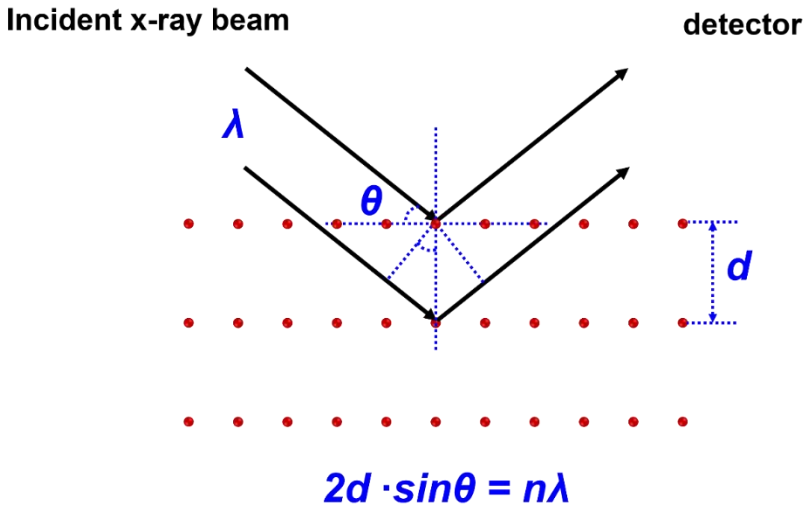

Figure 2.3 Schematic illustration showing x-ray diffraction on a crystal with inter-plane spacing of d.

As shown in Figure 2.3, a XRD instrument consists of an incident X-ray source, a sample stage and x-ray detector. When the X-ray is incident on the crystalline materials, diffraction occurs and fulfills the Braggs' equation,

$$n\lambda = 2d \cdot sin\theta \quad (2\text{-}1)$$

where n is an interger, λ corresponds to the wavelength of x-ray (λ = 1.54056 Å for Cu Kα), d represents the lattice spacing of the crystalline materials, and θ is the incident angle. For crystalline materials with long-range order and periodic spacing, diffraction peaks can be observed in the XRD patterns. No peaks can be observed in the XRD patterns of amorphous materials.[90]

In epitaxial thin films, the peak position, intensity and width of the XRD θ-2θ scan can be used to resolve the film phase, crystallinity, growth orientation, crystallite size, lattice parameter and epitaxial strain. The crystallinity of the material is estimated from the full width at half maximum of the peak. Narrow peak represents high crystallinity of the films. The lattice parameters can be calculated according to the peak position in the XRD pattern and the Braggs' equation. The epitaxial strain of the films can be resolved from either the diffraction peak shift from its original position (uniform strain) or the peak broadening (nonuniform strain) in the XRD pattern (Figure 2.4 (a-c)).[91] Take the epitaxial VO_2 films deposited on TiO_2 substrates as an example. With gradually increased film thickness from ~1.6 nm to ~74 nm, the epitaxial VO_2 films exhibit a peak shift to lower angle direction corresponding enlarged d-spacing as shown in Figure 2.4 (d).[92]

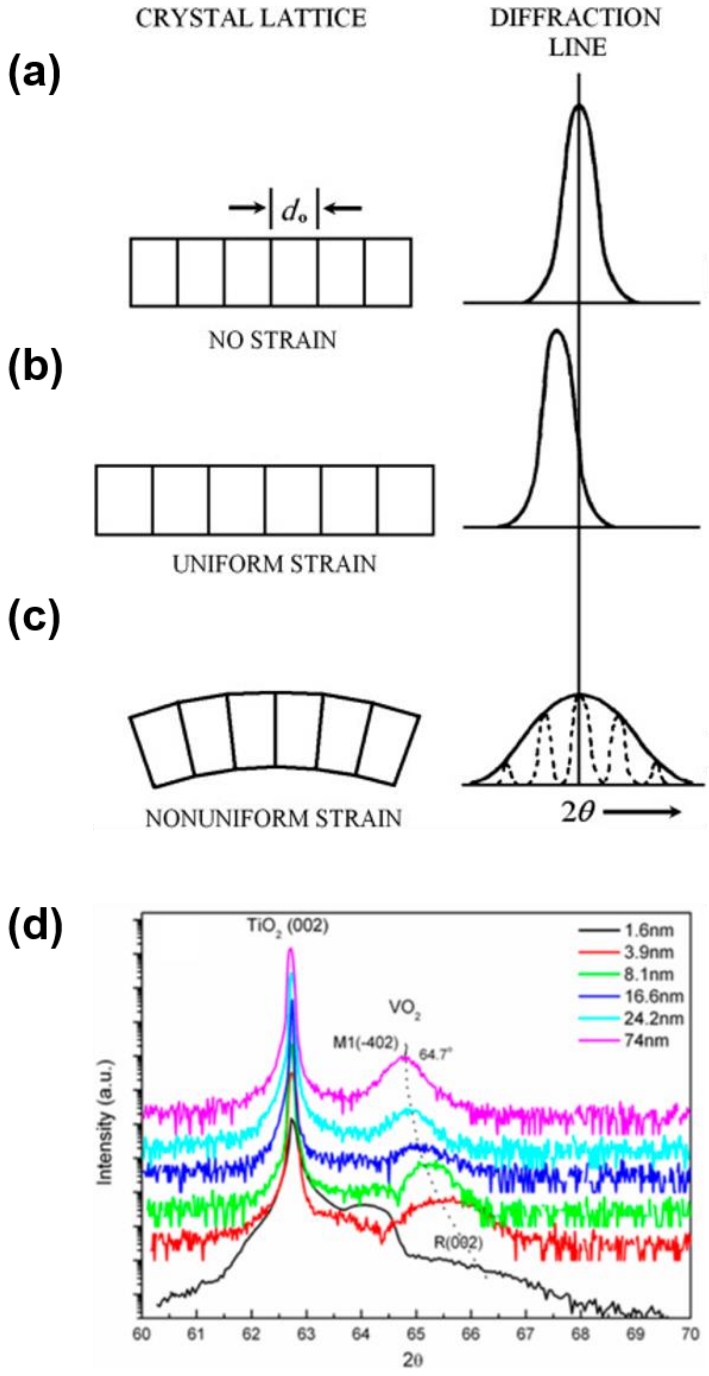

Figure 2.4 Influence of different epitaxial strains on the peak position and width in x-ray diffraction (XRD): (a) no strain, (b) uniform strain, and (c) nonuniform strain.[91] (d) XRD θ-2θ patterns of the epitaxial VO_2 thin films with gradually increased film thickness grown on TiO_2 substrates.[92]

Besides the θ-2θ scans, reciprocal spacing mapping (RSM) is another common tool which can be used to evaluate the epitaxial quality, lattice parameter and strain of thin films along the

selected planes. RSM is able to provide the crystallographic information along both in-plane and out-of-plane directions simultaneously, as long as the targeted plane contains both dimensions' information. The common selected planes include (112), (113) and (103), in which the lateral and vertical lattice distortion information can be judged according to the peak shifts. For example, the RSM mapping in Figure 2.5 reveals the evolution of strain states in VO_2 films with the film thickness increasing from ~1.6 nm to ~74 nm. The VO_2 (112) peak in Figure 2.5 (a) exhibits negligible horizontal change, suggesting that this ultrathin VO_2 film is fully strained after coupling with the TiO_2 substrate. When the VO_2 film is getting thicker, the VO_2 (112) peak gradually deviates from TiO_2 (112) with enhancing peak intensity, corresponding to the gradually relaxed strain in VO_2 films (Figure 2.5 (b) and (c)). When the film thickness reach ~74 nm, the VO_2 film is fully relaxed as shown in Figure 2.5 (d). All the peak spots in Figure 2.5 reveals good epitaxial growth quality of these VO_2 films on TiO_2 substrates.[92] The similar peak deviations or shifts in RSM are observed to estimate the strain variations in previous reports.[93, 94] The drawback of the RSM technique is the spatial resolution. Therefore, the lattice and strain variations can be qualitatively estimated on RSM. For higher resolution and accuracy, a synchrotron x-ray diffraction is needed.

Moreover, there are many other powerful measurements which can be conducted in XRD to study crystalline materials. For example, the φ scans are conducted to study the domain orientation of the film or lattice coupling relation between different phases. Rocking curve can be used to determine the lattice distortion and crystal orientation. Pole figure is very popular to exam the growth texture of polycrystalline thin films.

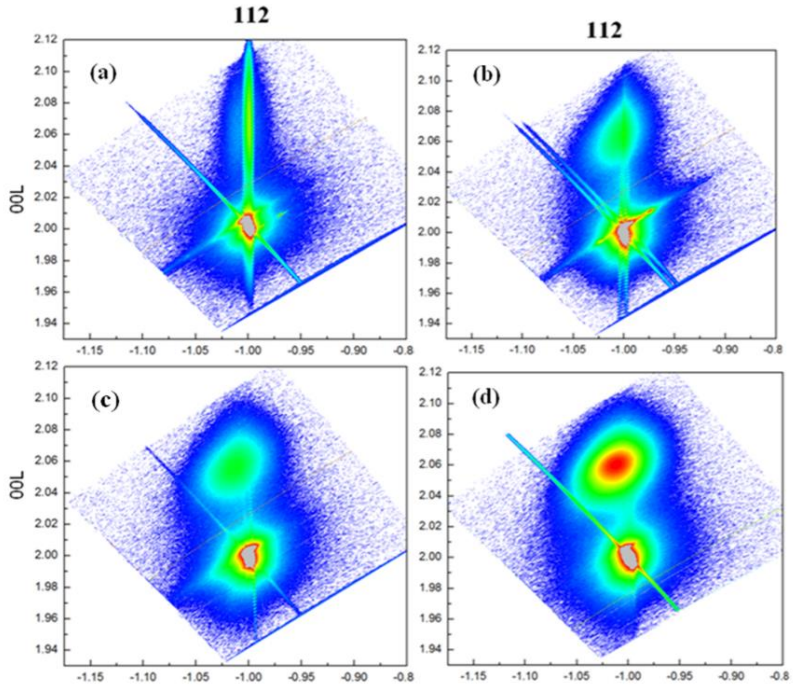

Figure 2.5 Reciprocal space mapping of the epitaxial VO_2 thin films grown on TiO_2 substrates along TiO_2 (112) direction with different film thickness of (a) ~1.6 nm, (b) ~16.6 nm, (c) ~24.2 nm and (d) ~74 nm.[92]

2.2.2 Transmission electron microscopy

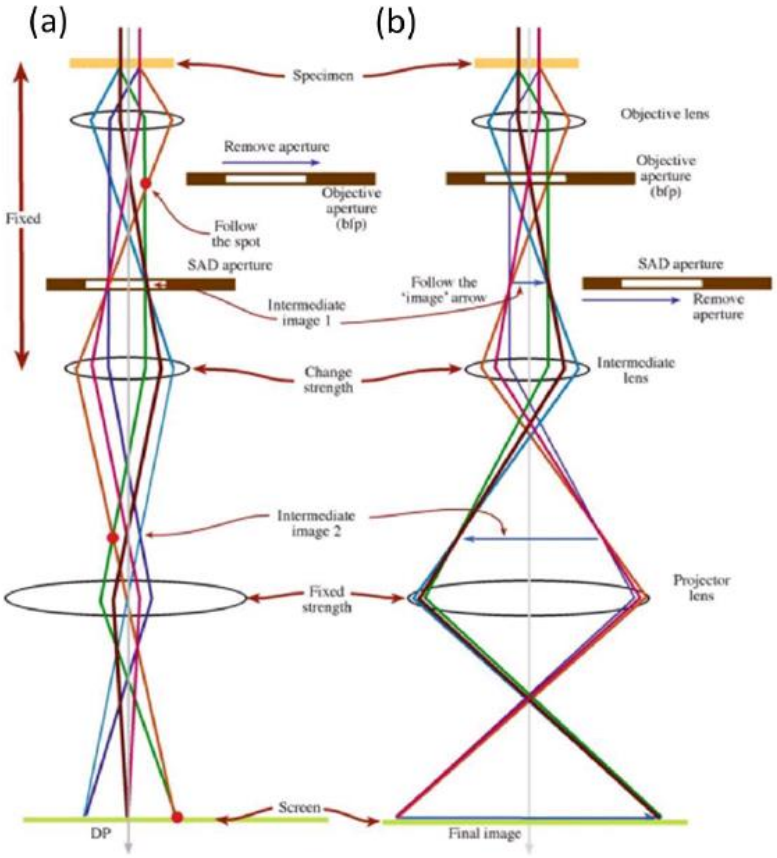

Figure 2.6 Two basic operation modes of the transmission electron microscopy: (a) diffraction mode, and (b) imaging mode.

Transmission electron microscopy (TEM) is considered as a very popular, versatile and powerful tool in materials characterization and fundamental studies. Similar to optical microscopy, TEM applies electron beam to penetrate through a very thin sample (thickness is or less than ~100 nm) and interact with this sample while it travels through the sample. Instead of visible light, TEM makes use of traveling electron beam and achieves way much higher image resolution (~ a couple of angstroms) which optical microcopy cannot reach. With the help of TEM, researchers can not only directly observe the structure of the sample in the imaging mode at very high magnifications,

and also obtain quite significant information, such as crystallographic, chemical and more information, caused by the interplay between the specimen and the electron beam.

A typical TEM system mainly contain the following four parts: illumination system, electromagnetic lens system, sample holder, and imaging system. They are all assembled within a high vacuum column which are connected to a mechanical pump and turbo pump. The illumination is composed of the gun and condenser lenses, which transfers the electron beam from the source to the specimen. The electron source plays a critical role in determining the TEM image quality. The illumination system has two operation modes: (1) parallel beam for the TEM imaging and electron diffraction, (2) convergent beam for STEM imaging and element analysis. The TEM operation on the electromagnetic lens system is to focus and confine the electron beam before interacting with the specimen for high quality images. The objective lens mainly determines the image quality as it generates the first image. The cutting-edge aberration-corrected TEM can obtain highly enhanced image quality and resolution, as the spherical aberration at objective lens is minimized by the corrector. The TEM resolution is mainly determined by the electron beam and aberration of lens. The regular TEM sample holders are mainly classified into two types: single-tilt and double-tilt holders. Double-tilt TEM holder is applied for the work in this thesis. The image system has two systems of lenses—one for magnifying the image and the other for projecting the image onto screen. Worth mention that STEM has a CCD camera system to detect the electron beam and create STEM images. Therefore, the final magnification of TEM is the collective result of the magnifying power from objective lens, intermediate lens and projecting lens.

TEM has two major operation modes—imaging mode which provide visualization information and diffraction mode which provides electron diffraction information (Figure 2.6). The operator can easily switch between the two modes by varying the focal length between the

image plane (for imaging mode) and the back focal plane (for diffraction mode). In imaging mode, the objective lens is placed at its image plane with the focal length of the intermediate lens modulated to project the view on the imaging screen. In this way, the microstructure of the sample can be visualized. To obtain the local view of the atom arrangement at high magnification, the sample needs to be tilted and aligned to a right zone axis. In diffraction mode, the electron beam is refocused at the back focal plane, generating the electron diffraction pattern of the specimen. Similar to x-ray diffraction, the electron diffraction pattern can provides local structural information such as crystal structure and lattice parameter of the specimen.

In imaging mode of TEM, researchers can gain both dark field (DF) and bright field (BF) images (Figure 2.7) by tuning the objective aperture configuration and the beam diffraction. The BF images can be gained when the objective aperture is placed to let the direct transmitted electron beam pass through. In contrast, one can obtain DF images by changing the objective aperture position to let only a certain portion of diffracted electrons pass through. Only the domains along a certain orientations of the sample show up in bright contrast on the screen and can be imaged in DF mode operation, since the filtered beam only deliver the information along a certain diffraction planes. The areas along other directions are shown in dark contrast.

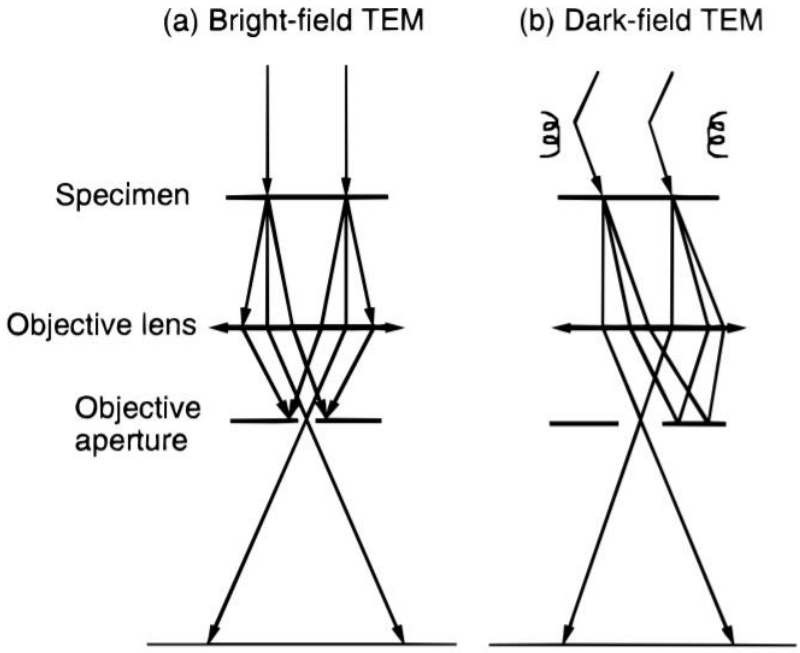

Figure 2.7 Schematic diagram showing (a) bright-field and (b) dark-field imaging mode in TEM.[95]

Scanning transmission electron microscope (STEM) mode is also frequently used in TEM where the electron beam is convergent into a probe, parallel to the optic axis, and keeps scanning the scanning the specimen. Due to its scanning nature, STEM mode is often used in high-angle annular dark field imaging (HAADF), element chemistry analysis, and electron energy loss spectroscopy. The imaging contrast is directly related to Z^2 (Z represents the atomic number) in the HAADF STEM mode, which can be used to directly differentiate the different phases or compounds. Thus researchers use the STEM mode more regularly to study the heterogeneous structure or heterepitaxial interfaces.

TEM is heavily utilized in this thesis to characterize the microstructures of those nanocomposite thin films, investigate the lattice coupling relations along interfaces, and help to deliver strain mapping studies. The TEM facilities involved in this work include an FEI TALOS

F200X FEG S/TEM at 200 kV equipped with ultrahigh resolution high angle annular dark field detectors and Supper-X^{TM} electron-dispersive x-ray spectroscopy, an aberration-corrected FEI Titan microscope equipped with a high brightness Schottky-field emission electron source operated at 300 kV, and a Themis Z aberration corrected 300 kV FEG S/TEM (including double correctors and monochromator). Double-tilt TEM holders are needed for the material characterizations here.

2.2.3 Geometric phase analysis

As mentioned above, the lattice parameter and calculated strain from XRD data is average results from the detected sample globally. Strain mapping is needed to obtain a direct observation of the strain distribution or variation. In this thesis, the visualization of strain mapping is obtained through a commercial program called geometric phase analysis (GPA) program (a plug-in for Digital Micrograph package, HREM Research Inc.). The GPA strain map is generated from high resolution TEM or STEM images by the GPA program. The strain in GPA (ε^{GPA}) is derived according to the following equation

$$\varepsilon^{GPA} = \frac{d_{hkl}^{local} - d_{hkl}^{reference}}{d_{hkl}^{reference}} \quad (2\text{-}1)$$

where d_{hkl}^{local} and $d_{hkl}^{reference}$ represent the d-spacing of a certain plane (*hkl*) of the local area and the reference area, respectively. Thus, the GPA strain map gives a visualization of the relative strain variations compared with the reference region, but cannot give the absolute strain values. The relative lattice variations can be dictated from the sign of the strain ε^{GPA}: "+" presents enlarged lattice and "-" means reduced or shrinked lattice compared with the reference lattice. The GPA program conducts the relative strain calculation according to the contrast change across the

HRTEM/HRSTEM images. Also, it only can give a rough strain relative variations in a small area, which is judged according to the color contours of the GPA strain map.

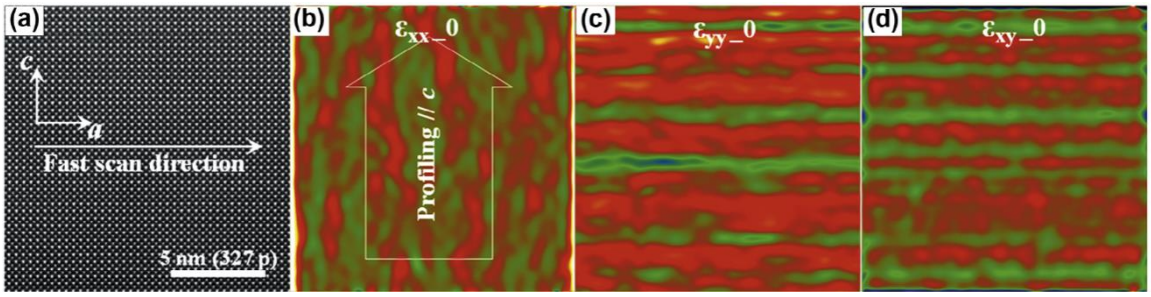

Figure 2.8 (a) HRSTEM image of the STO substrate along<001> zone axis. (b-d) The corresponding GPA ε_{xx}, ε_{yy} and ε_{zz} maps of (a).[96]

2.2.4 TEM sample preparation

As mentioned above, TEM is such a powerful characterization tool with many enchanting superiorities. However, TEM also has a drawback which limits its application—TEM requires the specimen's thickness below ~100 nm so that the electron beam can penetrate through the specimen and deliver effective results. The key to a clear TEM images is to prepare fine TEM sample with thin area less than ~100 nm. Samples need different procedures to be prepared for TEM observation according to their dimensions. For nanoparticles or quantum dots, TEM grids are commercially available with or without carbon film according to the customers' needs. However, the TEM grid can't work for the brittle ceramic thin films grown on crystalline substrates. More importantly, cross-sectional and plan-view samples are both needed in this work to study the films' microstructure from different angles.

In this work, we used a special TEM sample preparation procedures. To prepare a cross-sectional TEM sample, the procedure includes the following five steps: (1) cutting off two small pieces (~3 mm×3 mm) from the thin film sample; (2) attaching the two film sides together face-to-face into a disk and heating for 4 hours to solidify the glue; (3) Thinning the disk down to ~60

μm; (4) careful grinding down below ~30 μm and polishing; (5) ion milling which can ensure the sample less than 100 nm thin. The final ion milling step needs careful consideration of the beam energy, vacuum condition, and incident angle. For a plan-view TEM sample, the procedure is quite similar to the cross-sectional and skips the step (2) by direct thinning the sample from the backside. Then grinding, polishing and ion milling steps are followed.

2.3 Property Characterization

Magnetotransport and magnetization properties of the thin films are measured on a Physical Property Measurement System (PPMS-Quantum Design DynaCool) and Magnetic Property Measuremen System (MPMS-3 Quantum Design), respectively.

This PPMS has a stable and accurate control on a wide temperature range from 1.8 K to 400 K and the magnetic field in the range of -9 T to +9 T. By using liquid helium and heater the temperature sweeping speed can be controlled from 0.01 K/min to 15 K/min. The sample space is 25 mm in diameter. It is able to conduct a wide variety of automated measurements for the research of magnetic materials, semiconductor transport, phase transitions, photovoltaics, thermoelectrics, and superconductivity. In general, this PPMS has three options—resistance/magnetoresistance, Hall effect and I-V curves measurements for electrical transport properties. In this thesis, the magnetotransport measurements are conducted by two modes electrical transport (ETO) and resistivity (R-T) on this PPMS. The maximized current in ETO is ~100 mA so that the resistance that ETO can measure ranges from 1μΩ to 10 MΩ. On the other hand, the maximized current of R-T measurement mode can reach 5 mA with the resistance range from 10 μΩ to 1 MΩ. Before the resistance measurements, the film surfaces need to be cleaned and dried. Then four gold contacts are deposited onto the film surface in a four point probe configuration (van der Pauw geometry) with application of masks via sputtering or PLD. During the measurements, one needs

to make sure that the sample is thermally conducted but electrically isolated. The magnetic field of around 1 T is applied along out-of-plane direction of the sample with the temperature sweeping range of 10 K to 390 K. The PPMS measures the current going through two contacts and also the voltage through the other two gold contacts. The resistivity can be calculated by Ohm's law and the dimension of the films.

The PPMS has a vibrating sample magnetometer (VSM) option for the magnetic property measurements which determine the DC magnetic moment of the sample. The main drawback of this VSM option is lack of accuracy. Compared with the VSM option equipped on the PPMS, MPMS delivers more fast, sensitive and accurate measurements. The full magnetic hysteresis loops can be achieved within several minutes. It can accommodate the sample space of 8 mm diameter for bulk, crystal, film, and powdered samples. The temperature control on MPMS is 1.8 K-400 K and 300 K-1000 K equipped with an oven. Field control range can be controlled from -7 T to +7 T. The measurements involved in this thesis is mainly the magnetization hysteresis loops with the magnetic field applied along in-plane and out-of-plane directions. The magnetic properties of the thin films are measured at around 300 K.

CHAPTER 3. THREE-DIMENSIONAL STRAIN ENGINEERING IN EPITAXIAL VERTICALLY ALIGNED NANOCOMPOSITE THIN FILMS WITH TUNABLE MAGNETOTRANSPORT PROPERTIES

(This chapter is reprinted with permission from "*Three-dimensional strain engineering in epitaxial vertically aligned nanocomposite thin films with tunable magnetotransport properties*" by X. Sun, et al., Materials Horizons, 5, 536-544 (2018).)

3.1 Overview

Three-dimensional (3D) frameworks have been successfully constructed by interlayering $La_{0.7}Sr_{0.3}MnO_3$ (LSMO)-CeO_2 based epitaxial vertically aligned nanocomposite (VAN) thin films with pure CeO_2 (or LSMO) layers. Such 3D interconnected CeO_2 scaffolds integrate the lateral film strain by the interlayers with the vertical strain in VAN layers, and thus achieve the maximized strain tuning in LSMO. More importantly, by varying the types of the interlayers (i.e., CeO_2 or LSMO) and the number of interlayers from 1 to 3 layers, such 3D framework nanostructures effectively tune the electrical transport properties of LSMO, e.g., from 3D insulating CeO_2 framework with integrated magnetic tunnel junction structures, to 3D conducting LSMO frameworks, where the magnetoresistance (MR) peak values have been tuned systematically to a record high of 66% at 56 K and enhanced MR properties at high temperatures above room temperature (~325 K). This new 3D framed design provides a novel approach in maximizing film strain, enhancing strain-driven functionalities, and manipulating the electrical transport properties effectively.

3.2 Introduction

ABO_3-based perovskites have attracted substantial research interests and been widely applied in various modern electronic devices, because of their versatile electrical and magnetic properties, such as superconductivity, colossal magnetoresistance (CMR), ferroelectricity, ferromagnet, and multiferroicity.[97-104] The physical properties of perovskite oxides are mainly determined by their building blocks-BO_6 octahedral units. Constructed by B-site transition metal cation coordinating with six oxygen ligands, BO_6 octahedral units interconnect with each other by sharing corners and form a three-dimensional (3D) framework. Altering size, shape, and connectivity pattern of those units can directly tune B-O-B bonds, crystal structure, and subsequently perovskite oxides' physical responses.[40, 105] Strain engineering has been agreed on as one of the most effective approaches in tuning the octahedral units, crystal structure, spin ordering in perovskites and, in turn, the physical properties of these perovskite oxides.[40, 48, 106, 107]

Great efforts have been devoted to exploring effective strain engineering approaches. One of the most effective approaches is substrate strain control where various substrates with different lattice parameters are explored for in-plane strain control.[4, 49, 53] The approach provides effective lateral strain tuning in relatively thin films (within the critical thickness of a few nanometers) since the substrate strain is relieved with increasing film thickness.[68, 108] In parallel, implementing heteroepitaxial 2-phase nanocomposite thin films can incorporate additional interfacial strain into the matrix film through interface coupling between the two phases, such as zero-dimensional (0D) nanoparticles in matrix, two-dimensional (2D) multilayered films, and very recently, vertically aligned nanocomposite (VAN) thin films.[7, 31, 54, 63, 64, 68, 109-114] In VANs, the lattice strain can be maintained in much thicker films because of the vertical

interface coupling. In addition, the density of the secondary phases, column dimensions and morphologies are also major factors in the strain tuning of VAN films. Using VANs, a broad range of multifunctionalities, such as multiferroicity, ferroelectricity, low field magnetoresistance (LFMR), and anisotropic electrical/ionic transport properties have been demonstrated.[64, 107, 108, 110, 111, 115]

Estimated as state of the art, 3D nanostructured materials such as branched nanorods or nanoforests have been rapidly attracting dramatic attentions. As they fully make use of vertical and horizontal dimensions and exhibit many impressive advantages, i.e., highly enhanced interfacial area and stability, derived from their 3D architectural characteristics compared to one-dimensional (1D) nanowire arrays.[116-120] However, this concept of 3D nanostructures has not been applied in the epitaxial thin films yet. To take advantages of the above strain control approaches and to explore the ultimate strain control in those films, in this work, we propose a 3D strain architecture to combine the lateral strain introduced by layered interface and the vertical strain from vertical interface in VANs (as illustrated in Figure 3.1). More specifically, this 3D strain control is achieved by alternative growth of the single phase and the VANs in multilayer fashion. $La_{0.7}Sr_{0.3}MnO_3$ (LSMO) is selected as the matrix for this 3D strain design as it has shown high CMR effect, magnetic anisotropy, spin-glass like behavior, and LFMR properties.[107, 110, 121, 122] Various secondary phases have been demonstrated for enhanced LFMR in LSMO VAN films.[109, 121-124] CeO_2 is selected as the insulating secondary phase embedded in the LSMO matrix, because of its good in-plane lattice match with LSMO and STO after a 45º in-plane rotation (Figure 3.1), as well as its high thermal/mechanical stability.[112, 121, 123] Furthermore, CeO_2 can serve as insulating layer favoring spin-dependent tunneling, easier to explore synergistic effects between strain tuning and the LFMR effect.

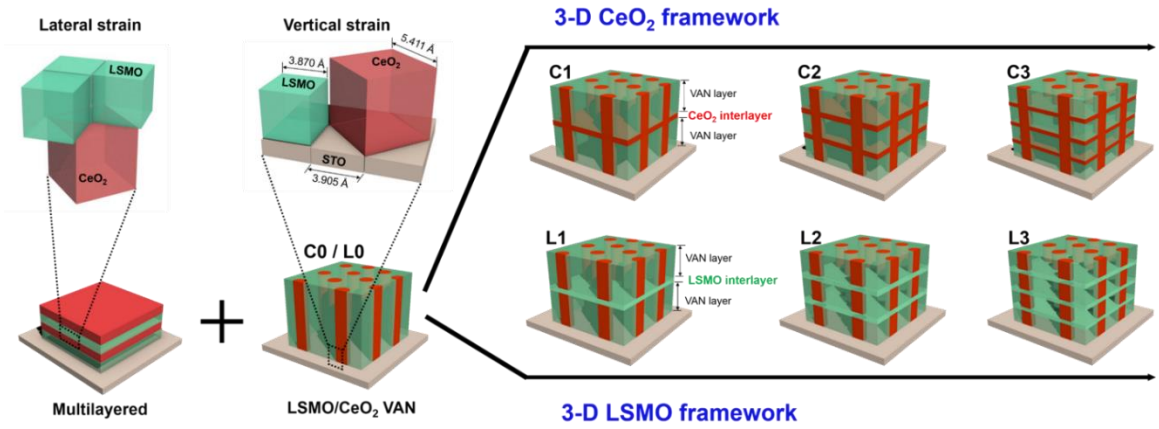

Figure 3.1 Schematic illustration of 2-phase heterogeneous microstructure evolution of the thin films: from vertical aligned nanocomposite (VAN) C0/L0 to 3D CeO_2 framed thin films C1-C3 and 3D LSMO framed thin films L1-L3. The 3D framed microstructure is achieved by alternative growth of the single phase and the VANs in multilayered fashion. This design combines the lateral strain introduced from multilayered thin film and the vertical strain from interfacial coupling in VANs, creates 3D interconnected CeO_2 or LSMO framework microstructures within the thin films, and provides a versatile tool to achieve 3D strain tuning. The unit cells and phase of LSMO are in green, and the unit cells and phase of CeO_2 are in red.

As illustrated in the left panel of Figure 3.1, we have selected either CeO_2 or LSMO single layer to construct the 3D CeO_2 framework or the 3D LSMO framework, respectively. More specifically, single layer LSMO-CeO_2 (molar ratio of LSMO:CeO_2 = 1:1) VAN thin films were prepared as control experiments and named as C0 or L0, without LSMO or CeO_2 as interlayers. 3D CeO_2 interlayered thin films with 1, 2, and 3 interlayers inserted in VAN structures are named as samples C1, C2, and C3, respectively. Similarly, 3D LSMO interlayered thin films with 1, 2, and 3 interlayers inserted in VAN are named as sample L1, L2, and L3, respectively. To explore the power of 3D strain effects offered by the 3D framework built in the LSMO-CeO_2 VAN systems, the molar ratio of LSMO and CeO_2 is maintained at 1:1 in the VAN layers. Such ratio was selected based on the previous reports where effective tunneling effects from the secondary phase have been found.[31, 65, 121, 122] This set of interlayered samples are expected to combine the vertical strain control by VAN structures and lateral strain control by the interlayers and to achieve 3D

strain modulation. LFMR properties are measured and correlated with the strain in these 3D strained frameworks.

3.3 Experimental

3.3.1 Target preparation

Targets of pure LSMO, pure CeO_2, and composite LSMO-CeO_2 (molar ratio 1:1 of LSMO and CeO_2) were prepared via conventional ceramic sintering process. A stoichiometric mixture of La_2O_3, MnO_2, and $SrCO_3$ powders were ground, pressed into a disk, and annealed at 1300 °C in air for 12 h to form pure LSMO target. The same procedure was also employed to synthesize CeO_2 target at 1200 °C for 6 h and LSMO-CeO_2 target at 1300 °C for 12 h, respectively.

3.3.2 Thin film growth

3D LSMO-CeO_2 framed nanocomposite films were grown on $SrTiO_3$ (STO) (001) substrates via a pulsed laser deposition (PLD) approach with KrF excimer laser (λ = 248 nm). Before deposition, the chamber was evacuated to a base pressure of 1.0E-6 Torr (1 Torr = 133.3 Pa) or below. During deposition, the substrates were maintained at 750 °C and the oxygen pressure was controlled at 200 mTorr with a laser frequency of 1 Hz. After deposition, the substrates were cooled down at a ramp rate of 10 °C min^{-1} under an oxygen pressure of 200 Torr.

To synthesize 3D framed nanocomposite films with distinct nanostructures, detailed deposition pulses on each target were summarized in Table 3.1 and 3.2, including VAN thin films C0/L0, 3D CeO_2 framed thin films C1-C3, and 3D LSMO framed thin films L1-L3, respectively. Sample C0 has no lateral CeO_2 interlayer which is the typical LSMO-CeO_2 VAN structure. From sample C1 to C3, the CeO_2 interlayer number gradually increases from 1 to 3.

Table 3.1 Synthesis Condition for 3D Framed Thin Films with Pure CeO_2 as Interlayer

Sample NO.	**LSMO-CeO_2**	**CeO_2**	**LSMO-CeO_2**	**CeO_2**	**LSMO-CeO_2**	**CeO_2**	**LSMO-CeO_2**
C0	2400	0	0	0	0	0	0
C1	1200	120	1200	0	0	0	0
C2	800	120	800	120	800	0	0
C3	600	120	600	120	600	120	600

Table 3.2 Synthesis Condition for 3D Framed Thin Films with Pure LSMO as Interlayer

Sample NO.	**LSMO-CeO_2**	**LSMO**	**LSMO-CeO_2**	**LSMO**	**LSMO-CeO_2**	**LSMO**	**LSMO-CeO_2**
L0	2400	0	0	0	0	0	0
L1	1200	120	1200	0	0	0	0
L2	800	120	800	120	800	0	0
L3	600	120	600	120	600	120	600

3.3.3 Characterization

The phase and orientation of the thin films were characterized by x-ray diffraction (XRD) (2θ-ω and ϕ scans with Cu Kα radiation, PANalytical Empyrean system). Reciprocal space mapping was also conducted on the same X-ray diffractometer to analyze the strain and d-spacing variations of those thin films. Transmission electron microscopy (TEM) images, and selected-area electron diffraction (SAED) patterns were collected on FEI Tecnai G2 F20 operated at 200 kV. Cross-sectional and plan-view samples for TEM analysis were prepared by a standard procedure-manual grounding, plane-parallel polishing, thinning, and then a final polishing step in ion polishing system (PIPS 691, Gatan). The high-resolution scanning TEM (STEM) images were

collected on an aberration-corrected FEI Titan microscope equipped with a high brightness Schottky-field emission electron source operated at 300 kV. A commercial program, a Digital Micrograph plug-in (DM 1.8.3 package, HRTEM Research Inc.), was used for geometric phase analysis (GPA). The GPA method provides the strain mapping of the entire area based on the atomic spacing variation calculated based on the original STEM images. The out-of-plane strain ε_{yy} is derived to illustrate the local lattice displacement from the reference lattice. The strain in GPA is the relative value and in this work the lateral CeO_2 interlayer area is chosen as reference, which shows with red-green coloration. Due to $\varepsilon_{yy} = (c^{local}\text{-}c^{ref})/c^{ref}$, the sign of ε_{yy} represents tensile ("+") or compressive ("-") the strain in the local lattice is compared to the reference. GPA yields a strain map with color contours to illustrate the location of the relative strains. Since the lateral CeO_2 interlayer area is selected as reference area, the GPA ε_{yy} maps here in this work can only be utilized to analyze the out-of-plane strain distributions of CeO_2 phases. Magnetron sputtering and shadow masks were used to grow Au electrodes onto the surfaces of those thin films as contacts for transport measurements. The magnetotransport properties of those thin films were systematically studied by the Physical Properties Measurement System (PPMS Model 6000, Quantum Design) in a four point probe configuration (in Van der Pauw geometry) with a 1 T magnetic field applied out-of-plane (perpendicular to film plane) and the current applied in-plane. Each sample was first cooled from 350 K down to 10 K without applied magnetic field, and then heated up to 350 K under a magnetic field of 1 T. Electrical resistance was recorded in the temperature range of 10-350 K with and without applied the magnetic field of 1 T. The corresponding magnetoresistance (MR) was calculated by this following equation:

$$\text{MR}\ (\%) = [(R_0 - R_H)/R_0] \times 100\% \quad (3\text{-}1)$$

where R_H and R_0 is the electrical resistance with and without the applied magnetic field of 1 T at the same temperature.

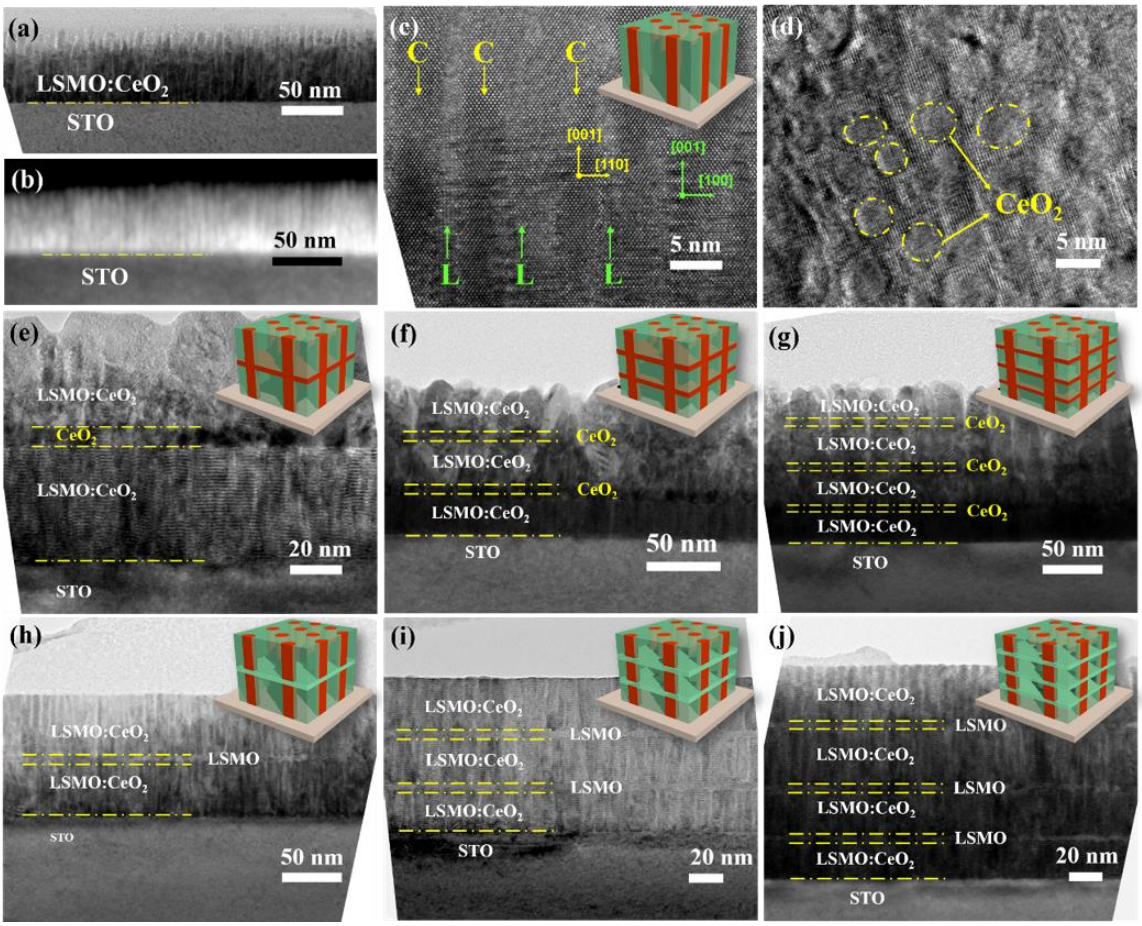

Figure 3.2 (a) Cross-sectional TEM image of the VAN thin film C0 and (b) its corresponding STEM image at low magnification. (c) Cross-sectional and (d) plan-view HRTEM images of sample C0. In the HRTEM image of (c), "C" in yellow points out the CeO_2 nanopillars and "L" in green points out the LSMO matrix. Clearly, those CeO_2 nanopillars with a large aspect ratio are vertically aligned and well distributed in the LSMO matrix and the sharp phase boundaries suggest the well separated growth of the two phases. Cross-sectional TEM images of the thin films (e-g) C1-C3 and (h-j) L1-L3, showing the microstructures of 3D interconnected CeO_2 and LSMO frames embedded within the thin films respectively.

3.4 Results and discussion

Transmission electron microscopy (TEM) and scanning transmission electron microscopy (STEM) images (Figure 3.2) confirm the microstructures of samples C0-C3 and L0-L3. The thickness of all the as-deposited films are around 100-120 nm. A columnar nanocomposite structure with alternative columns of LSMO and CeO_2 can be clearly seen in the VAN thin film C0 from the cross-sectional TEM and corresponding STEM images (Figure 3.2 (a) and (b)), respectively. It is obvious that the CeO_2 nanopillars with large aspect ratio are vertically grown in LSMO matrix as seen from the high resolution TEM (HRTEM) image in Figure 3.2 (c). Uniform distribution of CeO_2 nanopillars in-plane is confirmed from the plan-view TEM image of C0 (Figure 3.2 (d)). These images present clear and sharp interfaces between the LSMO/CeO_2 phases with limited inter-diffusion. In addition, the diameter of the circular-shaped CeO_2 nanopillar domains is estimated to be ~2-5nm. Figure 3.2 (e)-(g) and (h)-(j) present the 3D framed structured samples C1-C3 and L1-L3, respectively. Overall the structures are all grown as the designed 3D framed structures, as shown in the inset. For example, in the 3D CeO_2 framed thin films C1-C3, each CeO_2 interlayer is around 5 nm thick, sandwiched between LSMO-CeO_2 VAN layers, and joined by vertical CeO_2 nanopillars in the VAN layers to form a 3D CeO_2 skeleton embedded in the thin films. Similarly, in the 3D LSMO framed thin films L1-L3, each LSMO interlayer is around 5 nm thick, sandwiched between the LSMO-CeO_2 VAN layers. It is noted that as the number of CeO_2 interlayers increases, the surface roughness increases gradually from C1 to C3. This might be related to the surface roughness introduced by CeO_2 interlayers. In contrast, incorporation of LSMO interlayers maintains relatively smooth film surfaces in L1-L3 without obvious pores on the top surfaces (Figure 3.2 (h)-(j)). Instead, well-defined 3D interconnected LSMO skeletons are clearly observed within the dense films. Overall these VAN thin films are

grown with high epitaxial quality despite the introduced interlayers and comparable with previously reported LSMO-based nanocomposites.[121, 123]

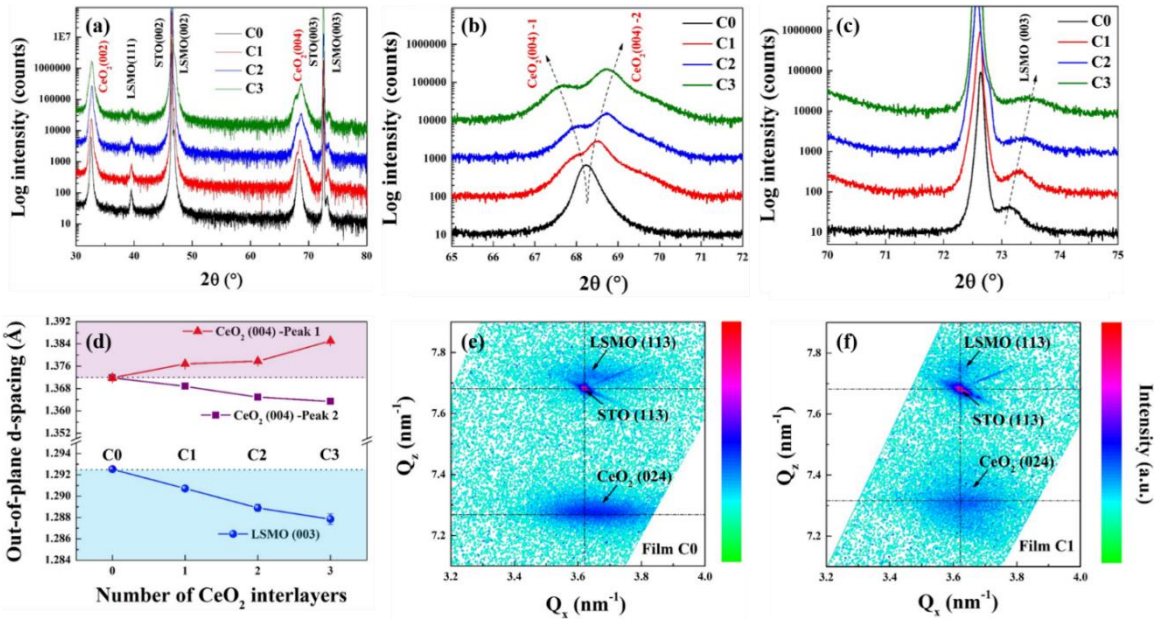

Figure 3.3 (a) XRD 2θ-ω patterns of the VAN thin film C0 and the 3D CeO_2 framed thin films C1-C3. (b) Local CeO_2 (004) 2θ-ω scans of the VAN thin film C0 and the 3D CeO_2 framed thin films C1-C3. (c) Local LSMO (003) 2θ-ω scans of the VAN thin film C0 and the 3D CeO_2 framed thin films C1-C3. (d) Systematic tuning of the out-of-plane d-spacing of CeO_2 (004) and LSMO (003) by the 3D structure engineering in C0-C3 (the d-spacing values and error bars are listed in Table 3.3). The red and purple lines belong to CeO_2 (004) Peak 1 and 2, respectively, while the blue line belongs to the LSMO (003) peak. The pink regime represents the tensile out-of-plane strain area of the CeO_2 phase and the blue regime represents the compressive out-of-plane strain area of the LSMO phase, compared to sample C0. Reciprocal space maps (RSMs) of (e) the VAN thin film C0 and (f) the 3D framed thin film C1 near STO (113). The spots of LSMO and CeO_2 in the RSM reveal the high quality epitaxy growth of the two phases on STO substrates.

Table 3.3 Out-of-plane d-spacing Variation of 3D Framed Thin Films with Different CeO_2 Interlayers

Sample Name	**CeO_2 (004) – Peak 1**	**Error**	**CeO_2 (004) – Peak 2**	**Error**	**LSMO (003)**	**Error**
C0	1.371875	0.000575	1.371875	0.000575	1.292525	0.000188746
C1	1.376825	0.000312	1.3688	0.000187	1.290725	0.000271953
C2	1.377825	0.000239	1.364925	0.000155	1.2889	0.000339116
C3	1.385075	0.000411	1.3631.4	0.000351	1.28785	0.000490748

XRD was employed to study the evolution of the out-of-plane strain in both CeO_2 and LSMO phases as a function of the interlayer structure. Full XRD 2θ-ω patterns of samples C0-C3 are present in Figure 3.3. (00*l*) diffraction peaks for both are present and confirm that CeO_2 and LSMO are grown highly textured along the (00*l*) direction on STO (001) substrates, despite the minor LSMO (111) texture in the films. To reveal the strain of LSMO and CeO_2, local scans of CeO_2 (004) and LSMO (003) are plotted in Figure 3.3 (b) and c for all the C0-C3 samples. It is clear that, as the number of CeO_2 interlayer increases, the CeO_2 (004) peak starts to split into two peaks, i.e., Peak 1 and 2, which are getting further apart (Figure 3.3 (b)). This suggests the coexistence of two different strain states in the CeO_2 phase for the cases of C1-C3. To differentiate the contributions of the two CeO_2 peaks, the XRD data was carefully examined. As the number of the lateral CeO_2 interlayer increases, the intensity and sharpness of Peak 2 (on the right) increases, and Peak 1 (on the left) maintains its similar intensity. It suggests that Peak 2 is attributed to the CeO_2 lateral layers and Peak 1 is from the CeO_2 vertical nanopillars. The origins of the two CeO_2 (004) peaks are further confirmed by strain mapping using geometric phase analysis (GPA) in Figure 3.4, to be discussed later. Simultaneously, the LSMO (003) peak shifts to higher angle as

the interlayer number increases (Figure 3.3 (c)). According to the XRD patterns and Bragg's law, the $d_{(00l)}$-spacing values of both CeO_2 and LSMO phases are calculated (Table 3.3) and plotted in Figure 3.3 (d). In the VAN thin film C0, $d_{CeO2(004)}$ is ~1.372 Å and $d_{LSMO(003)}$ is ~1.293 Å, which are marked with dash lines, respectively. In Figure 3.3 (d), the upper branch (CeO_2 Peak 1) of $d_{CeO2(004)}$ representing the vertical CeO_2 columns gradually increases from 1.377 Å (C1) to 1.385 Å (C3) as the number of CeO_2 interlayers increases. The lower branch (CeO_2 Peak 2) marked in purple represents $d_{CeO2(004)}$ of the lateral CeO_2 interlayers and gradually reduces from 1.369 Å (C1) to 1.363 Å (C3). The out-of-plane strain is calculated and listed in Table 3.4. Compared to the single layer LSMO-CeO_2 VAN sample C0, the vertical CeO_2 nanopillars are in tensile out-of-plane strain of 0.361%. The lateral CeO_2 layer is under compressive out-of-plane strain of -0.224% once the 3D CeO_2 frame is formed in C1. With increasing lateral CeO_2 interlayers in C3, the out-of-plane strain in the 3D CeO_2 framework increases almost three times compared to that of C1. The vertical CeO_2 nanopillars of C3 are under 0.962% tensile strain out-of-plane and the lateral CeO_2 interlayers are under -0.618% compressive out-of-plane. In comparison, from C1 to C3, $d_{LSMO(003)}$ is reduced from 1.291 Å (C1) to 1.288 Å (C3), corresponding to a gradually enhanced compressive strain out-of-plane from -0.139% (C1) to -0.362% (C3). Overall, compared to the reference C0, the out-of-plane strain coupling between the CeO_2 vertical nanopillars and LSMO matrix in C1-C3 is obviously strengthened as the number of CeO_2 interlayer increases, indicating the effectiveness of the 3D strain framework. Figure 3.3 (e) and (f) compare the reciprocal space maps (RSMs) near the substrate STO (113) peak for C0 and C1, respectively. Again, the strain state evolution is further confirmed by the RSM data, i.e., from C0 to C1, the LSMO (113) peak spot is shifted upwards similar to that in Figure 3.3 (c) and CeO_2 (024) is broadened along Q_Z direction reflecting the peak splitting in Figure 3.3 (b). Meanwhile, the 3D LSMO frameworks lessen the

out-of-plane strain coupling between the CeO_2 vertical nanopillars and LSMO matrix in samples L1-L3 with increasing lateral LSMO interlayers (Figure 3.4 and Table 3.5). Accordingly, the strain tunabilty of the epitaxial thin films is mainly decided by the 3D interconnected frames.

Table 3.4 Strain Variation of Sample C0-C3

Sample Name	**Strain on CeO_2 (004) – peak 1/ (%)**	**Strain on CeO_2 (004) – peak 2/ (%)**	**Strain on LSMO (003)/ (%)**
C0	0	0	0
C1	0.361	-0.224	-0.139
C2	0.434	-0.507	-0.280
C3	0.962	-0.618	-0.362

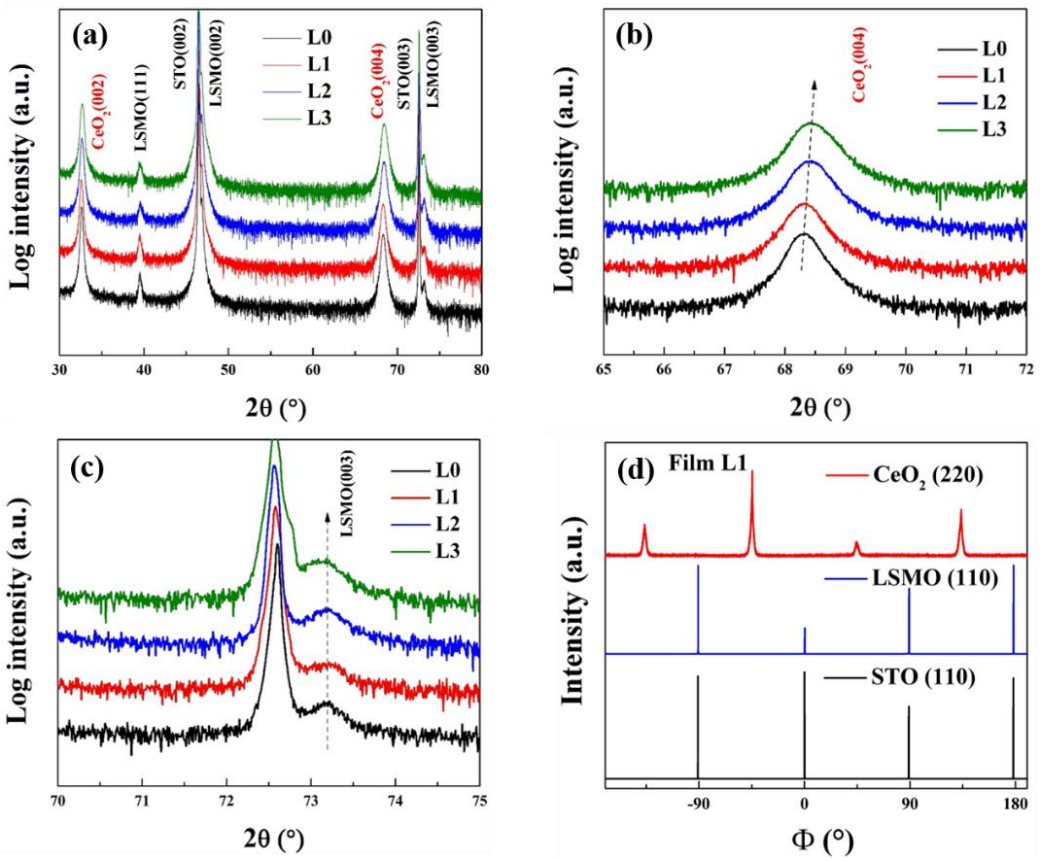

Figure 3.4 (a) 2θ-ω XRD patterns of L0-L3 3D framed thin films, (b) local CeO_2 (004) scans of L0-L3 VAN films, (c) local LSMO (003) scans of L0-L3 VAN films, and (d) ϕ scan patterns of L1 films along (110) direction.

Table 3.5 Out-of-plane d-spacing Variation of 3D Framed Films L0-L3 With Different LSMO Interlayers

Sample name	**CeO_2 (004)**	**Error**	**LSMO (003)**	**Error**
L0	1.37188	5.75E-4	1.29252	1.88746E-4
L1	1.37090	3.80789E-4	1.29135	2.75379E-4
L2	1.36975	3.22749E-4	1.29170	7.07107E-5
L3	1.36853	4.97284E-4	1.29185	3.88909E-4

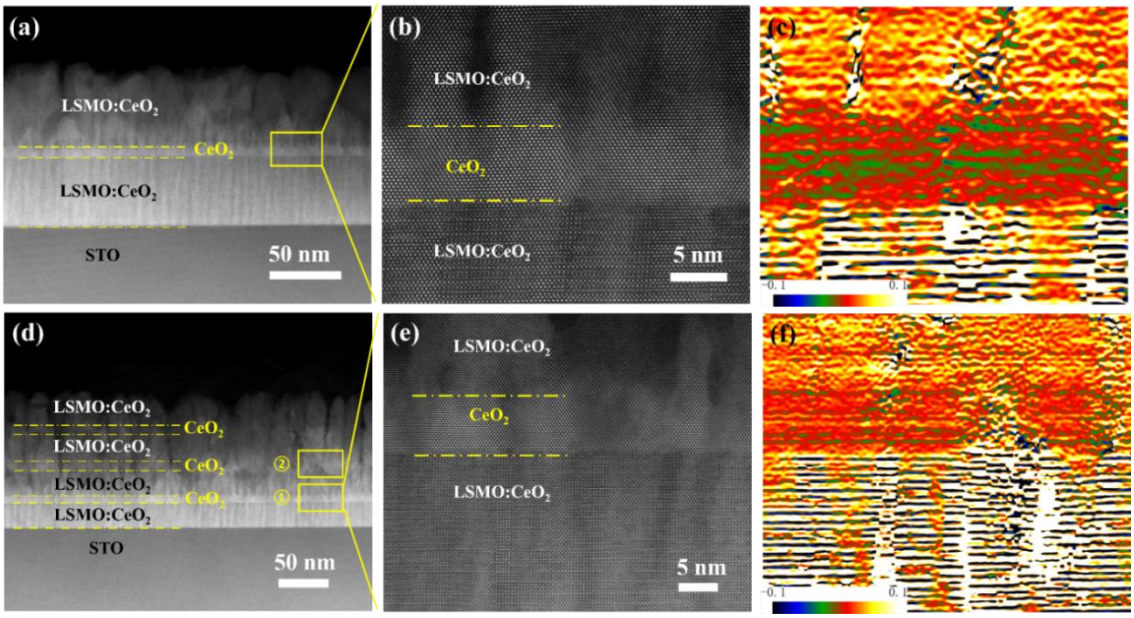

Figure 3.5 (a) Cross-sectional STEM image of the 3D CeO_2 framed thin film C1, (b) its HRSTEM image at the lateral CeO_2 interlayer area (marked by a yellow rectangular in (a)), and (c) the corresponding GPA ε_{yy} (out-of-plane strain) map of the image shown in (b). (d) Cross-sectional STEM image of the 3D CeO_2 framed thin film C3, (e) its HRSTEM image at the first lateral CeO_2 interlayer area from bottom (marked by the yellow rectangular as 1), and (f) the corresponding GPA ε_{yy} (out-of-plane strain) map of the image shown in (e). Here the lateral CeO_2 interlayer area is selected as the reference in each GPA ε_{yy} map of (c) and (f), and thus exhibits a red-green color. The CeO_2 vertical nanopillars within VAN layers are shown in a bright yellow color, illustrating larger out-of-plane d-spacing in those vertical CeO_2 nanopillars compared to its reference of the lateral CeO_2 interlayer area.

Figure 3.5 (a) and (b) exhibit STEM images of sample C1 under high-angle-annular-dark-field (HAADF) mode in low and high resolution, respectively. Consistent with the previous TEM results, the STEM images confirm 3D interconnected CeO_2 skeletons embedded in films. High resolution STEM images (Figure 3.5 (b)) show a very clear interface between CeO_2 and LSMO with high epitaxial quality. A similar structure is observed at the first lateral CeO_2 interlayer of sample C3 (Figure 3.5 (d) and (e)). However, as the number of interlayers increases, larger surface roughness is seen. To clearly resolve the 3D strain state in the samples, geometric phase analysis (GPA) was conducted using the high resolution STEM images (Figure 3.5 (b) and (e)), and

presented as vertical strain (ε_{yy}) maps in Figure 3.5 (c) and (f), respectively. Here the lateral CeO_2 interlayer area is selected as a reference for this GPA mapping and is shown by a red-green color. The bright yellow color contrast of CeO_2 in the VAN part suggests that the vertical CeO_2 nanopillars have a larger out-of-plane d-spacing, i.e. a tensile strain out-of-plane compared to the lateral CeO_2 layer, which is consistent with our observation of the two split peaks in the XRD data (Figure 3.3). A sharp change of ε_{yy} can be clearly seen across the lateral CeO_2 and VAN layers, indicating that the *c*-lattice parameter of CeO_2 varies abruptly in those layers. It is consistent with its filtered image (Figure 3.6), in which the CeO_2 interlayer shows a smaller out-of-plane d-spacing and CeO_2 in the VAN part presents a larger tensile strain out-of-plane. These observations confirm our initial 3D strain design where highly strained LSMO can be achieved using a 3D CeO_2 framework. Such strain could potentially lead to the variation of the length and angle of Mn^{3+}-O-Mn^{4+} bonds, which has been previously reported.[106, 125, 126]

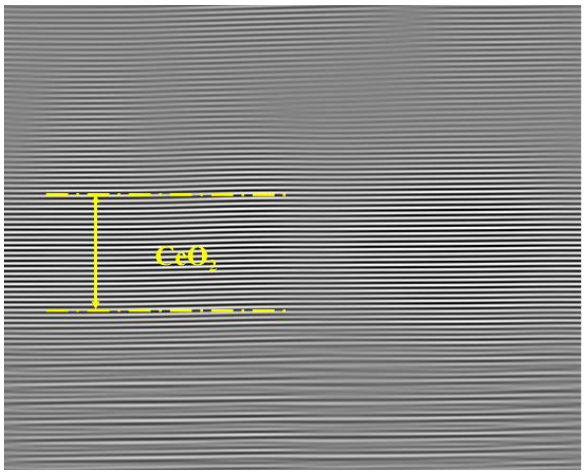

Figure 3.6 The fast-Fourier filtered image of Figure 3.5 (b).

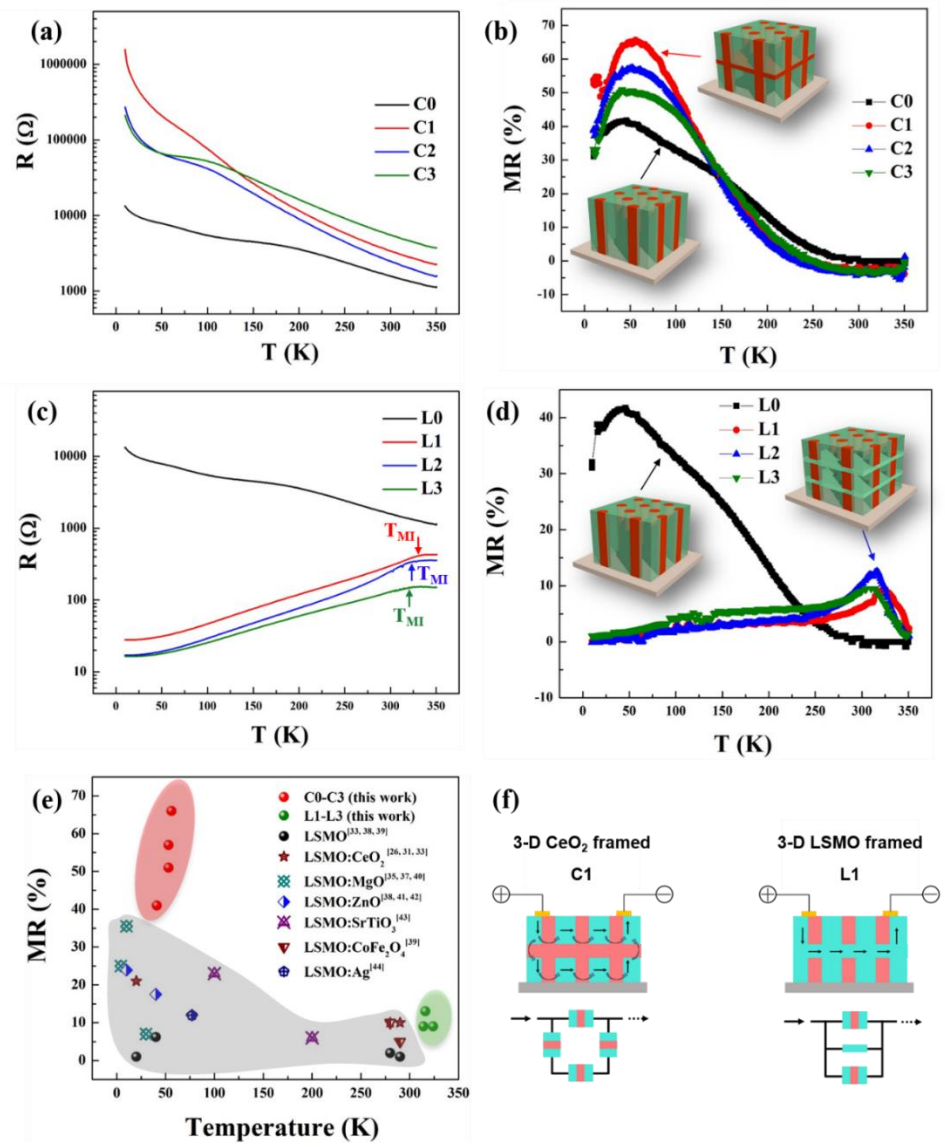

Figure 3.7 (a) R-T plots of 3D CeO_2 framed nanocomposite thin films C0-C3. (b) The temperature dependence of MR for the nanocomposite thin films C0-C3. (c) R-T plots of 3D LSMO framed nanocomposite thin films L0-L3. The arrows point out the metal-to-insulator transition temperature T_{MI} of L1-L3. (d) The temperature dependence of MR for the nanocomposite thin films L0-L3 with the metal-to-insulator transition temperature T_{MI} marked for samples L1-L3. (e) Summary of the maximum LFMR values of LSMO-based composite thin films recently reported and their corresponding peak temperature.[26, 31, 33, 35, 37-44] All the LFMR values listed here are measured under the same magnetic field of 1 T applied out-of-plane (perpendicular to the film plane). (f) Schematic illustrations of the circuit models for the 3D CeO_2 framed nanocomposite structure C1 and the 3D LSMO framed nanocomposite film structure L1.

To resolve the transport properties in these 3D framed structures, temperature dependence of resistance (R-T) curves at zero-field are shown in Figure 3.7 (a) for samples C0-C3. Overall, reducing resistance with increasing temperature represents a typical semiconductor behavior in C0-C3, because of the large portion of CeO_2 introduced in the nanocomposites (CeO_2: LSMO ≥ 1:1 in C0-C3). Figure 3.7 (b) plots the temperature dependence of the magnetoresistance (MR %) in the 3D framed nanocomposite films C0-C3, with clearly defined MR peaks located near 50 K. The MR % of films C0-C3 increases at first and then reduces as the temperature increases from low temperature to room temperature. The MR % peak value of the VAN thin film C0 is ~ 40%, which is higher than many other reported LSMO composite films.[31, 121, 123, 127-129] 3D CeO_2 frameworks further enhance the overall MR properties, where the MR peak value increases from 40% (C0) to 51% (C3), 57% (C2) and maximizes at 66% (C1). The enhancement can be explained by the 3D CeO_2 framework as indicated in Figure 3.7 (f). Such 3D CeO_2 framework not only tailors the out-of-plane strain of the LSMO phase, but also builds up the 3D tunneling framework for the electron transport. The synergistic effect between the strain tuning and the tunneling effect in C1-C3 (red dots) highly promotes the MR properties and enables a record high MR % in LSMO nanocomposites (Figure 3.7 (e)).[112, 121, 123, 127, 129-136] The relatively lower MR % in C2 and C3 compared to C1 is possibly related to the surface roughness observed in both samples where the 3D insulating framework might not be effective in the top layers.

The L1-L3 samples with a 3D LSMO framework exhibit metallic behavior in contrast to the C1-C3 samples (Figure 3.7 (c)), as their resistances gradually increase from 10 K to 350 K with a metal-insulator transition temperature T_{MI} at ~325 K. The metallic behavior is associated with the high composition of LSMO in L1-L3 and the 3D interconnected conductive LSMO frames built in the composite films L1-L3. Meanwhile, the resistance of the composite films L1-L3

decreases with inserting more lateral LSMO interlayers over the entire temperature regime. The LSMO interlayers interconnect with the vertical LSMO domains forming a conductive 3D frame in the film. Thus, the tunneling magnetoresistance effect is effectively reduced. But interestingly, such L1-L3 structures enable higher MR values at higher temperatures, e.g. 13% at 316 K in sample L2, which is a dramatic MR value improvement compared to C0-C3 and previous reports at higher temperatures near room temperature.

Based on the above observations, it is clear that magnetic tunneling junctions (MTJ) of LSMO/CeO_2/LSMO and their geometrical arrangement in these composite films are very important for enhancing the LFMR properties. In C1-C3 samples, there are effective vertical and lateral MTJ structures integrated in the system by incorporating CeO_2 interlayers in the VAN system as indicated in Figure 3.7 (f). Such 3D insulating frameworks effectively maximize the 3D magnetic tunneling effect and lead to a record high MR % in LSMO based systems.

Most of the previous nanocompositing efforts focus on single layer VAN structures. For example, changing the dimension and density of MgO, Chen *et al.* altered the strain and magnetic properties of LSMO-MgO VAN systems and tripled the MR value to 40% at 20 K.[107] Similarly, the LFMR value of LSMO-CeO_2 VAN structure was enhanced from 5% to 21% at 20 K by reducing secondary phase domain size from ~7 nm to ~3 nm.[123] Fan *et al.* systematically shifted transition temperature and promoted the LFMR up to ~35% at 20 K by tuning shape and relative ratio of CeO_2 domains in the LSMO-CeO_2 VAN system.[121] This work with a 3D strain framework using both lateral and vertical interlayers structures effectively maximizes the 3D strain state in the systems, manipulates the electron transport paths in these systems, and thus gives even larger tunabilities of the strain-enabled physical properties and the overall electrical transport phenomena.

3.5 Conclusion

The 3D framework thin films of LSMO-CeO_2 epitaxial VANs interlayered with either CeO_2 or LSMO are designed and processed to effectively control the strain state of the films as well as the electron transport phenomena. This 3D strained framework structures combine both lateral strain by layered structures and vertical strain in VAN and thus maximize the overall strain in the films. Under synergistic effects of 3D maximized strain tuning and integrated vertical and lateral magnetic tunnel junction structures, 3D CeO_2 interlayered samples show a record high MR % of 51%-66%, while 3D LSMO interlayered thin films boost the MR % peak in the relatively higher temperature regime (near room temperature). This 3D strain framework concept opens up a new avenue to maximize the film strain beyond the initial critical thickness and can be applied to many other material systems with strain-enabled functionalities beyond magnetrotransport properties.

CHAPTER 4. STRAIN AND PROPERTY TUNING OF THE 3D FRAMED EPITAXIAL NANOCOMPOSITE THIN FILMS VIA INTERLAYER THICKNESS VARIATION

(This chapter is reprinted with permission from "*Strain and property tuning of the 3D framed epitaxial nanocomposite thin films via interlayer thickness variation*" by X. Sun, et al., Journal of Applied Physics, 125, 082530 (2019).)

4.1 Overview

This work demonstrates the growth of three-dimensional (3D) ZnO-framed $La_{0.7}Sr_{0.3}MnO_3$ (LSMO)-ZnO heteroepitaxial thin films in a vertically aligned nanocomposite (VAN) form on $SrTiO_3$ (STO) substrates. Such 3D framed structures are formed by interlayering pure ZnO layers in LSMO-ZnO vertically aligned nanocomposite (VAN) thin films to thus achieve a ZnO-framed nanocomposite structure. Tailoring the thickness of the ZnO interlayer enables fine-tuning of the overall strain state of the two phases, and thus leads to the tuning of the physical properties, such as the metal-insulator transition temperature, and magnetotransport properties. The optimum thickness of the ZnO interlayer is determined to be ~2 nm to obtain a maximum magnetoresistance of 31% by a combined strain tuning and magnetoresistance tunneling effect. This work demonstrates effective strain tuning using the 3D framed design and provides a comprehensive perspective on the strain- and property- tuning using 3D nanocomposite frameworks

4.2 Introduction

With a broad spectrum of structures and functionalities, complex oxide thin films have been under intense research focus for decades. In particular, perovskite oxide (ABO_3) thin films

have very wide interest, owing to their controllable crystal structures, outstanding physical properties, and promising applications in many modern electronic devices.[3, 8, 31, 63, 68, 108, 137] More interestingly, the properties of the perovskite oxides are sensitive to structural changes. For example, adjusting the crystal structure of ABO_3, via changing the B-O-B bonds length and angles, can efficiently tune the electronic bandgaps, conductivity, transition temperature, magnetoresistance and other physical properties of the perovskite oxides.[8, 12, 138] Strain tuning is considered as one of the most effective approaches to manipulate the crystal lattices and optimize the properties. In most cases, the focus has been on tuning the in-plane strain in ABO_3-based thin films by growing them epitaxially onto the substrates with large lattice mismatch, such as $SrTiO_3$, $LaAlO_3$, and Al_2O_3.[8, 40, 48, 68, 79, 139] Thereafter, a multilayered heterostructure is created to continuously adjust the in-plane strain and strengthen it over a large scale by stacking the ABO_3 layers with a secondary phase in a layer-by-layer fashion.[57, 64, 140-142]

However, tuning in-plane strain using epitaxial growth is largely constrained by the substrate choices and the critical film thickness (typically, a few 10s of nanometers). Much of the strain will relax through the formation of misfit dislocations as the film thickness increases.[61, 138, 143] Two-phase heteroepitaxial nanocomposite thin films in the vertically aligned nanocomposite (VAN) thin film form presents a novel approach for coupling the out-of-plane strains between the two phases.[18, 61, 79, 115, 143-145] The VAN microstructures can thus achieve continuous strain through the film thickness, and thus lead to novel or enhanced properties.[61, 64, 68, 144, 146] For example, the $(La_{0.7}Ca_{0.3}MnO_3)_{1-x}$:$(MgO)_x$ epitaxial nanocomposite thin films have achieved fine-tuning of the structure leading to strongly enhanced magnetotransport properties of $La_{0.7}Ca_{0.3}MnO_3$ through vertical strain control by the stiffer MgO phase.[147] Also, VAN $(La_{0.7}Sr_{0.3}MnO_3)_{1-x}$:$(CeO_2)_x$ thin films have not only improved low-field

magnetoresistance (LFMR) from ~13.5% to ~34.3% by adjusting the relative ratio x, but they also have new functionalities which do not normally exist in single-phase epitaxial thin films.[50, 77] The observed giant enhancements in LFMR is not only due to the tensile strain imparted on the $La_{0.7}Sr_{0.3}MnO_3$ (LSMO) vertically, but is also due to the introduction of insulating secondary phases such as MgO and CeO_2.[57, 138, 148] Those secondary phases create many vertical insulating nanopillars as barriers well dispersed in the LSMO matrix and they successfully lead to magnetic tunneling in-plane to further boost the magnetoresistance (MR) of the thin films. Recently a three-dimensional (3D) framed LSMO-CeO_2 nanocomposite thin film structure was made by inserting lateral interlayers into VAN structures.[138] Combining the VAN and multilayered structures together, this novel 3D framed structure takes the advantages of both lateral and vertical strain, creating magnetic tunneling effects both in-plane and out-of-plane, given superior magnetotransport performance, with LFMR values as high as 66% at 56 K (under the magnetic field of 1 T).[138]

To explore the flexibility of 3D framed nanocomposite designs and to study the thickness dependent of the lateral interlayer on the overall strain and the properties of the thin films, we applied the 3D framed design to another classic nanocomposite system LSMO-ZnO and constructed a 3D ZnO frame structure with a ZnO lateral layer. In addition, to being a well-known wide-bandgap semiconductor, ZnO effectively tunes the strain of LSMO through lattice coupling and serves as an insulating tunneling barrier in LSMO for enhanced magnetotransport performance.[31, 116, 117, 149-151] As illustrated in Figure 4.1, the thickness of the ZnO lateral layer is varied while the LSMO-ZnO composition is maintained at 3:7 (L3Z7). As the average thickness of the ZnO lateral interlayer is varied from ~1, 2, 5, to 10 nm, the corresponding L3Z7-based samples are named as Z1, Z2, Z5, and Z10. In addition, the thickness effect on strain is also

explored in the L5Z5 (molar ratio of LSMO/ZnO = 5:5)-based system, with samples named as Z1', Z2', Z5', Z10' accordingly. The single layer L3Z7 and L5Z5 VAN thin films are named Z0 and Z0' respectively. Detailed microstructure studies including XRD, TEM and STEM were conducted to reveal the 3D framed structures, strain states and the defects at the interfaces. The microstructural characteristics are correlated with the LFMR properties to reveal the interlayer effects on strain tuning and the overall transport properties.

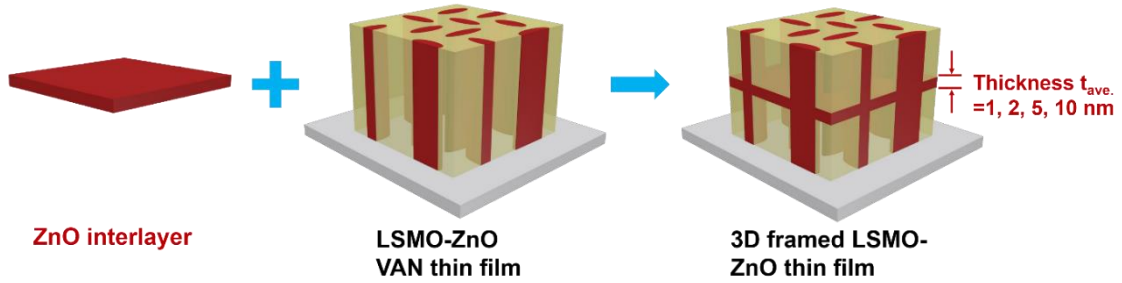

Figure 4.1 Schematic diagram of assembling the three-dimensional (3D) framed heteroepitaxial $La_{0.7}Sr_{0.3}MnO_3$ (LSMO)-ZnO nanocomposite thin film by inserting one pure ZnO lateral interlayer into the LSMO-ZnO vertically aligned nanocomposite (VAN) thin film. The impact of this lateral ZnO interlayer is systematically investigated by gradually increasing its average thickness from 0 to ~10 nm.

4.3 Experimental

4.3.1 Sample preparation

The 3D-framed LSMO-ZnO nanocomposite thin films Z0-Z10 were grown on single crystalline $SrTiO_3$ (STO) (001) substrates via a pulsed laser deposition (PLD) approach. The L3Z7 and L5Z5 composite targets were prepared by a conventional solid-state sintering process: high-purity La_2O_3, $SrCO_3$, MnO_2, and ZnO powders were sufficiently mixed and ground according to the stoichiometric ratio of 3:7 and 5:5 between LSMO and ZnO, respectively. The mixtures were pressed into disks and sintered at 1100 ºC in air for 12 h. The pure ZnO target was prepared through a similar procedure. The deposition was accomplished at 750 ºC under the oxygen partial pressure

of 0.2 Torr (1 Torr=133.3 Pa). All the samples Z0-Z10 were named according to the average thickness t_{ave} of their lateral ZnO interlayer, varying from 0 to 10 nm. For example, the VAN thin film Z0 is classified as a L3Z7-based 3D framed thin film with 0 deposition pulses from the ZnO target. Similarly, L5Z5-based 3D framed thin films Z0'-Z10' were obtained by inserting one ZnO interlayer of 0-10 nm thick into the L5Z5 VAN thin films.

4.3.2 Characterization

The crystal structures, lattice coupling, and d-spacing of the thin films Z0-Z10 were characterized with a PANalytical Empyrean x-ray diffraction (XRD) system through θ-2θ and Φ scans. Transmission electron microscopy (TEM), scanning TEM, selected area electron diffraction (SAED) patterns, and energy-dispersive x-ray spectra (EDS) mapping of the thin films Z0-Z10 were obtained on a FEI TALOS F200X instrument at 200 kV equipped with ultrahigh resolution high angle annular dark field detectors and Supper-X^{TM} electron-dispersive X-ray spectroscopy. Magnetotransport results were collected on the Physical Properties Measurement System (PPMS, Quantum Design Dynacool) with an applied out-of-plane (OP) magnetic field and an in-plane (IP) current. Magnetoresistance (MR) values were calculated by the following equation:

$$\mathrm{MR}(\%) = \frac{\rho_0 - \rho_H}{\rho_0} \times 100\% \quad (4\text{-}1)$$

where ρ_H and ρ_0 is the electrical resistivity with and without applied magnetic field of 1 T at the same temperature.

4.4 Results and discussion

4.4.1 Strain evolution

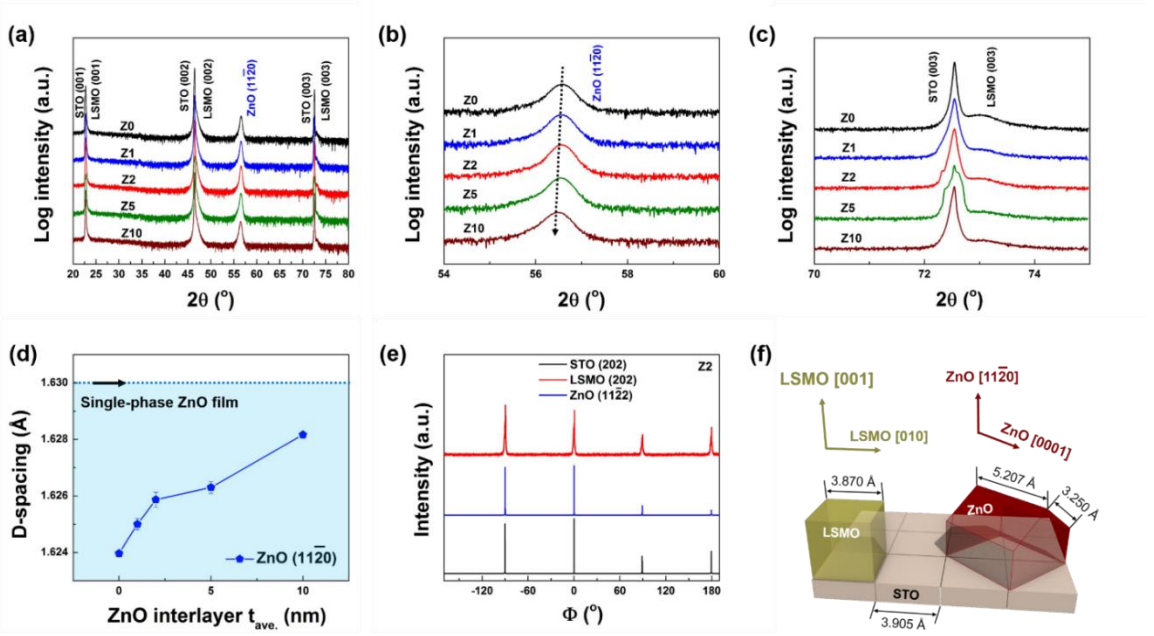

Figure 4.2 (a) XRD *θ-2θ* patterns of the as-prepared L3Z7 (the molar ratio of LSMO/ZnO = 3:7)-based 3D framed nanocomposite thin films Z0-Z10 grown on $SrTiO_3$ (STO) (001). Detailed XRD *θ-2θ* scans of those nanocomposite thin films Z0-Z10 in the range of (b) ZnO (11$\bar{2}$0) and (c) LSMO (003) peaks. (d) Systematic tuning of the ZnO lateral interlayer on the d-spacing of ZnO (11$\bar{2}$0) by increasing the average thickness ($t_{ave.}$) of ZnO lateral interlayer from 0 nm to ~10 nm (from Z0 to Z10). The d-spacing values and error bars are based on Table 4.1. (e) *Φ* scans of STO (202), LSMO (202), and ZnO (11$\bar{2}$2) for the thin film Z2. (f) In-plane lattice matching relations between LSMO, ZnO, and STO.

X-ray diffraction (XRD) is utilized to determine the phases, growth patterns, and the evolution of d-spacing in all the L3Z7-based 3D-framed nanocomposite thin films. The XRD *θ-2θ* patterns in Figure 4.2 (a) reveal that all the nanocomposite thin films Z0-Z10 grew highly textured with high crystallinity on the single-crystalline $SrTiO_3$ (STO) (001) substrates. LSMO grows along the [001] direction and ZnO is textured along the [11$\bar{2}$0] direction. No impurity peaks are observed in the full *θ-2θ* scans. In the detailed *θ-2θ* scans of Figure 4.2 (b), the ZnO (11$\bar{2}$0)

peak gradually shifts to lower angles with increasing the thickness of the lateral ZnO interlayer from 0 to ~10 nm for samples of Z0-Z10, i.e., a larger d-spacing of ZnO (11$\bar{2}$0) is obtained from Z0 to Z10, as the thickness of the lateral ZnO interlayer increases. Meanwhile, all the d-spacing values are calculated based on the Bragg's equation and the multiple θ-2θ scans results. The results are plotted in Figure 4.2 (d). It confirms the increase of the $d_{ZnO\ (11\bar{2}0)}$-spacing as the ZnO lateral interlayer thickness increases. According to Table 4.1, the average $d_{ZnO(11\bar{2}0)}$-spacing value of the L3Z7 VAN thin film Z0 (no lateral interlayer) is ~ 1.6240 Å and the strain is -0.4312% compared with the single-phase ZnO film grown on STO ("-" represents compression, "+" represents tension, both out-of-plane). After introducing the lateral ZnO interlayer in sample Z1-Z10, the $d_{ZnO\ (11\bar{2}0)}$-spacing value steadily increased from ~1.6250 Å (Z1) to ~1.6282 Å (Z10), corresponding to a reduced compressive strain from -0.3679% to -0.1737% out-of-plane. Due to the low percentage of LSMO in this case, the LSMO peaks are not obvious in the L3Z7-based composite system. The Φ scans in Figure 4.2 (e) illustrate that the orientation relationship between the film and the STO substrate as LSMO(001) || STO(001) || ZnO(11$\bar{2}$0). LSMO is epitaxially grown on the STO substrate in a cube-on-cube fashion with no in-plane rotation. In contrast, the ZnO hexagonal unit cell lies down on the top of STO with ZnO [0001] direction in-plane as illustrated in Figure 4.2 (f).

Table 4.1 Thickness Effect of Lateral ZnO Interlayer on The d-spacing And Strain of ZnO $(11\bar{2}0)$ in The L3Z7-based Nanocomposite Thin Films Comparing with The Pure ZnO Film Grown on STO

Sample Name	**$d_{ZnO(11\bar{2}0)}$-spacing / (Å)**	**Error**	**Strain on ZnO $(11\bar{2}0)$ / (%)**
Pure ZnO Film Grown on STO	1.6310	4.0000E-4	0
Z0	1.6240	6.6667E-5	-0.4312
Z1	1.6250	2.0000E-4	-0.3679
Z2	1.6259	2.6667E-4	-0.3147
Z5	1.6263	2.08167E-4	-0.2882
Z10	1.6282	6.66667E-5	-0.1737

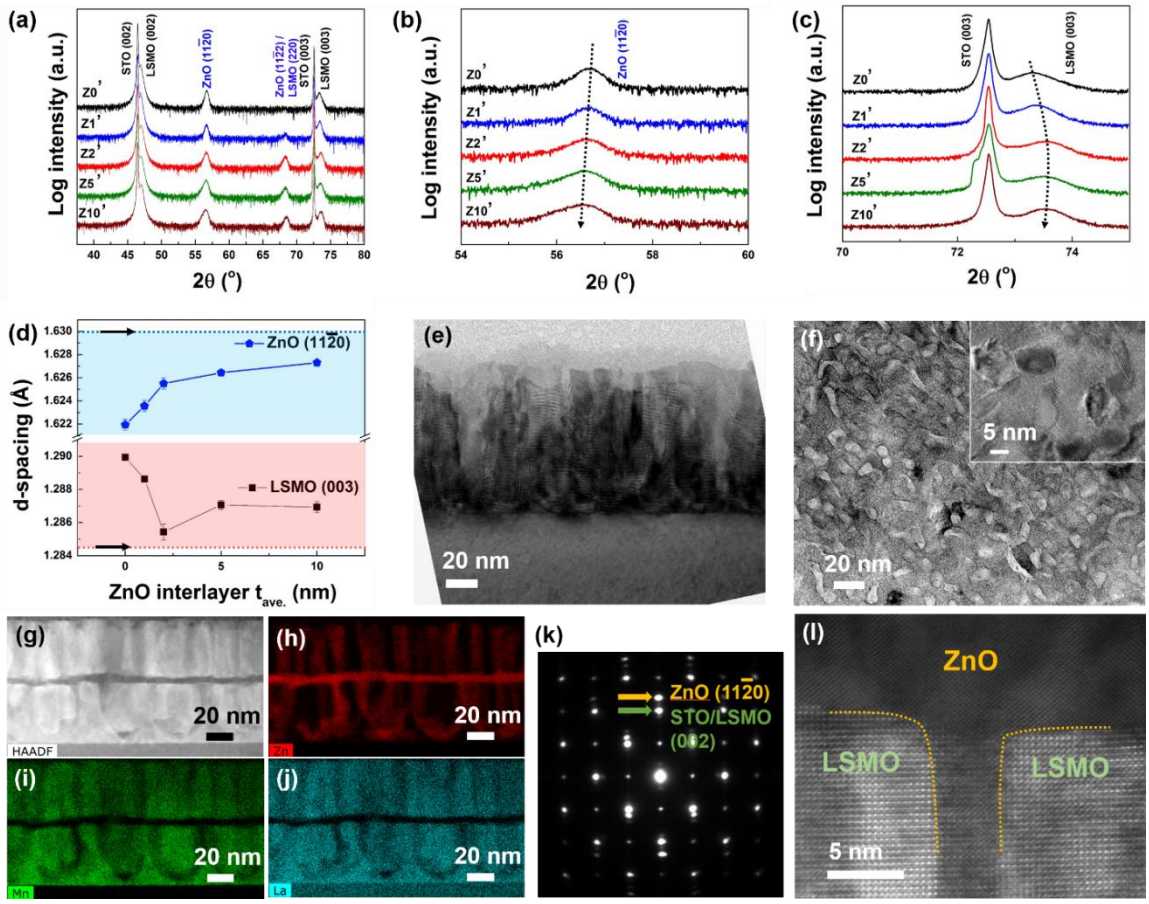

Figure 4.3 (a) XRD *θ-2θ* patterns of the as-prepared L5Z5 (the molar ratio of LSMO/ZnO = 5:5)-based 3D framed nanocomposite thin films Z0'-Z10' grown on $SrTiO_3$ (STO) (001). Detailed XRD *θ-2θ* scans of those nanocomposite thin films Z0'-Z10' in the range of (b) ZnO (11$\bar{2}$0) and (c) LSMO (003) peaks. (d) Systematic tuning of the ZnO lateral interlayer on the d-spacing of ZnO (11$\bar{2}$0) and LSMO (003) by increasing the average thickness ($t_{ave.}$) of ZnO lateral interlayer from 0 nm to ~10 nm (from Z0' to Z10'). The d-spacing values and error bars are based on Table 4.2. The blue dash line on the top marks the $d_{ZnO(11\bar{2}0)}$-spacing of the single-phase ZnO thin film grown on STO, and the red dash line on the bottom reveals the $d_{LSMO(003)}$-spacing of the single-phase LSMO film grown on STO. (e) Cross-sectional and (f) plan view TEM images of the L5Z5 VAN thin film Z0' with a plan view HRTEM image as the inset of (f). Cross-sectional (g) STEM image, (h-j) energy-dispersive x-ray spectra (EDS) mapping, and (k) selected-area electron diffraction (SAED) pattern of the L5Z5-based 3D framed thin film Z5'. (i) Cross-sectional high-resolution TEM (HRTEM) image of the sample Z5' showing clear interface between ZnO and LSMO on lateral and vertical directions without apparent inter-mixing between phases.

Table 4.2 Thickness Effect of Lateral ZnO Interlayer on The d-spacing And Strain of ZnO ($11\bar{2}0$) And LSMO (003) in The L5Z5-based Nanocomposite Thin Films Comparing with The Pure ZnO And LSMO Films Grown on STO

Sample Name	**$d_{ZnO(11\bar{2}0)}$-spacing / (Å)**	**Error**	**Strain on ZnO ($11\bar{2}0$) / (%)**	**$d_{LSMO(003)}$-spacing / (Å)**	**Error**	**Strain on LSMO (003) / (%)**
Pure ZnO Film Grown on STO	1.6310	4.0000E-4	0			
Pure LSMO Film Grown on STO				1.2846	5.7735E-5	0
Z0'	1.6219	2.9059E-4	-0.5559	1.2899	6.6667E-5	0.4152
Z1'	1.6236	4.6667E-4	-0.4558	1.2886	1.6667E-4	0.3140
Z2'	1.6255	5.0000E-4	-0.3372	1.2854	4.8074E-4	0.0649
Z5'	1.6264	1.2019E-4	-0.2800	1.2871	2.7284E-4	0.1920
Z10'	1.6273	2.0000E-4	-0.2269	1.2869	3.3333E-4	0.1816

To effectively reveal the strain tuning in LSMO in the 3D ZnO framed nanostructures, we compare the results to LSMO-ZnO composites having a LSMO:ZnO 50:50 (L5Z5) ratio. Similar to the L3Z7-based system, the L5Z5-based 3D framed thin films, Z0'-Z10', are also grown highly textured on the single-crystalline STO substrates as evidenced in Figure 4.3 (a). The minor peak at ~68º in Z1'-Z10' could be attributed to ZnO ($11\bar{2}2$) or LSMO (220). The peak shift of ZnO

(11$\bar{2}$0) to lower angles (Figure 4.3 (b)) corresponds to the gradually enhanced $d_{ZnO(11\bar{2}0)}$-spacing values from 1.6219 Å to 1.6273 Å, caused by increasing the thickness of the lateral ZnO interlayer from Z0' to Z10'(Figure 4.3 (c)). These observations are consistent with the L3Z7-based system in Figure 4.2 (b) and d. In this system, LSMO (003) peaks are clearly observed in Z0'-Z10' (Figure 4.3 (c)). The LSMO (003) peak mainly shifts to higher angles from Z0' to Z10', revealing the trend of the reduced $d_{LSMO(003)}$-spacings with increasing interlayer thickness, as shown in Figure 4.3 (d). After comparing with the respective single-phase films grown on STO (blue dashed line-pure ZnO film, red dashed line-pure LSMO film), it is easily noted that the ZnO phase is compressively strained out-of-plane and that the LSMO in Z0'-Z10' is in tension out-of-plane. The strain states are both simultaneously relieved slowly with the increasing interlayer thickness. Besides, the cross-sectional (Figure 4.3 (e)) and plan-view (Figure 4.3 (f)) TEM images of Z0' show that the ZnO nanopillars are vertically aligned and uniformly distributed in the LSMO matrix with clear interfaces. The cross-sectional STEM and the EDS mapping of Z5' (Figure 4.3 (g)-(j)) confirm the 3D ZnO framed structure with a lateral ZnO interlayer of ~5 nm. The distinct dots in the selected-area electron diffraction (SAED) pattern (Figure 4.3 (k)) demonstrates the high epitaxial quality of Z5' grown on STO substrates. The cross-sectional high-resolution TEM (HRTEM) image of Figure 4.3 (i) exhibits the intersection part of a ZnO vertical nanopillar connecting to its lateral interlayer with sharp vertical and lateral LSMO-CeO_2 interfaces. To demonstrate the d-spacing variation of LSMO, the L5Z5 system with a higher LSMO content compared to the L3Z7 system has been included in this interlayer study. More systematic studies are still conducted in L3Z7 system and presented in the following sections.

4.4.2 Microstructural and chemical composition characterizations

In the cross-sectional TEM image of the L3Z7-based thin film Z0 (Figure 4.4 (a)), all the ZnO nanopillars of ~100 nm height are vertically aligned and embedded in the LSMO matrix. Its SAED pattern demonstrates the high epitaxial quality of the nanocomposite Z0 film and the epitaxial relation of LSMO (001) || ZnO ($11\bar{2}0$) || STO (001). The STEM, EDS mapping and HRTEM images (Figure 4.4 (b)-(d)) clearly reveal the ZnO vertical nanopillars are evenly distributed through the entire film thickness and that the LSMO-ZnO interfaces are sharp without any apparent interphase mixing. The EDS results show that the atomic ratio between element Mn and ZnO is ~3.03:7, very close to the target ratio of 3:7. In the plan view STEM image and EDS mapping of Z0 (Figure 4.4 (e) and (f)), the high amount of ZnO leads to rectangular ZnO nanodomains which are linked to form a nanomaze-like structure implemented within the LSMO matrix. These nanomaze-like ZnO scaffolds can serve as an efficient insulating barrier in-plane for the conducting LSMO matrix, and thus are responsible for the enhanced LFMR properties to be discussed later.

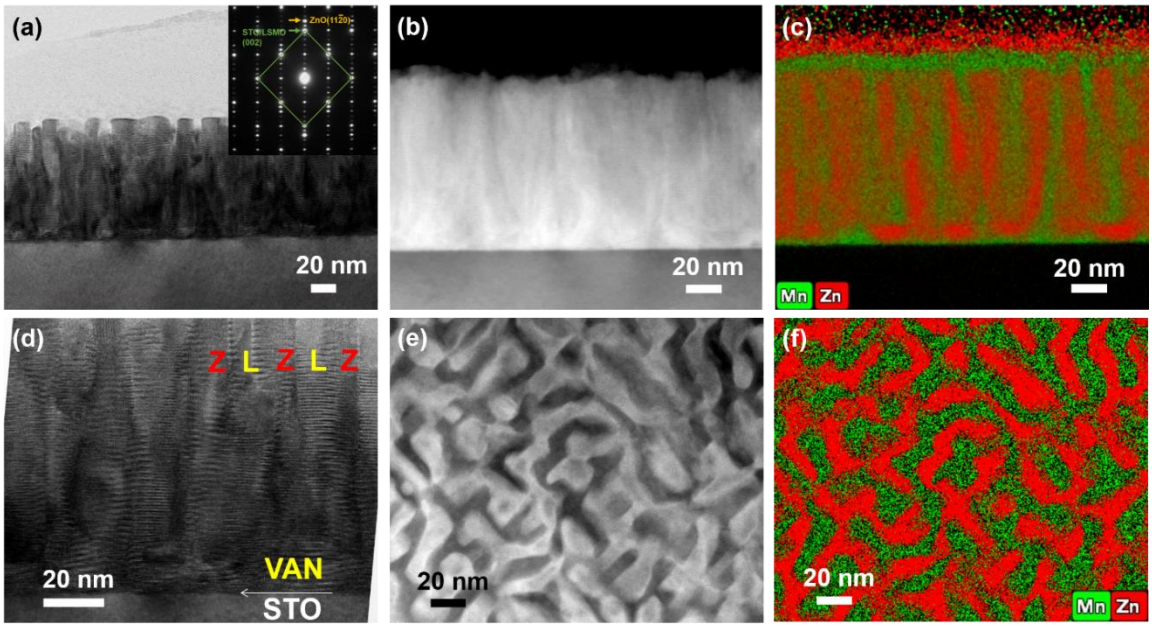

Figure 4.4 (a) Cross-sectional TEM image of the L3Z7-based VAN thin film Z0 with its SAED pattern as the inset. Cross-sectional (b) STEM image, (c) EDS mapping, and (d) HRTEM of the sample Z0. Plan view (e) STEM image and (f) EDS mapping of the sample Z0 in which the large amount of ZnO forms a maze-like ZnO scaffold embedded in the LSMO matrix with sharp LSMO-ZnO interface and no obvious interphase-diffusion.

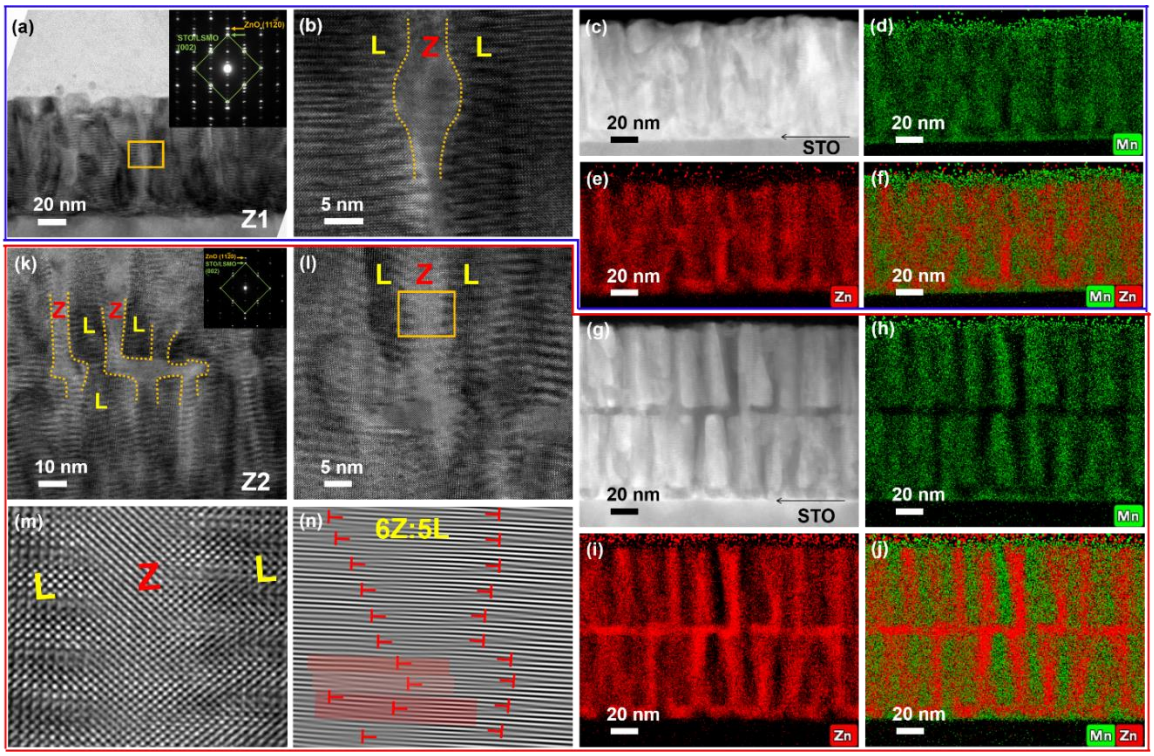

Figure 4.5 Cross-sectional (a) TEM, (b) HRTEM, and (c) STEM images of the L3Z7-based 3D framed thin film Z1 with its SAED pattern as the inset of (a). The average thickness of the ZnO lateral interlayer is ~1 nm in sample Z1. The HRTEM image of (b) corresponds to the rectangular area marked by orange-colored frame in (a). (d-f) Cross-sectional EDS mapping of the sample Z1. Cross-sectional (g) STEM image and (h-j) EDS mapping of the L3Z7-based 3D framed thin film Z2 with a lateral ZnO interlayer of ~ 2 nm thick. Cross-sectional (k) TEM and (l) HRTEM images of the sample Z2 with the corresponding SAED pattern as the inset of (k). (m) Atomic-scale HRTEM image corresponding to the rectangular area marked by orange frame in (l) and (n) its fast-Fourier filtered image, showing the lattice matching relations between ZnO and LSMO out-of-plane. The major coupling pattern is 6-5 matching between ZnO ($11\bar{2}0$) and LSMO (002) along vertical interfaces (6Z:5L) and some minor patterns are 4Z:3L, 5Z:4L, and 7Z:5L marked by red rectangles in (n).

The cross-sectional TEM image in Figure 4.5 (a) shows that the ZnO nanopillars are vertically aligned and embedded in the LSMO matrix of thin films Z1, but without an obvious continuous ZnO lateral interlayer. The SAED pattern still shows high epitaxial growth quality and the same lattice coupling relations between LSMO, ZnO, and STO. The HRTEM image (Figure 4.5 (b), originating from Figure 4.5 (a), shows a ZnO swelling locating in the middle of the vertical ZnO nanopillar. The STEM image and EDS mapping in Figure 4.5 (c)-(f) show obvious contrast

of the ZnO nanopillars which could work as barriers for LSMO out-of-plane but have not connected into a continuous lateral ZnO interlayer yet. The average thickness of the ZnO interlayer is estimated to be ~1nm. Because there is more ZnO in Z2, the ZnO islands are elongated in-plane and some of them are connected together to form ZnO lateral disks (Figure 4.5 (k)). The average thickness can be estimated to be ~2 nm. Excellent epitaxial growth and the same lattice matching relations are still shown by the SAED patterns. The HRTEM image of Z2 (Figure 4.5 (l)) confirms the elongated ZnO disks with a larger barrier effect for the LSMO out-of-plane. It is evident in Figure 4.5 (g)-(j) that some ZnO disks also connect with the vertical ZnO nanopillars to establish a partial 3D frame in the LSMO matrix with sharp LSMO-ZnO interfaces. Besides, the atomic-scale HRTEM image (Figure 4.5 (m)) and its faster-Fourier filtered image (Figure 4.5 (n)) reveal that the main lattice coupling relationship is 6 unit cells of $(11\bar{2}0)$ ZnO match with 5 of (002) LSMO (6Z:5L) along the vertical LSMO-ZnO interface, causing ZnO to be in a compressive strain state out-of-plane. Some minor coupling relations of 4Z:3L, 5Z:4L, and 7Z:5L are also observed and marked as red rectangles (Figure 4.5 (n)), which can trigger ZnO into a higher compressive state out-of-plane. The details are explained in the supplementary information.

A continuous ZnO lateral interlayer is established in the middle of Z5 and creates a full 3D interconnected ZnO frame embedded in the LSMO matrix by attaching to the ZnO vertical nanopillars in the VAN layers (Figure 4.6 (a)). This structure still keeps excellent epitaxial growth and the same lattice matching relations as Z0-Z2 according to the SAED pattern. The average thickness of the lateral interlayer is ~5 nm in the HRTEM image of Figure 4.6 (b). The 3D ZnO framed structure is verified with sharp LSMO-ZnO interfaces vertically and laterally by the STEM image and EDS mapping (Figure 4.6 (c)-(f)). For sample Z10, the ZnO lateral interlayer is estimated to be ~10 nm to ~100 nm thick (Figure 4.6 (g)). The HRTEM, STEM images, and EDS

mapping further confirm that an excellent 3D interconnected ZnO frame structure is maintained in Z10 with all the ZnO vertical nanopillars perfectly aligned (Figure 4.6 (h)-(l)). To evaluate the impact of lateral interlayer thickness on the lattice coupling relations, atomic-scale HRTEM and its filtered images are shown in Figure 4.6 (m) and (n), corresponding to the vertical LSMO-ZnO interface area marked by the orange rectangular frame in Figure 4.6 (h). Along this vertical LSMO-ZnO interface, the main lattice coupling relation is still 6Z:5L, just as for sample Z2 (Figure 4.5 (n)). Besides the 6Z:5L coupling relation, the remaining lattice coupling relation is 7Z:6L which is different from Z2. The coupling of 6Z:5L causes ZnO to be in compression out-of-plane, while 7Z:6L potentially results in ZnO being in a tensile strain state out-of-plane. The potential strains derived from the different lattice coupling patterns are calculated in the supplementary information. The difference in the lattice matching relations between Z2 and Z10 can be used to explain the enlarged $d_{ZnO(11\bar{2}0)}$-spacing from Z2 to Z10 in Figure 4.2 (d). Moreover, it is interesting to note that the initial ZnO nucleation is hard above the STO substrate and thus generates valley-like LSMO-ZnO interfaces in the LSMO-ZnO VAN growth on STO substrate (Figure 4.4). After deposition of the ZnO interlayer (Figure 4.6), the ZnO nucleation is much easier for the top VAN layer and thus grows into vertically pillars without curved interfaces above the ZnO interlayer. It suggests that the strain transition from the ZnO interlayer is different from that from the substrate.

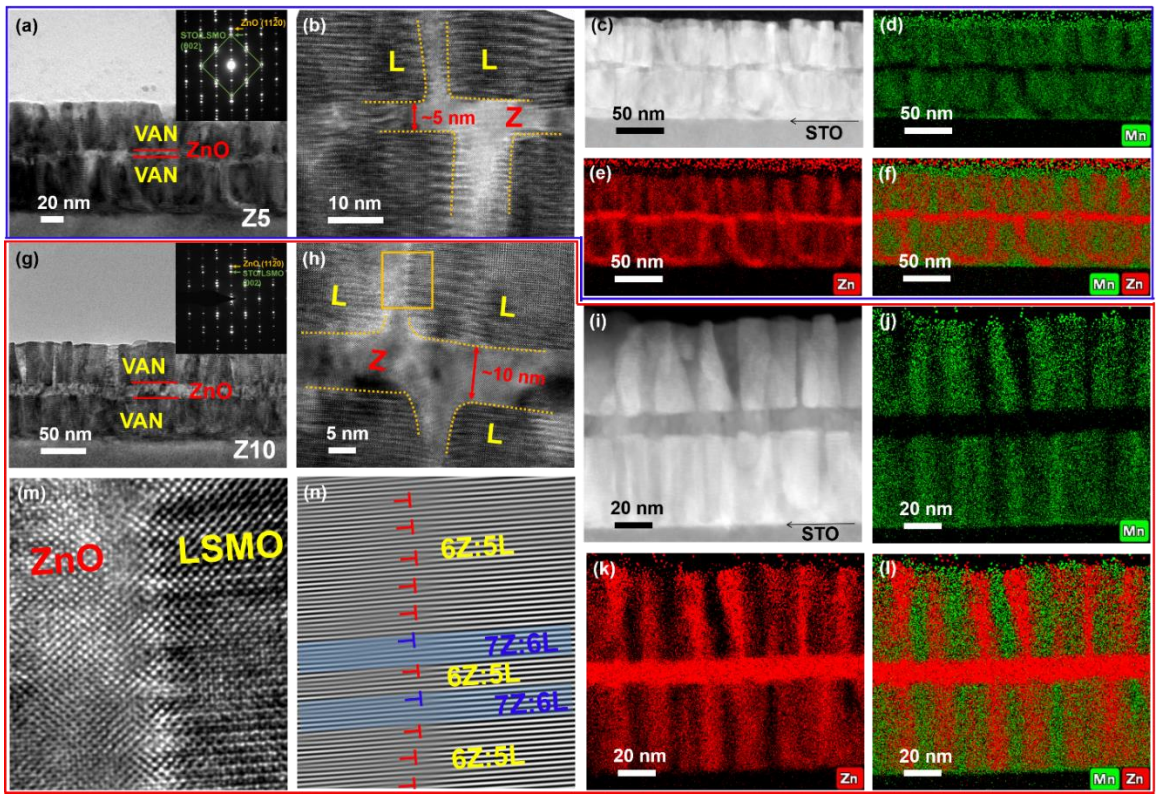

Figure 4.6 Cross-sectional (a) TEM, (b) HRTEM, and (c) STEM images of the L3Z7-based 3D framed thin film Z5 with its SAED pattern as the inset of (a). Sample Z5 has a continuous ZnO lateral interlayer of the average thickness ~5 nm. (d-f) Cross-sectional EDS mapping of the sample Z5 confirming the thickness of Z5 and no apparent inter-mixing between phases. Cross-sectional (g) TEM, (h) HRTEM, and (i) STEM images of the L3Z7-based 3D framed thin film Z10 with a continuous lateral ZnO interlayer of ~ 10 nm thick. The SAED pattern of sample Z10 is in the inset of (g). (j-l) Cross-sectional EDS mapping of the sample Z10 corresponding to (i). (m) Atomic-scale HRTEM image corresponding to the rectangular area marked by the orange frame in (h) and (n) its fast-Fourier filtered image, showing the lattice matching relations between ZnO and LSMO out-of-plane. The major coupling pattern is 6-5 matching between ZnO ($11\bar{2}0$) and LSMO (002) along vertical interfaces (6Z:5L) and the minor pattern of 7Z:6L is marked by blue rectangles in (n).

4.4.3 Tuning of magnetotransport properties

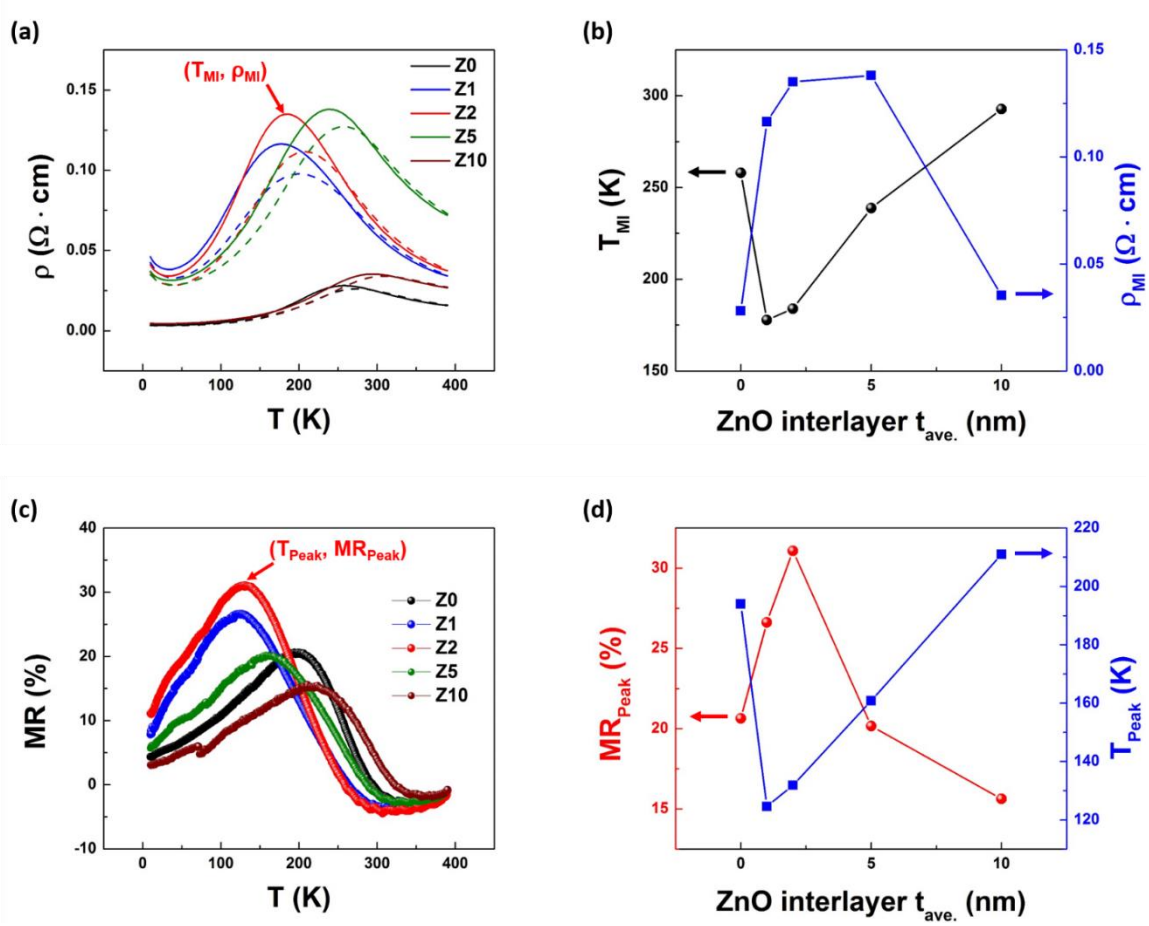

Figure 4.7 (a) Temperature dependence of resistivity (ρ-T) curves for the L3Z7-based 3D framed thin films Z0-Z10 under no magnetic field (in solid line) and a magnetic field of 1 T (in dash line). The metal-insulator transition point of the R-T curve under no magnetic field is recorded as (T_{MI}, ρ_{MI}). (b) Systematic tuning of lateral ZnO interlayer thickness $t_{ave.}$ on the metal-insulator transition temperature T_{MI} and resistivity ρ_{MI} with the thickness $t_{ave.}$ increased from 0 to ~10 nm. (c) Temperature dependence of magnetoresistance (MR-T) curves for the L3Z7-based 3D framed thin films Z0-Z10. The peak of the MR-T curve is recorded as (T_{Peak}, MR_{Peak}). (d) Systematic tuning of lateral ZnO interlayer thickness $t_{ave.}$ on T_{Peak} and MR_{Peak} with the thickness $t_{ave.}$ increased from 0 to ~10 nm.

The transport properties of the L7Z3-based thin films Z0-Z10 are plotted in Figure 4.7. Under no magnetic field, the ρ-T curve of Z0-Z10 initially increases and then decreases from 10 K to 390 K, corresponding to the metallic-insulator transition behavior (Figure 4.7 (a)). The

dependence of the metallic-insulating transition point (T_{MI}, ρ_{MI}) is plotted in Figure 4.7 (b) versus the average thickness $t_{ave.}$ of the ZnO lateral interlayer for each sample. Comparing to the VAN structure of Z0, the transition temperature T_{MI} is largely reduced from ~258 K (Z0) to ~178 K (Z1) once a partial 3D frame structure starts to form in Z1. As the 3D ZnO frame forms in Z1-Z5 and then further strengthens in Z10, the transition temperature T_{MI} keeps increasing to near room temperature (~300 K). Meanwhile, the transition resistivity ρ_{MI} increases from 0.028 Ω·cm (Z0) to ~0.138 Ω·cm (Z5) when the average thickness $t_{ave.}$ increases from 0 nm to ~5 nm. However, after the full 3D ZnO frame is completed in Z5, the transition resistivity ρ_{MI} decreases to ~0.035 Ω·cm (Z10) with a further increase of thickness to ~10 nm. This can be explained by the fact that the thick interlayer of ~10 nm in Z10 can block the current flow out-of-plane, thus only allowing the current to flow in-plane, as is the case for Z0. Moreover, the thin film Z0-Z10 exhibits excellent magnetoresistance (MR) behavior, as shown in Figure 4.7 (c). With the temperature rise from 10 K to 390 K, the MR-T curves of each sample increase at first and then reduce after the peak points (T_{Peak}, MR_{Peak}). Figure 4.7 (d) displays the impact of ZnO interlayer thickness $t_{ave.}$ on the MR peak value (T_{Peak}, MR_{Peak}). With the lateral interlayer thickness increase from 0 nm (Z0) to ~2 nm (Z2), the MR_{Peak} value increases from ~20% (Z0) to ~31% (Z2), which is a 50% enhancement over the VAN structure. After creating continuous lateral interlayers and full 3D ZnO frames, in the films Z5 and Z10, the MR_{Peak} value decreases to ~20% (Z5) and ~15% (Z10). The MR_{Peak} value appears in sample Z2 with a near complete ZnO interlayer. In sample Z5, the thickness of ~5 nm is quite thick for a tunneling effect out-of-plane. In short, a thin ZnO lateral interlayer can provide sufficient barrier effects for magnetoresistance tunneling to give enhanced MR values. However, a full coverage of the lateral ZnO interlayer deteriorates the epitaxial quality of the following VAN

layer. Therefore, the optimal MR_{Peak} value of 31% is achieved in the interlayer sample of ~2 nm through a trade-off between the tunneling effect and epitaxial growth quality.

4.5 Conclusion

Three-dimensional (3D) framework structures were successfully assembled in the $La_{0.7}Sr_{0.3}MnO_3$ (LSMO)-ZnO composite system by inserting one lateral interlayer of ZnO into a LSMO-ZnO vertically aligned nanocomposite thin film. The thickness dependence of this lateral interlayer was explored in terms of the crystal structure, strain, metal-insulator transition temperature, and magnetotransport properties. With thickness increased from 0 to ~10 nm, the tensile strain on ZnO is gradually relieved and so is the compressive strain on LSMO out-of-plane. The lateral interlayer thickness controls the d-spacing and strains on both phases via varying the lattice coupling patterns along the vertical LSMO-ZnO interfaces. Moreover, the ZnO lateral interlayer and vertical nanopillars serve as effective barriers for tunneling which enhance the magnetotransport performance in the 3D ZnO-framed nanostructures. The optimal thickness of the lateral interlayer is ~2nm at which the maximized magnetoresistance of ~31% is achieved above 130 K under the synergistic effect between the strain tuning and the tunneling effect. Because of the hexagonal structure of ZnO, a thicker ZnO lateral interlayer of full coverage degrades the epitaxial quality, and blocks the magnetic tunneling effect. This work demonstrates the flexibility of the 3D framed concept in vertically aligned nanocomposite systems, and provides a promising path for effectie strain tuning and strain-driven property enhancement.

CHAPTER 5. INTERLAYER EFFECT ON MICROSTRUCTURE AND MAGNETOTRANSPORT PROPERTY OF 3D FRAMEWORKS

5.1 Overview

A set of novel three-dimensional (3D) frameworks are assembled through a relatively thin interlayer M sandwiched by two $La_{0.7}Sr_{0.3}MnO_3$ (LSMO)-ZnO vertically aligned nanocomposites (VAN) layers. ZnO nanopillars from the two VAN layers are connected by the interlayer M and create a heterogeneous 3D frame embedded in the LSMO matrix. The impact of the interlayer M is systematically explored on the microstructure and the magnetotransport properties of these 3D frameworks by appropriate selection of the interlayer M within the following candidates—yttria-stabilized zirconia (YSZ), CeO_2, $SrTiO_3$, $BaTiO_3$, and MgO. The strain relaxation on the interlayer causes tilted growth of the ZnO nanopillars from the vertical axis in the top VAN layer. Meanwhile, adjusting the interlayer M increases the metal-insulator transition temperature from ~133 K (M=YSZ) to ~252 K (M=MgO), and also tunes the magnetoresistance peak value from ~36.7% to ~20.8%. The 3D heterogeneous frames empower the films excellent tunable magnetotransport properties and promising potentials in the microstructure-enabled applications.

5.2 Introduction

Strain engineering has been recognized as an efficient approach for tailoring the crystal structure and multifunctionalities of materials, such as electrical, magnetic, optical properties, etc. Since the substrate-clamped single-phase epitaxial films are constrained by the critical film thickness (~ a few tens of nanometers), increasing efforts have been focused on assembling epitaxial nanocomposite films with various microstructures.[62, 138, 146, 152-155] Evolving from

the multilayer configuration to the vertically aligned nanocomposite (VAN), microstructure has been closely correlated with interface-, strain-, and property-engineering in nanocomposite thin films.[52, 61, 64, 115, 143] Although the VAN microstructure has been considered as the-state-of-art, a three-dimensional (3D) framework design is drawing great research interest recently. The 3D framework is generated by combining the multilayer and VAN designs together—numerous vertical nanopillars connect with the lateral interlayers to form a 3D interconnected frame embedded in the matrix phase. This 3D framework design integrates the lateral and vertical strain engineering within the film, exhibits both advantages of the multilayer and VAN designs, and achieves an unprecedented level control of the film performances.[138, 156]

The 3D framework thin films were realized for the first time in $La_{0.7}Sr_{0.3}MnO_3$ (LSMO)-CeO_2 systems by inserting 1-3 layers of CeO_2 (or LSMO) interlayers into the LSMO-CeO_2 VAN counterparts and forming 3D CeO_2 (or LSMO) frameworks.[138] Later, the feasibility of this 3D framework concept was demonstrated in LSMO-ZnO system along with the thickness effect study of the ZnO interlayer.[156] The skeletons embedded in all the reported 3D frameworks are homogenous, such as CeO_2, LSMO, and ZnO frames.[138, 156, 157] Studies on heterogeneous frames are still rare. Moreover, the lateral interlayer and its interplay with the surroundings are crucial for the 3D frameworks, since the 3D frames consist of the vertical nanopillars and lateral interlayers. To achieve a precise control on the 3D framework structures, understanding the role of the interlayer within a 3D framework is substantially significant and necessary.

Therefore, this work constructs diverse novel 3D frameworks by inserting one lateral interlayer M of different in-plane matching distance into the LSMO-ZnO VAN system (Figure 5.1 (a)). This interlayer M candidates are selected to be yttria-stabilized zirconia (YSZ, 8 mol% Y_2O_3 + 92 mol% ZrO_2), CeO_2, $SrTiO_3$ (STO), $BaTiO_3$ (BTO), and MgO, respectively. In the developed

structure, numerous ZnO nanopillars connect with the lateral interlayer M and create a heterogeneous frame embedded in the LSMO matrix. The role of the lateral interlayer in determining the 3D heterogeneous framework microstructure and magnetotransport properties is systematically studied by adoption of different interlayer material. The aforementioned interlayer materials are selected as the candidates of interlayer M for the following reasons: (1) the in-plane lattice matching distance of these oxides gradually increases from 3.63 Å (YSZ), 3.83 Å (CeO_2), 3.91 Å (STO), 3.99 Å (BTO), to 4.21 Å (MgO), which enables the systematical in-plane strain tuning of LSMO (a_{LSMO} =3.87 Å) from compressive to tensile (Figure 5.1 (b)). (2) These oxides have sufficiently high resistivity and can serve as tunneling barriers to enhance the magnetotransport properties of LSMO. (3) They all have good chemical, mechanical and thermal stabilities. The chosen oxides also exhibit structural compatibility and have been widely used as the secondary phase in assembling the LSMO-based nanocomposite films with good epitaxial quality.[55, 59-61, 64, 143, 146, 158, 159] The LSMO-ZnO VAN system has been well investigated and exhibited excellent controllable functionalities, especially in the magnetotransport properties.[75, 79, 130, 134] One single interlayer is inserted into the LSMO-ZnO VAN system here for an easy demonstration. The 3D frameworks with multiple interlayers could be explored in the future for highly improved properties. The idea of 3D heterogeneous frame enhances the tunabilities in the VAN-based films for controllable functionalities and highlighted the significance of the engineering in lateral dimension in the VAN systems.

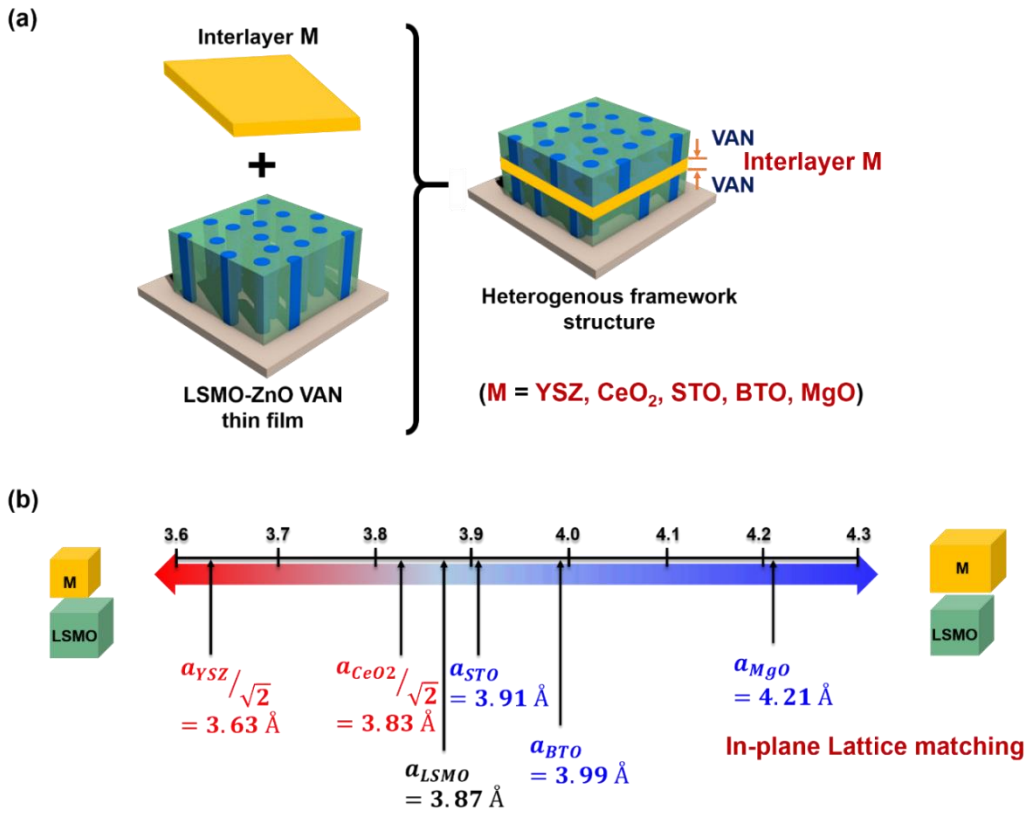

Figure 5.1 (a) Schematic illustration of constructing a three-dimensional (3D) heterogeneous framework by inserting a lateral interlayer M (M = YSZ, CeO_2, STO, BTO, or MgO) into a LSMO-ZnO VAN thin film. (b) Schematic drawing showing the in-plane matching distance relations within these oxides, e.g., YSZ, CeO_2, LSMO, STO, BTO, and MgO.

5.3 Experimental

Pulsed laser deposition (PLD) was used to grow the 3D heterogeneous framework samples on $SrTiO_3$ (STO) (001) substrates along with a composite LSMO-ZnO target (molar ratio of LSMO:ZnO = 3:7, name as L3Z7) and a pure M target (M = YSZ, CeO_2, STO, BTO, MgO, respectively). The 3D heterogeneous framework samples were prepared through a three-step sequential deposition: (1) depositing one LSMO-ZnO VAN layer onto the STO substrate, (2) depositing one single-phase M interlayer on the top, and (3) depositing a second LSMO-ZnO VAN layer on top of the M interlayer. During the deposition, the substrate temperature was controlled

at 750 ºC under a constant oxygen pressure of 200 mTorr with a laser frequency of 10 Hz. After deposition, the substrates were cooled at 10 ºC/min to room temperature under an oxygen pressure of 200 Torr.

The phases and structures were studied by X-ray diffraction (XRD) (PANalytical Empyrean system). The microstructures of these films were analyzed through FEI TALOS F200X FEG STEM at 200 KV equipped with ultrahigh resolution high angle annular dark field (HAADF) detectors and Super-X^{TM} electron-dispersive X-ray spectroscopy. The magnetotransport properties were investigated on a Physical Property Measurement System (PPMS, Quantum Design) in a four point probe configuration. The temperature dependence of resistance (R-T) curves were collected within a temperature range of 10-390 K under zero magnetic field and an applied magnetic field of 1 T perpendicular to the films surface. The magnetoresistance (MR) value was calculated according to the equation below:

$$MR(\%) = \frac{R_0 - R_H}{R_0} \times 100\% \quad (5\text{-}1)$$

Here, R_0 and R_H represent the resistances under zero magnetic field and the magnetic field of 1 T perpendicular to the film surface, respectively.[138, 148, 156]

5.4 Results and discussion

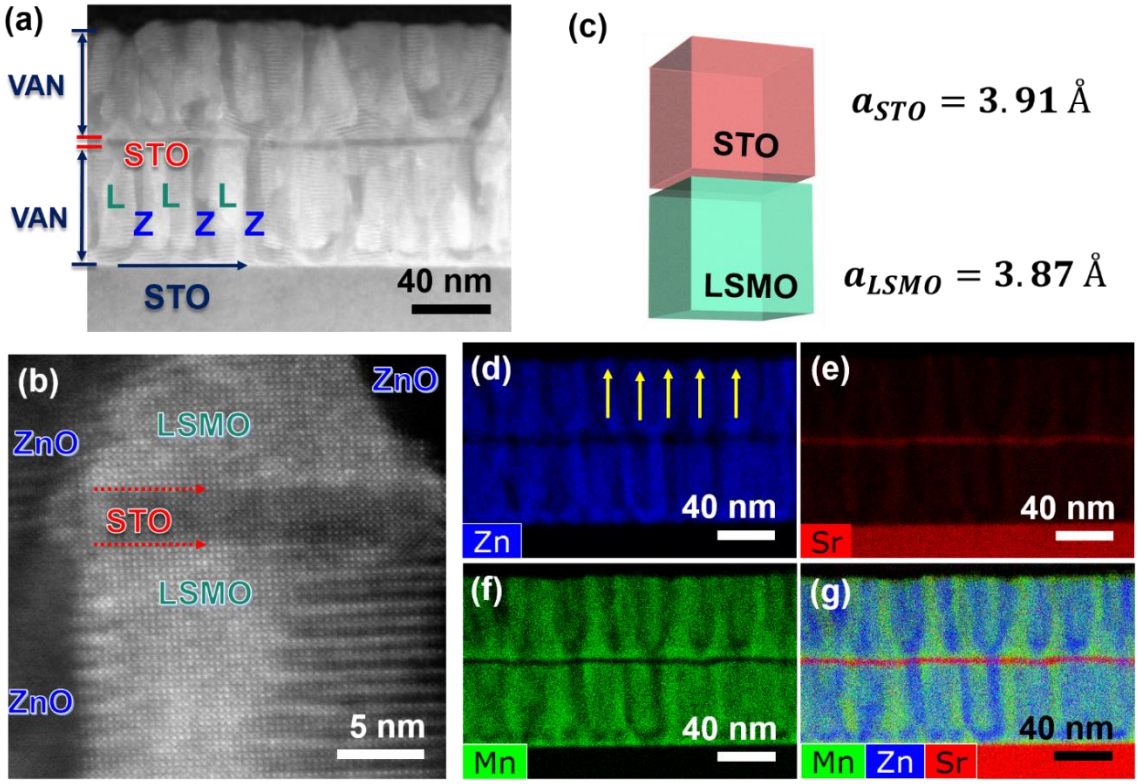

Figure 5.2 (a) Cross-sectional STEM image of the 3D heterogeneous framework with a STO interlayer. (b) Cross-sectional HRSTEM image of the 3D heterogeneous framework at the area of the STO interlayer. (c) Schematic illustration showing a well in-plane lattice match between STO and LSMO lattices. (d-g) Cross-sectional EDS mapping of the 3D heterogeneous framework with a STO interlayer showing clear phase separation and that all the ZnO nanopillars vertically aligned in the VAN layers.

To understand the impact of the interlayer M on crystal growth and microstructure, the different 3D heterogeneous frameworks were systematically studied by varying the interlayer material from YSZ to MgO. Figure 5.2 (a) shows the microstructure of the 3D framework with a STO interlayer. The sequential deposition leads to the vertical stacking of a bottom LSMO-ZnO VAN layer, STO interlayer, and a top LSMO-ZnO VAN layer. All the vertical ZnO nanopillars from the bottom and top VAN layers link to the STO interlayer, creating a 3D interconnected heterogeneous frame embedded in the LSMO matrix. This agrees well with the expected design in

Figure 5.1 (a). The STO interlayer is controlled to a thickness of ~5 nm and shows excellent epitaxial quality grown on the LSMO domain (Figure 5.2 (b)). No misfit dislocation is observed and the LSMO domain on top of the interlayer continues the coherent growth. Compared with other interlayer candidates, STO has a better in-plane lattice match with LSMO (Figure 5.2 (c)). Since the STO interlayer is very thin and coherently grown, the in-plane strain of STO (a_{STO} = 3.91 Å) induced from LSMO (a_{LSMO} = 3.87 Å) is estimated quite small (~-1.02%). Mutually, the strain effect of STO on LSMO lattice is also small, which is closely associated with the vertical orientation of all the ZnO nanopillars in the top VAN layer after the STO interlayer inserted (Figure 5.2 (d)). Moreover, sharp lateral and vertical interfaces are observed in the EDS mapping (Figure 5.2 (d)-(g)), confirming clear phase separation in the 3D framework with a STO interlayer.

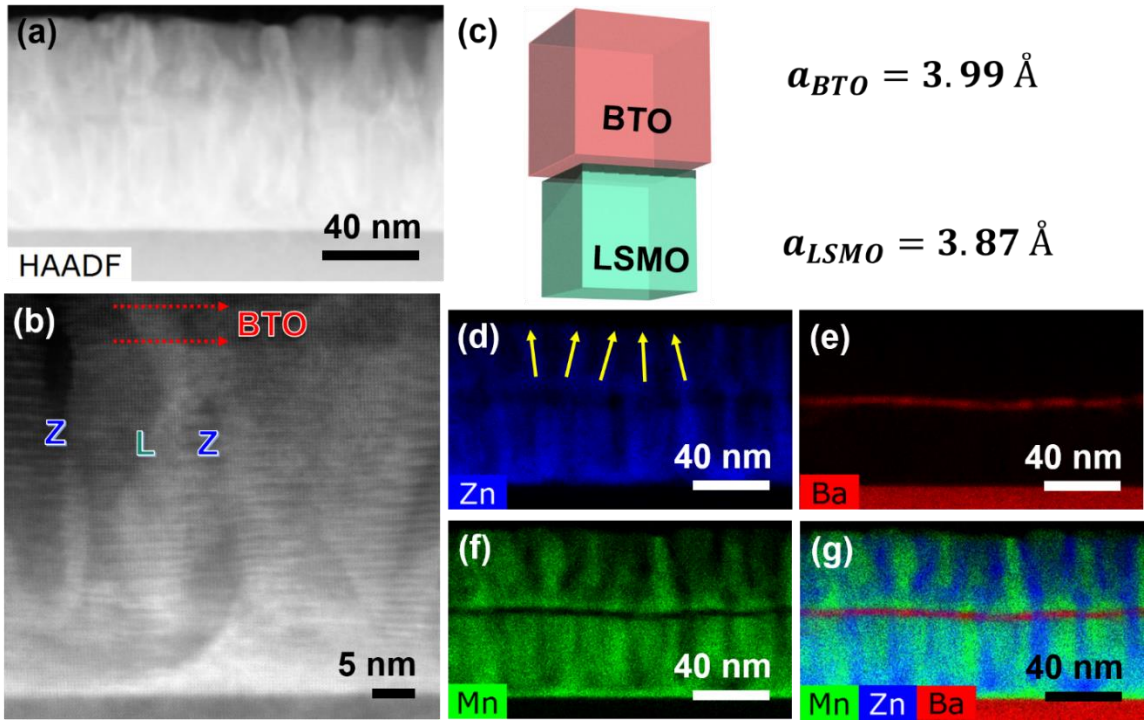

Figure 5.3 (a) Cross-sectional STEM and (b) HRSTEM images of the 3D heterogeneous framework with a BTO interlayer. (c) Schematic illustration showing that BTO has a larger in-plane lattice parameter than LSMO. (d-g) Cross-sectional EDS mapping of the 3D heterogeneous framework with a BTO interlayer.

Figure 5.3 (a) shows the cross-sectional STEM image of the 3D framework with a BTO interlayer. The ZnO nanopillars in the bottom VAN layer are still vertically aligned in the LSMO matrix, similar to the counterpart with a STO interlayer (Figure 5.2 (a)). However, the ZnO nanopillars in the top VAN layer are slightly inclined from the vertical axis after the integration of BTO interlayer. The thin BTO interlayer is coherently grown on top of the bottom VAN layer without misfit dislocation formation (Figure 5.3 (b)). Accordingly, the BTO ($a_{BTO} = 3.99$ Å) interlayer would be under a biaxial compressive strain of ~-3.01% after the cube-on-cube growth on LSMO ($a_{LSMO} = 3.87$ Å) (Figure 5.3 (c)). The larger compressive strain induces the sloping ZnO nanopillars in the top VAN layer (Figure 5.3 (d)). The thin BTO interlayer under the larger biaxial strain is metastable and favors strain relaxation by generating low-angle misoriented or tilted grains and increasing the structural disorder. This process is caused by the balance between the interfacial energy and elastic strain energy, which has been previously reported.[153, 155] The subsequent VAN layer continues the angled lattice orientation and exhibits tilted ZnO nanopillars (Figure 5.3 (d)). Meanwhile, the clear phase separation can be confirmed between the phases in the EDS mapping (Figure 5.3 (d)-(g)).

In conjunction, the case of the interlayer under tensile strain was also studied. Figure 5.4 (a) exhibits the 3D framework microstructure when CeO_2 serves as the interlayer. Similar to the case with BTO interlayer (Figure 5.3), the ZnO nanopillars are vertical in the bottom layer and tilted in the top layer, separated by the CeO_2 interlayer. In this case, the surface roughness is highly enhanced (Figure 5.4 (a)) and good epitaxial quality is well maintained in this 3D framework (Figure 5.3 (b)). Since the CeO_2 unit cell is coupled with LSMO unit cells after a 45º in-plane rotation, CeO_2 is under tensile strain of ~1.04% in-plane (Figure 5.4 (c)). The in-plane tensile strain along with the 45º rotation leads to larger lattice distortion and buckling of the CeO_2 interlayer

(Figure 5.4 (e)), and further induces the sloping ZnO nanopillars grown in the top VAN layer (marked by yellow arrows in Figure 5.4 (d)). Similar phenomena of the tilted growth was observed in YSZ-$Ce_{0.9}Gd_{0.1}O_{1.95}$VAN system.[160] Overall, no intermixing between phases is observed in this framework (Figure 5.4 (d)-(g)). Furthermore, the coherent trend is also noticed in the cases with YSZ (Figure 5.5) and MgO (Figure 5.6) employed as the interlayer, which are under larger strains respectively.

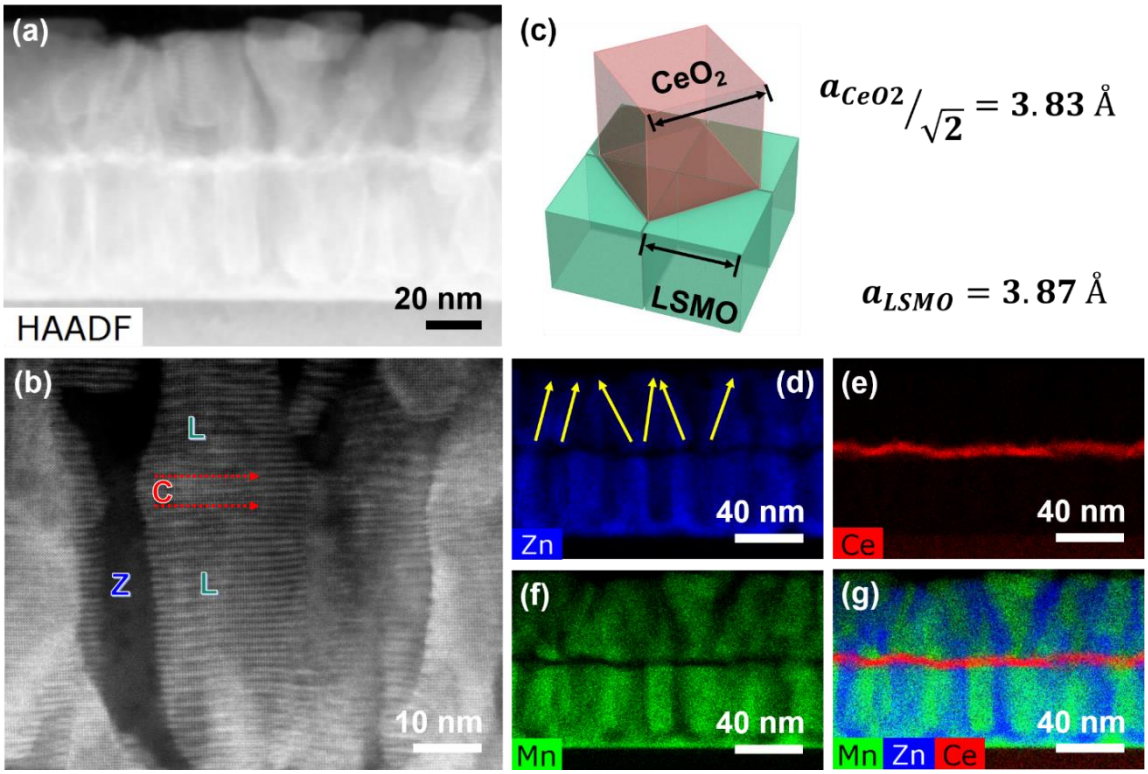

Figure 5.4 (a) Cross-sectional STEM and (b) HRSTEM images of the 3D heterogeneous framework with a CeO2 interlayer. (c) Schematic illustration showing the lattice coupling relation between CeO2 and LSMO. (d-g) Cross-sectional EDS mapping of the 3D heterogeneous framework with a CeO2 interlayer.

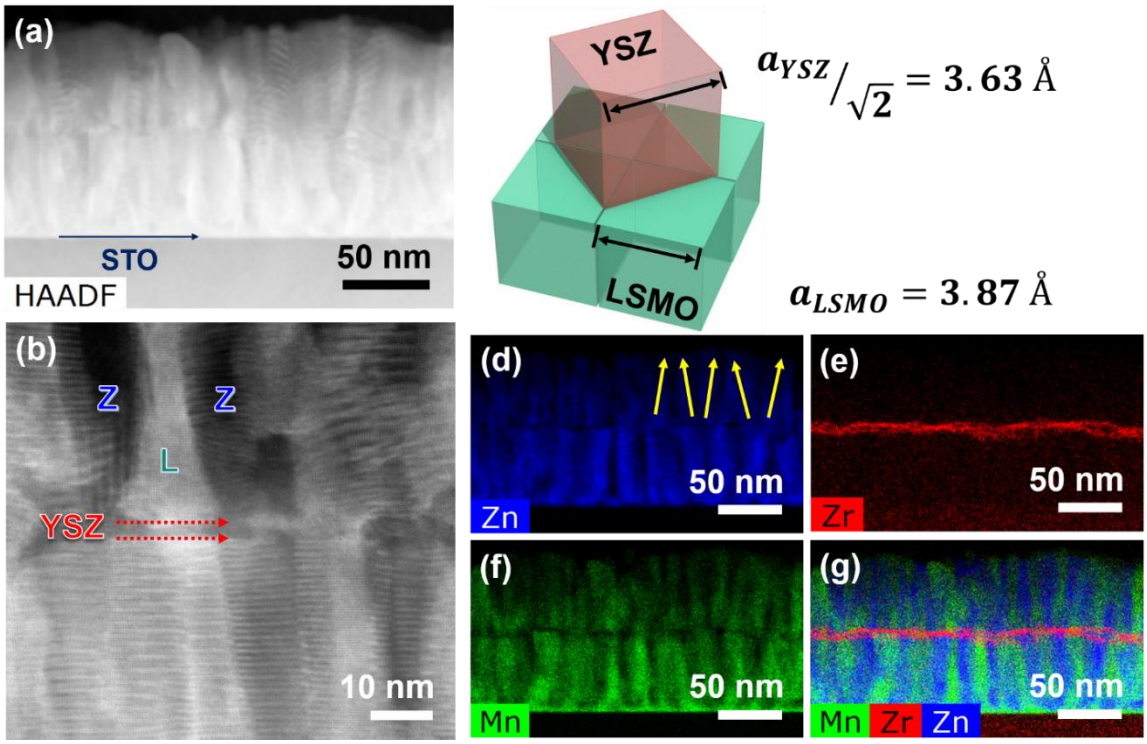

Figure 5.5 (a) Cross-sectional STEM and (b) HRSTEM images of the 3D heterogeneous framework with a YSZ interlayer. (c) Schematic illustration showing the lattice coupling relation between YSZ and LSMO. (d-g) Cross-sectional EDS mapping of the 3D heterogeneous framework with the YSZ interlayer.

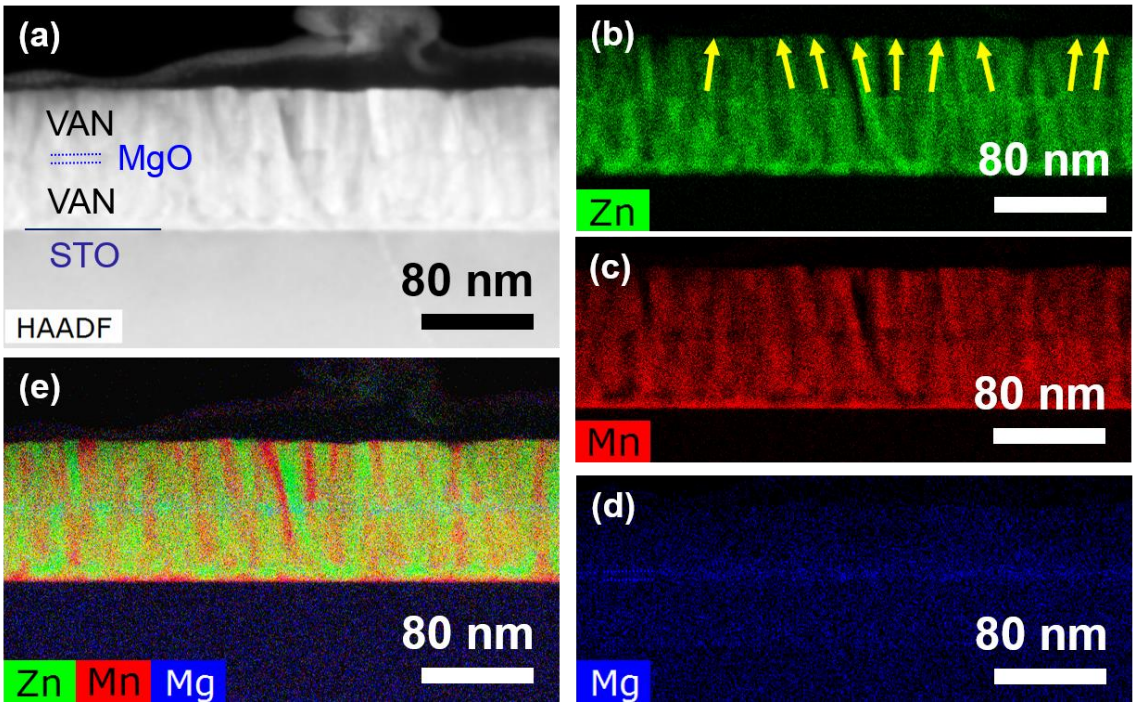

Figure 5.6 (a) Cross-sectional STEM image and (b-e) the corresponding EDS mapping of the 3D heterogeneous framework with the MgO interlayer.

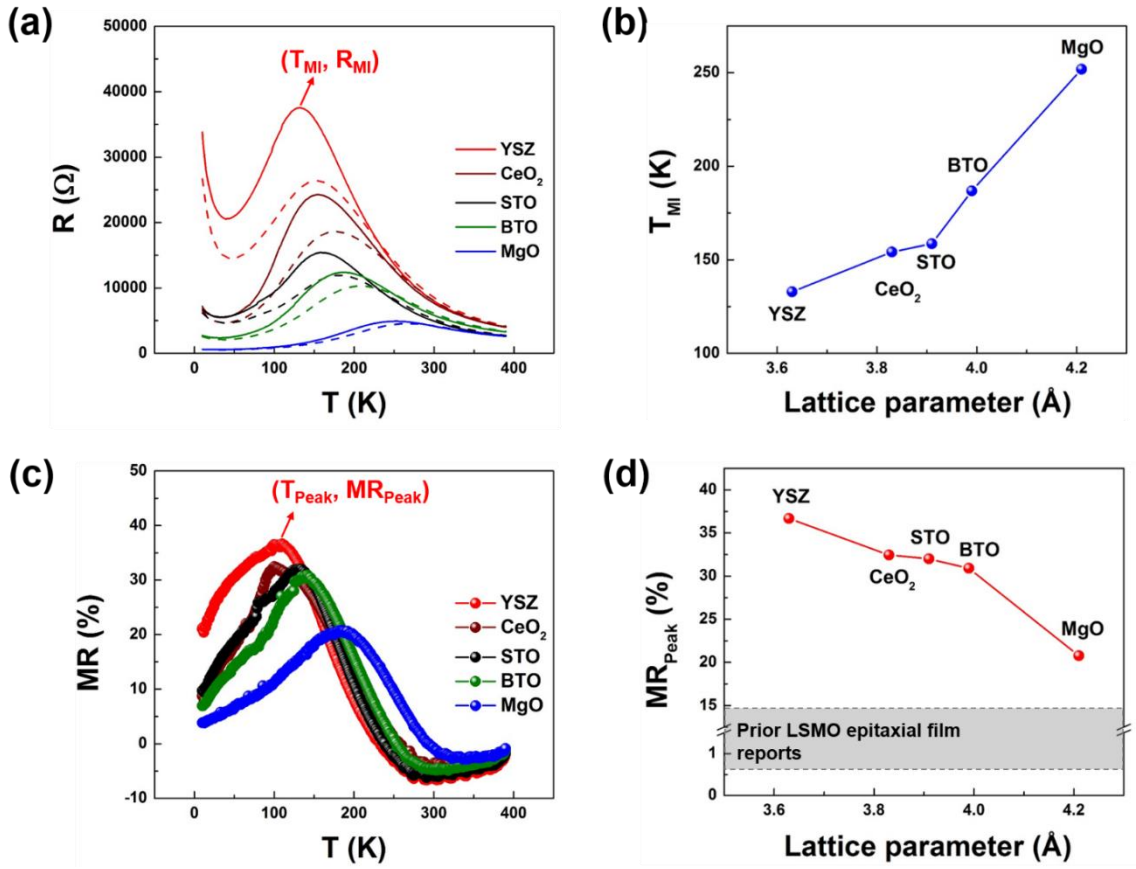

Figure 5.7 (a) Temperature dependence of resistance (R-T) curves for the 3D heterogeneous frameworks with varying the interlayer M (M = YSZ, CeO_2, STO, BTO, MgO) under zero magnetic field (solid line) and an external magnetic field of 1 T (dashed line). (b) The evolving curves of the metal-insulator transition temperature (T_{MI}) of these 3D heterogeneous frameworks. (c) Temperature dependence of magnetoresistance (MR-T) curves for these 3D heterogeneous frameworks. (d) The MR_{peak} value evolution of these 3D heterogeneous framework with the interlayer M varying from YSZ to MgO (the grey rectangular region marks the MR_{peak} range of the previously reported LSMO single-phase epitaxial films which is around 1-16%).[50, 130, 131, 161]

The influence of the various interlayers on the transport properties of the 3D heterogeneous frameworks is systematically investigated in Figure 5.7. The resistances of these frameworks are in general increased within the whole temperature regime by switching the interlayer M from MgO to YSZ (Figure 5.7 (a)). As the temperature is increased from 50 K to 390 K, the resistance of each framework is enhanced at first and then decreased with a well-defined metal-insulator transition.

The metal-insulator transition temperature (T_{MI}) is continuously tuned from ~133 K to ~252 K by varying the interlayer M from YSZ to MgO (Figure 5.7 (b)), suggesting the potentials of the 3D heterogeneous frames in nanoelectronics. The variations of the resistance and T_{MI} are mainly attributed to the integration of the lateral interlayer M which serves as the insulating barrier, blocks the electrical transport channels, and restricts how much current flows through.[162, 163] The enhanced resistivity leads to a decreased T_{MI}, which agrees well with the previous reports.[60, 77, 148, 163-165] The temperature dependence of magnetoresistance (MR-T) curves of Figure 5.7 (c) are derived from the R-T curves. The maximum MR (MR_{peak}) value and its position (T_{peak}) of each framework could be successively tuned by changing the interlayer M. The MR_{peak} value of each 3D framework is gradually reduced from ~36.7% to ~20.8% by varying from YSZ to MgO and the YSZ interlayer optimizes the magnetoresistance of the framework (Figure 5.7 (d)). Although the XRD results do not reveal obvious LSMO peak shifts (Figure 5.8), it is believed that the interlayers of different lattice parameters and crystal structures are still able to cause different biaxial interface effects on the LSMO domains locally, increase the structural and magnetic spin disorder degrees, and reinforce the grain boundary effects.[163] Accordingly, the carrier scattering and current resistance are enhanced under zero magnetic field. Once an external magnetic field of 1 T is applied, the magnetic spins are aligned and the magnetic coupling is strengthened, resulting in reduced resistance and improved magnetoresistance.[31, 55, 130, 166] The electrons can tunnel through the insulating barriers (e.g., ZnO domains and the interlayer M) laterally and vertically, which further boosts the magnetoresistance value.[130, 138] This magnetotunneling effect is closely associated with the electrical structure of the barriers and the barrier-LSMO interfaces. The reducing resistance with the interlayer from YSZ to MgO and current crowd effect leads to the successive decline of the MR_{peak} values.[28, 167, 168] Overall, the 3D heterogeneous frames

empower these nanocomposite films with the dramatically enhanced controllable MR_{peak} values, compared to the previously reported LSMO epitaxial thin films (~1-16%) (marked by grey rectangular region in Figure 5.7 (d)).[50, 130, 131, 161] This design provides a new handle to engineer the microstructure-modified properties in thin films and especially an extra tunabiliy in the free-standing composite films laterally.

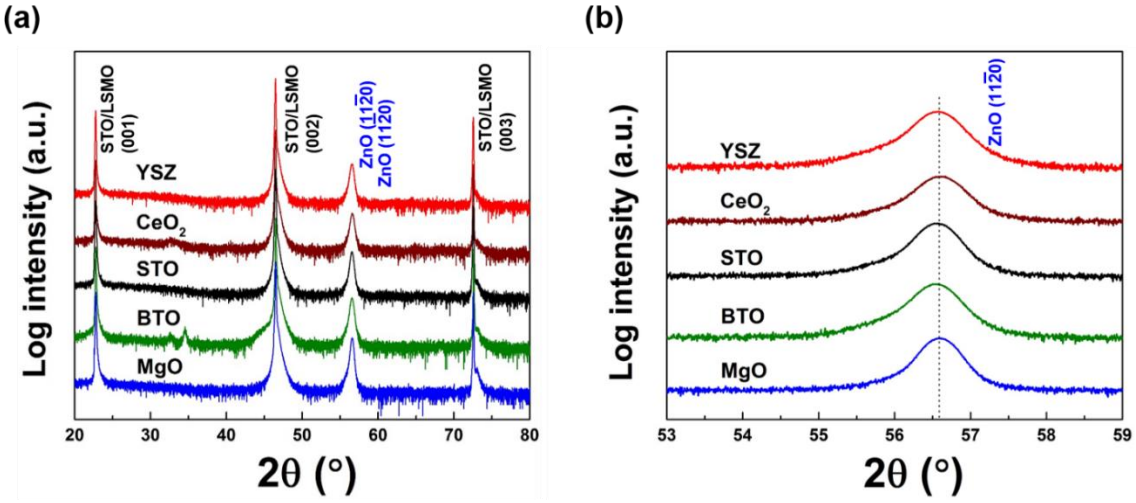

Figure 5.8 (a) XRD θ-2θ patterns of the as-prepared 3D heterogeneous frameworks with various interlayer M (M = YSZ, CeO_2, STO, BTO, MgO). (b) Detailed XRD θ-2θ scans of the 3D heterogeneous frameworks with various interlayer M (M = YSZ, CeO_2, STO, BTO, MgO) at ZnO (11$\bar{2}$0) peak.

5.5 Conclusion

A new microstructure embedding a 3D interconnected heterogenous frame is achieved in a series of three-phase epitaxial nanocomposite films. The 3D interconnected heterogeneous frame is generated by a thin interlayer M sandwiched by two VAN layers of LSMO-ZnO. To understand the significance of the interlayer M in the microstructure and transport properties, the interlayer M material varied within YSZ, CeO_2, STO, BTO, and MgO, whose lateral matching distance of these oxides increases from 3.63 Å (YSZ) to 4.21 Å (MgO). The interlayer with a high lateral lattice-

mismatch causes tilted ZnO nanopillars in the top VAN layer. The interlayer tunes the electrical resistance of the films and enhances T_{MI} from ~133 K to ~252 K. The magnetotransport properties are also highly improved with the magnetoresistance peak value lifted from ~20.8% (MgO) up to 36.7% (YSZ). Overall, the 3D heterogeneous frame design provides a new easy handle to modify microstructures and functionalities of thin films.

CHAPTER 6. STRAIN-DRIVEN NANODUMBBELL STRUCTURE AND ENHANCED PHYSICAL PROPERTIES IN HYBRID VERTICALLY ALIGNED NANOCOMPOSITE THIN FILMS

(This chapter is reprinted with permission from "*Strain-driven nanodumbbell structure and enhanced physical properties in hybrid vertically aligned nanocomposite thin films*" by X. Sun, et al., Applied Materials Today, 16, 204-212 (2019).)

6.1 Overview

Constructing vertical or lateral heterointerfaces using nanocomposite structures is an effective approach for tuning the overall strain state and the resulting physical properties of functional complex oxides. A hybrid $La_{0.7}Sr_{0.3}MnO_3$ (LSMO)-CeO_2 nanocomposite thin film with a novel nanodumbbell structure has been heteroepitaxially constructed by sequentially building composite bilayers with different two-phase volumetric ratios. Despite the different lateral diameters of the CeO_2 domains in the two sequential nanocomposite layers, the CeO_2 phase is coaxially grown within the LSMO matrix and vertically aligned to the substrate, producing the nanodumbbell structure. This structure is ascribed to a strain-driven nucleation and growth process. The high-density, tilted LSMO-CeO_2 heterointerfaces exhibit distinct domain mismatch patterns—different from the vertical counterparts and thus present highly efficient strain tuning and highly improved magnetic and transport performances. More importantly, the well stacked CeO_2 nanodumbbell structure suggest a strain-driven nucleation and growth mechanism in vertically aligned nanocomposite growth and demonstrate a new approach to enhance interfacial coupling and strain tunability in heteroepitaxial nanocomposite thin films by wise practice of the nucleation and growth mechanism.

6.2 Introduction

Strain engineering has been widely adopted as an effective approach for adjusting the lattice distortion and crystal structure of oxides, especially for pervoskite oxide (ABO_3) thin films, along with manipulating their multifunctionalities, such as electrical, magnetic, optical, catalytic and mechanical properties [8, 40, 41, 44, 52, 169-173]. Elastic strain originates from external loading or lattice/domain mismatch [9, 41, 44, 174], and can empower novel functionalities without varying the materials chemistry or creating a new material [44, 173, 175]. Such elastic epitaxial strain is imposed into the oxide thin films through the in-plane substrate clamping effect [9, 40, 48], and affects the crystallographic orientation of the oxide thin films, band structure, mobility of charge carriers in oxide semiconductors, catalytic properties, and transition temperature of ferroelectronics and superconductors [3, 8, 9, 26, 40, 48, 53, 69, 173, 176-178]. However, such lateral strain engineering derived from the substrate is limited within the critical thickness (~ a few nanometers to a few tens of nanometers). Beyond the critical thickness, the film strain relaxes via misfit dislocation generation which degrades the film properties [63, 68, 138, 176, 179]. Even multilayered nanocomposite thin films also suffer from similar issues of strain relaxation after reaching the critical thickness [7, 61].

Therefore, great research interests have been placed on the vertically aligned nanocomposite (VAN) thin films, which were generated by embedding a secondary-phase as either nanodomains or nanopillars into the matrix, interfacing two distinct phases vertically and forming columnar microstructures. The highly enlarged vertical interfacial area in the VAN configuration leads to that the vertical strain engineering dominates the net strain state more than the lateral one induced by the substrate especially in thick films [63, 68, 144, 180, 181]. Moreover, the vertical strain can be conveniently controlled by tailoring the microstructure of the VAN film, such as

morphology tuning, column aspect ratio variation, and density distribution of the secondary-phase nanopillars in the matrix [31, 50, 61, 64, 68, 77]. Many intriguing functionalities have been achieved in the VAN configurations through the control on the strain and microstructure, including the superconductivity, ferroelectricity, multiferroics, ferromagnetism, electronic/ionic transport, and optical properties [50, 54, 61, 64, 77, 143, 148].

Besides the above VAN designs, an interlayered VAN structure has been created very recently by inserting single-phase layers into the VAN thin films and forming 3D interconnected frame structures embedded in the films. This interlayered VAN configuration enables both the vertical and lateral strain engineering within the films [138]. To date, the strain engineering types discussed are solely along either lateral or vertical interfaces [61, 138, 143, 156, 182]. Different interface designs are greatly sought after for enhanced strain engineering and strain-enabled property improvements.

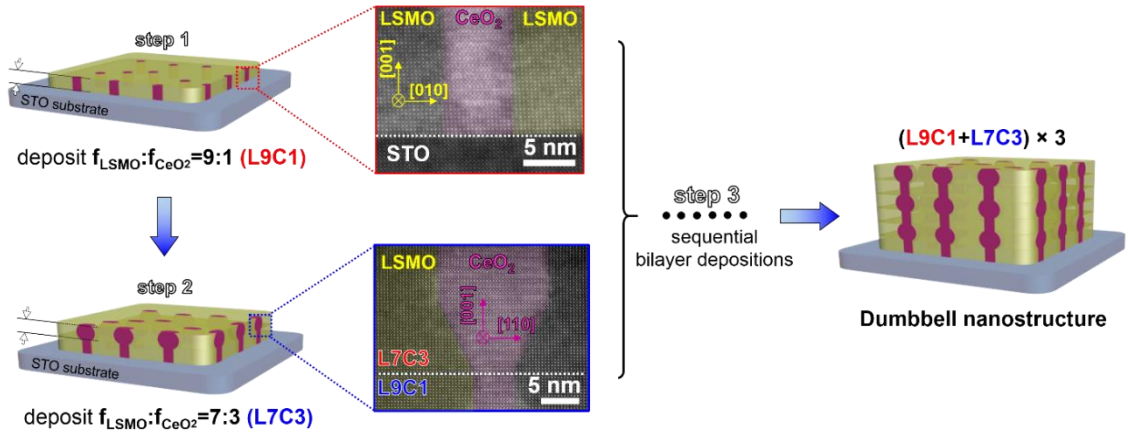

Figure 6.1 Steps of the self-assembled nanodumbbell structure VAN thin film growth process. Step 1: deposition of L9C1 VAN layer. Step 2: deposition of L7C3 VAN layer on top of the L9C1 VAN layer. Step 3: repeat step 1 and 2 to obtain the expected the nanodumbbell structure VAN thin film after sequential bilayer depositions of L9C1 and L7C3 VAN layers.

In this work, a novel hybrid two-phase nanodumbbell structure has been established in the model system $La_{0.7}Sr_{0.3}MnO_3$ (LSMO)-CeO_2 composite thin films through alternate deposition between two-phase nanocomposites of L9C1 (molar ratio of LSMO:CeO_2 = 9:1) and L7C3 (molar

ratio of LSMO:CeO_2 = 7:3) layers in a multilayer fashion onto a $SrTiO_3$ (STO) (001) substrate (Figure 6.1). Different from the previous VANs and single-phase interlayered VAN [50, 77, 138], this novel hybrid nanocomposite structure exhibits very unique tilted heterointerfaces which adopt different domain mismatch patterns, and forms the nanodumbbell-like CeO_2 nanopillars well aligned in the LSMO matrix. This new interface design provides an easy approach for maximizing the strain control and more opportunities for tailoring the physical properties of the epitaxial nanocomposite films, beyond the lateral or vertical heteroepitaxial ones.

Moreover, CeO_2 selected as the secondary phase is due to the following reasons: (1) CeO_2 shows a good lattice matching with the STO substrate after a 45º rotation in-plane and an evident lattice/domain mismatch with the LSMO out-of-plane, so that CeO_2 could efficiently strain LSMO after forming the nanocomposite film. (2) CeO_2 can serve as the nonmagnetic insulating barrier for the magnetoresistance tunneling effect in the LSMO-based films and improve the magnetotransport performances in the spintronic applications. (3) CeO_2 has great thermal and mechanical stabilities [50, 138]. Futhermore, this work demonstrates the feasiblity of multilayer stacking of two nanocomposite systems with nearly perfect pillar registration because of the strain-driven nucleation and growth mechanisms confirmed in the later part of this paper. This opens up enormous opportunities in complex nanocomposite designs with more than one nanocomposite systems.

6.3 Experimental

6.3.1 Thin Film Preparation

The nanocomposite thin films were fabricated on single crystal STO (001) substrates through a pulsed-laser deposition (PLD). The composite targets for PLD were prepared through a

conventional ceramic sintering method. La_2O_3, $SrCO_3$, MnO_2, and CeO_2 powders were fully mixed and ground according to stoichiometric ratios of 9:1 and 7:3 between LSMO and CeO_2, respectively. Then the mixtures were pressed into pellets and sintered at 1100 ºC for 12 h in air to obtain the L9C1 and L7C3 composite targets. Film deposition was performed with a substrate temperature of 700-750 ºC and oxygen pressure of 0.2 Torr (1 Torr = 133.3 Pa). After deposition, the thin films were cooled down to room temperature at a rate of 10 ºC·min^{-1} under 200 Torr oxygen pressure. L9C1 and L7C3 targets were used to deposite the parent L9C1 and L7C3 VAN thin films as reference samples, respectively. The nanodumbbell structure nanocomposite thin film was obtained through alternating deposition from the L9C1 and L7C3 targets. As shown in Figure 6.1, the deposition of the nanodumbbell structure was intiated with 440 pulses from the L9C1 target onto the STO substrate (step 1), and subsequently switched to the L7C3 target for another 440 pulses' deposition (step 2). Step 1 and 2 were repeated three times to create the nanodumbbell structure in this work.

6.3.2 Characterization methods

The phase, orientation, and strain of the thin films were studied using X-ray diffraction (XRD) (PANalytical Empyrean) by θ-2θ, Φ scans, and reciprocal space mapping (RSM). Transmission electron microscopy (TEM), scanning transmission electron microscopy (STEM), and selected area electron diffraction (SAED) patterns were obtained on the Talos 200X at 200 kV, equipped with ultra-high resolution high annular dark field (HADDF) and Super-X^{TM} energy-dispersive X-ray spectra (EDS) detectors. A Themis Z abberation corrected 300 kV FEG S/TEM (including double correctors and monochoromator) was also used to obtain atomically resolved STEM images. Geometric phase analysis (GPA) program (a plug-in o Digital Micrograph package, HREM Research Inc.) was used for mapping the lattice displacement and the strain field variations

based on the original TEM/STEM images. The strain ε is derived from $\boldsymbol{\varepsilon = (d_{hkl}^{local} - d_{hkl}^{reference})/d_{hkl}^{reference}}$ and shows the local strain variations from the selected reference. Here the LSMO lattice is selected as the reference. The GPA ε_{xy} map provides a visualization of the lattice variations and relative strains of CeO_2 from <110> direction with colour contours. Cross-sectional and plan-view TEM samples were prepared through a standard manual grinding and thinning procedure with a final ion-milling step (Gatan PIPS system). Four Au electrodes were deposited by PLD onto the surface of each thin film as contacts of transport measurement in a four point probe configuration (Van der Pauw geometry). Magnetotransport performance was recorded on the Physical Properties Measurement System (PPMS, Quantum Design Dynacool) with applied out-of-plane magnetic field of 1 T and in-plane current. Electrical resistance was recorded in a temperature range of 10-390 K with and without the applied magnetic field of 1 T. Magnetoresistance (MR) values were estimated using Equation 6-1, where $\mathbf{R_H}$ is the electrical resistance with the applied magnetic field and $\mathbf{R_0}$ without applied magnetic field [55, 138].

$$\mathrm{MR}(\%) = \frac{R_0 - R_H}{R_0} \times 100\% \qquad (6\text{-}1)$$

A Magnetic Property Measurement System (MPMS, Quantum Design MPMS-3) with applied in-plane (the applied magnetic field parallel to the film surface) and OP (the applied magnetic field perpendicular to the film surface) magnetic field were used to measure the magnetic properties of the thin films at 300 K.

6.4 Results and discussion

6.4.1 Microstructural characterizations of the nanodumbbell structure

To confirm and study the microstructure of the as-prepared nanodumbbell structure nanocomposite film, both TEM and STEM studies have been conducted along with EDS mapping. Consistent with the expected microstructure, all the CeO_2 nanopillars present a well-defined nanodumbbell structure and are vertically aligned in the LSMO matrix (Figure 6.2 (a)). The bright contrast area represents CeO_2 and the dark contrast area corresponds to the LSMO phase, due to the higher atomic number Z of Ce than that of La, Sr and Mn. The EDS elemental maps in Figure 6.2 (b) confirm the clear phase separation between CeO_2 and LSMO without any apparent intermixing. The overall architecture of the nanocomposite film is determined by the volume ratio (or molar ratio) of the secondary phase in the two layers, which is similar to the previous reports [65, 78]. Because of the alternate growth of the two layers with different molar ratios of LSMO: CeO_2, e.g., 9:1 and 7:3, the lateral diameter of the CeO_2 nanopillars varies periodically from ~3-4 nm to ~13-15 nm. Obvious tilted interfaces are observed and connect the two regions of the different diameters and form the unique nanodumbbell structure (Figure 6.2 (c)). The CeO_2 nanopillars consist of vertical and tilted heterointerfaces with no horizontal interfaces. Since the deposition was conducted in a multilayer fashion, horizontal interfaces could be expected between L9C1 and L7C3 layers; however, driven by the surface energy minimization, tilted interfaces are formed at the transition regions instead of sharp corners.

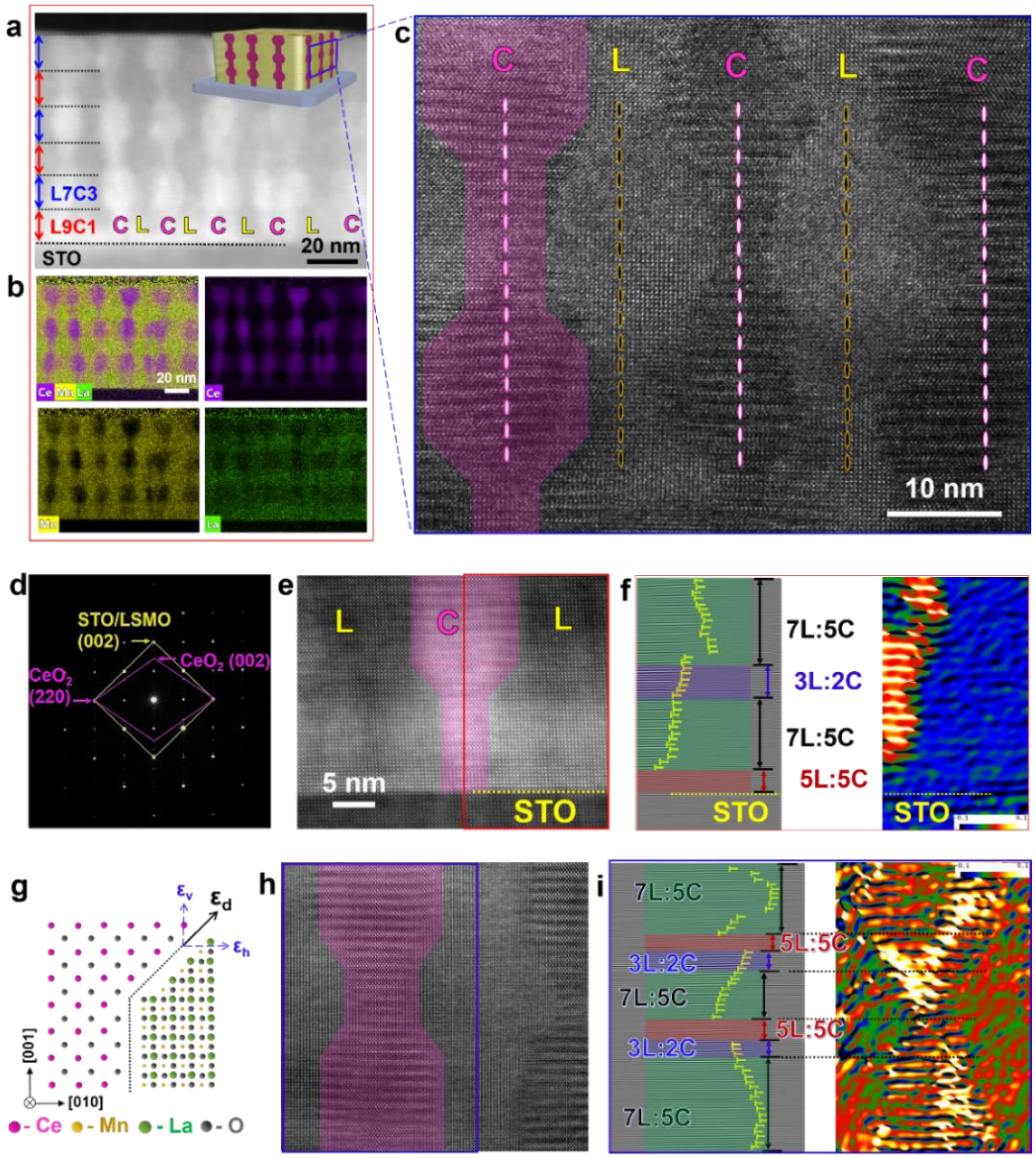

Figure 6.2 (a) Cross-sectional STEM image of the LSMO-CeO_2 nanodumbbell structure film with all the CeO_2 nanopillars vertically aligned in the LSMO matrix. (b) Cross-sectional energy-dispersive X-ray spectra (EDS) mapping of the as-prepared nanodumbbell structure VAN film. (c) Cross-sectional TEM image of the nanodumbbell structure VAN thin film clearly exhibiting that coaxial nanodumbbell-like CeO_2 nanopillars are vertically aligned in LSMO matrix with vertical and diagonal interfaces. (d) Selected area electron diffraction (SAED) pattern of (c). (e) Atomic-scale HRSTEM image at the film-substrate interface, showing a good epitaxial growth quality of the nanodumbbell structure. (f) Fast-Fourier transformed (FFT) image and geometric phase analysis (GPA) ε_{xy} map, corresponding to the selected area (marked by the red frame) on the right side of (e). (g) Atomic model showing the interfacial coupling between LSMO and CeO_2 along vertical and diagonal interfaces. (h) Atomic-scale HRTEM image of the nanodumbbell structure region close to the film surface. (i) FFT image and GPA ε_{xy} map corresponding to the selected area (marked by the blue frame) on the left side of (h).

The high epitaxial quality of the nanodumbbell structure grown on the STO (001) substrate is confirmed by the distinct diffraction dots of the SAED pattern (Figure 6.2 (d)) and the atomic scale high resolution STEM (HRSTEM) image (Figure 6.2 (e)). The fast-Fourier transformed (FFT) image (Figure 6.2 (f)) shows the domain mismatch relations between LSMO and CeO_2 along the vertical and tilted interfaces in the region close to the substrate. Starting from the film-substrate interface, the substrate-strain dominates and results in no misfit dislocation generation right at the starting part of the vertical interface. Therefore, the mismatch relation is 5 unit cells of LSMO (001) coupling with 5 unit cells of CeO_2 (001) (5L: 5C) (marked with the red rectangle) in the initial growth stage of the nanodumbbell structure (Figure 6.2 (f)). This substrate-strain effect also causes the 5L: 5C pattern observed at the film-substrate interfaces in the reference L9C1 and L7C3 counterparts (Figure 6.3). This also results in quite large strain into the films. To release the high strain energy, the following domain mismatch relation along the vertical interface switches to 7 unit cells of to LSMO (001) coupling with 5 unit cells of CeO_2 (001) (7L: 5C) (marked in green rectangles) (Figure 6.2 (f)), similar to the previously reported vertical LSMO-CeO_2 interfaces [50]. More interestingly, a new domain mismatch relation—3 unit cells of to LSMO (001) coupling with 2 unit cells of CeO_2 (001) (3L: 2C) (marked in blue rectangle)—is noticed along the first set of tilted interfaces in the region close to the film-substrate interface (Figure 6.2 (f)). The pattern of 3L: 2C is estimated to theoretically input a much larger strain of -6.787% on LSMO and 7.281% on CeO_2 out-of-plane, according to the detailed strain calculation in the supplementary information. It could strain the phases in the same fashion as the 7L: 5C pattern, but more efficiently. Afterwards the vertical interfaces continue the coupling pattern of 7L: 5C. The corresponding GPA ε_{xy} map in Figure 6.2 (f) shows a similar lattice displacement in the CeO_2 nanopillar as its FFT image. All of these films are in the "thick film" regime with the film thickness of ~110 nm (L9C1), ~85 nm

(L7C3), and ~87 nm (nanodumbbell) (Figure 6.2 and 6.3). The effect from the substrate cannot be completely excluded but can be minimized with the increasing film thickness. The interfacial strain engineering (tilted and/or vertically) within films mainly dominate the overall strain state of the films. Various domain mismatch relations are possible along the vertical and tilted interfaces (Figure 6.2 (g)). When it moves up to the region near the film surface (Figure 6.2 (h)), the mismatch relations along the tilted interfaces reveal the coexistence of both 3L: 2C (marked in blue rectangles) and 5L: 5C (marked in red rectangles) (Figure 6.2 (i)). The 5L: 5C pattern potentially strain the films in the opposite fashion compared to the case of 3L: 2C, i.e., tends to expand the d_{00l}-spacing of LSMO, and could release the accumulated strain energy from the previous 3L: 2C and 7L: 5C relations. The coexistence of 5L: 5C and 3L: 2C may be driven by the system energy minimization. The ultimate impact of the tilted interfaces is determined by the overall competition between these two relations. The strain field evolution of CeO_2 in the GPA ε_{xy} map agrees with the FFT image (Figure 6.2 (i)). Induced from the multilayer growth and minimization of system energy, the tilted interfaces and various strain states successfully distinguish the unique nanodumbbell structure from other previously reported VAN and interlayered VAN counterparts [50, 77, 138].

The importance of growing high quality epitaxial nanocomposite systems and allowing multilayer stacking also leads us to the selection of the LSMO-CeO_2 system as the prototype to demonstrate this design. Other insulating materials (e.g., STO, ZnO, Sm_2O_3, $CoFe_2O_4$) can also be chosen as the secondary phase in the experimental design according the desired physical properties [52, 64, 97, 156].

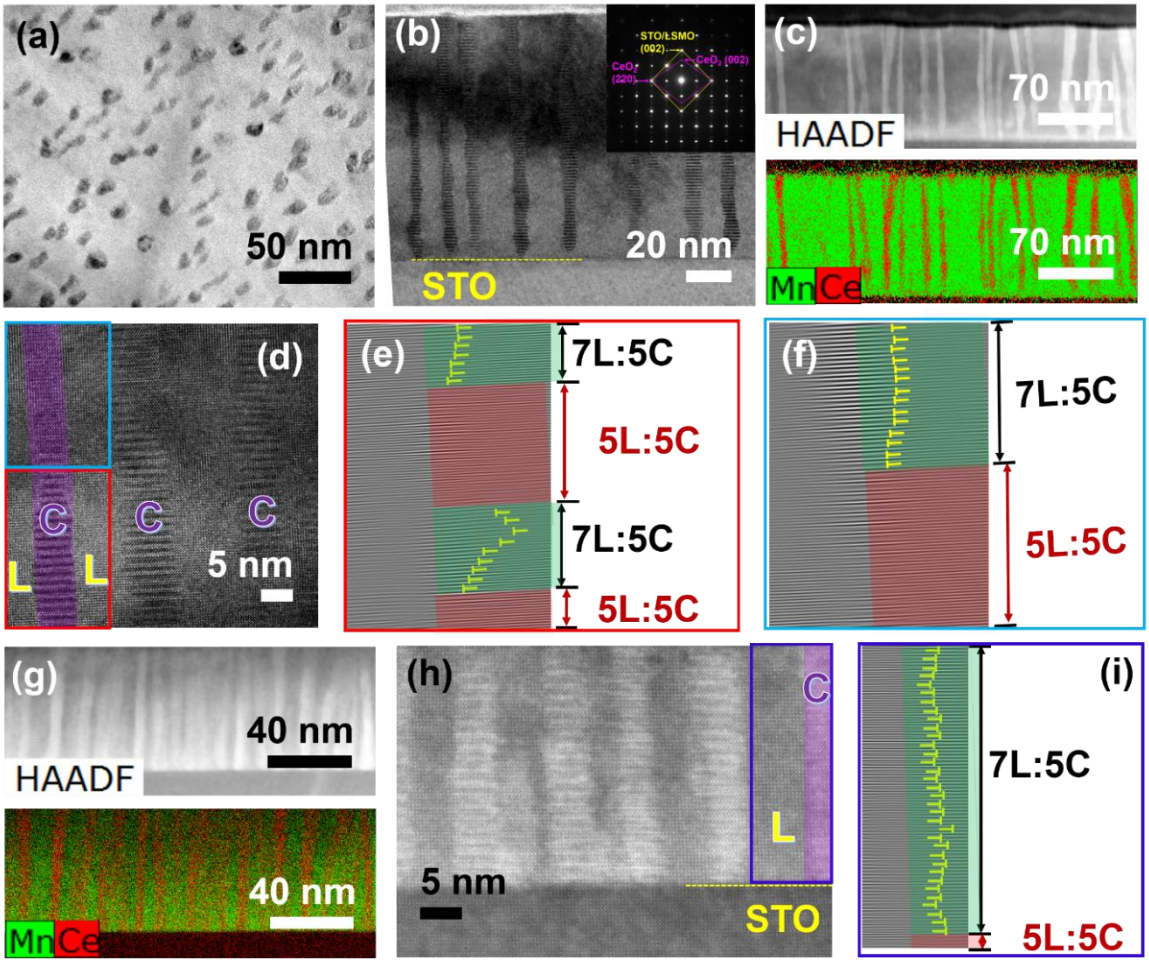

Figure 6.3 (a) Plan-view TEM image of sample L9C1 vertically aligned nanocomposite (VAN) thin film. (b) Cross-sectional TEM image of sample L9C1 VAN thin film with its SAED pattern as inset. (c) Cross-sectional STEM image and the corresponding EDS mapping of L9C1 VAN thin film. (d) Atomic-scale cross-sectional high resolution TEM (HRTEM) image of L9C1 VAN thin film. (e) Fast-Fourier transformed (FFT) image corresponding to the selected area (marked by the red frame) on the bottom of (d). (f) The FFT image corresponding to the selected region (marked by the blue frame) on the top of (d). The FFT images exhibit that the domain mismatching relations between LSMO and CeO_2 out-of-plane (OP) are mainly 7-5 and 5-5 matching between LSMO (001) and CeO_2 (001) along the vertical heterointerface. (g) Cross-sectional STEM image and the corresponding EDS mapping of L7C3 VAN thin film. (h) Atomic-scale cross-sectional high resolution STEM (HRSTEM) image of L7C3 VAN thin film. (i) FFT image of the selected area (marked by the blue frame) on the right side of (i).

6.4.2 Lattice and strain evolutions of the nanodumbbell structure

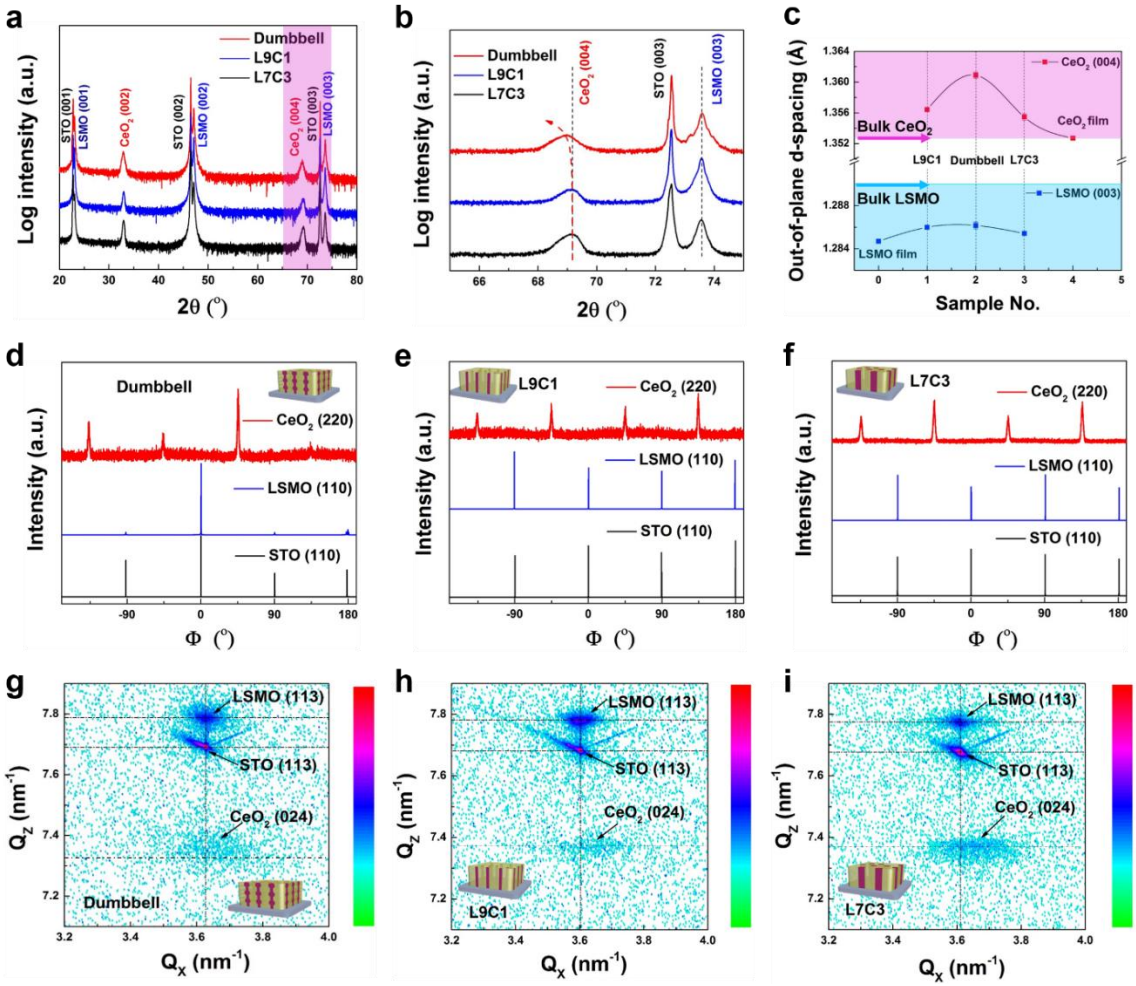

Figure 6.4 (a) XRD θ-2θ patterns of the L9C1, L7C3, and nanodumbbell structure VAN thin films grown on $SrTiO_3$ (STO) (001) substrates. (b) Detailed XRD θ-2θ scans of those LSMO-CeO_2 nanocomposite thin films in the range of CeO_2 (004) and LSMO (003) peaks. (c) Systematic evolution of the $d_{CeO2(004)}$- and $d_{LSMO(003)}$-spacing in the epitaxial thin films (error bars are shown according to Table 6.1). Sample No.0 and 4 represent the pure single-phase LSMO and CeO_2 thin films grown on STO substrates; sample No. 1-3 correpond to the L9C1, dumbell-structured, and L7C3 nanocomposite thin films, respectively. The bulk values of the $d_{CeO2(004)}$ and $d_{LSMO(003)}$ are 1.2900 Å and 1.3528 Å, marked with purple and blue. Thus, the purple rectangular area marks the out-of-plane tensile strain region of CeO_2 and the blue rectangular area covers the out-of-plane compressive strain region of LSMO, comparing with their bulk d_{00l} values. Φ scans of (d) the nanodumbbell structure, (e) L9C1, and (f) L7C3 VAN thin films on STO (110), LSMO (110), and CeO_2 (220). Reciprocal space maps (RSM) of (g) the nanodumbbell structure, (h) L9C1, and (i) L7C3 VAN nanocomposite thin films near STO (113).

Table 6.1 Out-of-plane (OP) d-spacing and Strain Evolution of LSMO-CeO_2 Nanocomposite and Their Single-phased Thin Films

Sample Name		**CeO_2 d_{004} / (Å)**	**Error / (E-4)**	**OP Strain of CeO_2 (Compared with Bulk) / (%)**	**LSMO d_{003} / (Å)**	**Error / (E-4)**	**OP Strain of LSMO (Compared with Bulk) /(%)**
Bulk LSMO					1.2900		
Thin Films Grown on STO	**Pure LSMO**				1.2847		-0.411
	L9C1	1.3564	0.76	0.276	1.2860	1.61	-0.310
	Nanodumbbell	1.3609	3.99	0.606	1.2862	3.14	-0.295
	L7C3	1.3555	4.30	0.203	1.2854	1.01	-0.357
	Pure CeO_2	1.3527					
Bulk CeO_2		1.3528					

All those domain mismatch relations put the lattice into different strain states locally, while the net OP strain for each film and the d_{00l}-spacing evolutions were investigated through XRD. Figure 6.4 (a) and 6.5 exhibit the XRD θ-2θ patterns of the nanocomposite thin films and the single-phase thin films grown on STO (001) substrates, respectively. The distinguished (00l) peaks of CeO_2 and LSMO phases in all the XRD θ-2θ scans demonstrate that both phases grow highly textured on the STO substrates along the out-of-plane direction. The relative ratio of LSMO:CeO_2 varies the d-spacing of each phase and peak position.[77] Since the nanodumbbell structure was obtained through alternating the deposition of L9C1 and L7C3, the CeO_2 (004) peak of the nanodumbbell structure is predicted to be between that of the parent thin films. However, the CeO_2 (004) peak of the nanodumbbell structure clearly shifts to a much lower angle position than the L9C1 and L7C3 films (Figure 6.4 (b)). This correlates to an abruptly enhanced $d_{CeO2(004)}$-spacing

in the nanodumbbell structure (1.361 Å) than that of the L9C1 (1.356 Å) and L7C3 (1.355 Å) thin films (Figure 6.4 (c)). Compared with its bulk lattice, CeO_2 of the nanodumbbell structure is in a much larger tensile strain of ~0.606% than that of L9C1 (~0.276%) and L7C3 (~0.203%) counterparts. It could be explained by the coupling pattern of 3L: 2C along the tilted interfaces (Figure 6.2 (f) and (i)), which increases the density of misfit dislocations and expands the $d_{CeO2(00l)}$-spacing according to the detailed strain estimation in supplementary information. On the other hand, the LSMO of those nanocomposite films is compressively strained out-of-plane and the variations of $d_{LSMO(003)}$-spacing are almost negligible (Figure 6.4 (c)). The variations could be more distinguishable if the relative ratio of CeO_2 is highly increased as well as the tilted interfacial area in the nanodumbbell structure. Accordingly, the net strain on each phase of the films is the synergistic effect between the substrate-clamping effect (laterally) and interfacial coupling within the film (tilted and vertically), and also the accumulated result of the lattice/domain mismatch along interfaces and the interfacial area. Meanwhile, it is significantly influenced by the composition of the system and instrinsic properties of each phase.

All the Φ scans in Figure 6.4 (d)-(f) demonstrate the cube-on-cube growth of LSMO on STO with no in-plane rotation (LSMO(001) || STO(001) and LSMO[100] || STO[100]). The CeO_2 has a 45 degree in-plane rotation on STO (i.e., CeO_2(001) || STO (001) and CeO_2[110] || STO[100]). This growth pattern is consistent with previous reports.[50, 77, 138] In the reciprocal space mapping (RSM) studies (Figure 6.4 (g)-(i)), the distinct diffraction spots of LSMO and CeO_2 illustrate the high epitaxial quality of those nanocomposite thin films on STO (001) substrates. The peak evolutions in the RSM results agree with the observations in Figure 6.4 (c). For example, LSMO (113) spots of Figure 6.4 (g)-(i) remain at similar relative positions to STO (113) along the Q_Z direction, revealing minor variations of the $d_{LSMO(003)}$-spacing in the three thin films. The

nanodumbbell structure shifts the CeO_2 (024) spot downwards along the Q_Z direction compared with L9C1 and L7C3, reflecting the elongation of the d_{001}-spacing in the nanodumbbell-like CeO_2 nanopillars.

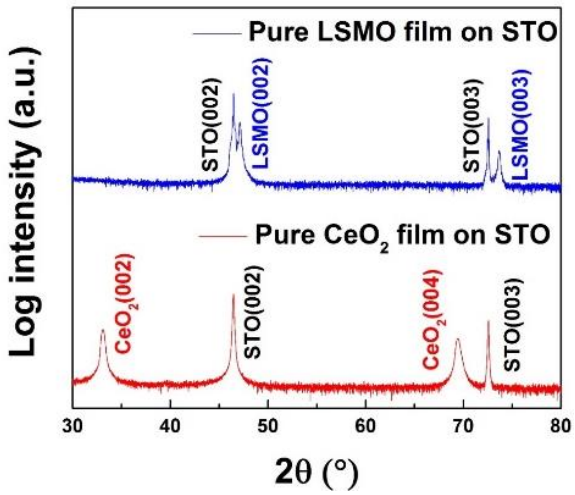

Figure 6.5 XRD *θ-2θ* patterns of the single-phase $La_{0.7}Sr_{0.3}MnO_3$ (LSMO) and CeO_2 thin films grown on $SrTiO_3$ (STO) (001) substrates.

6.4.3 Property enhancement of the nanodumbbell structure

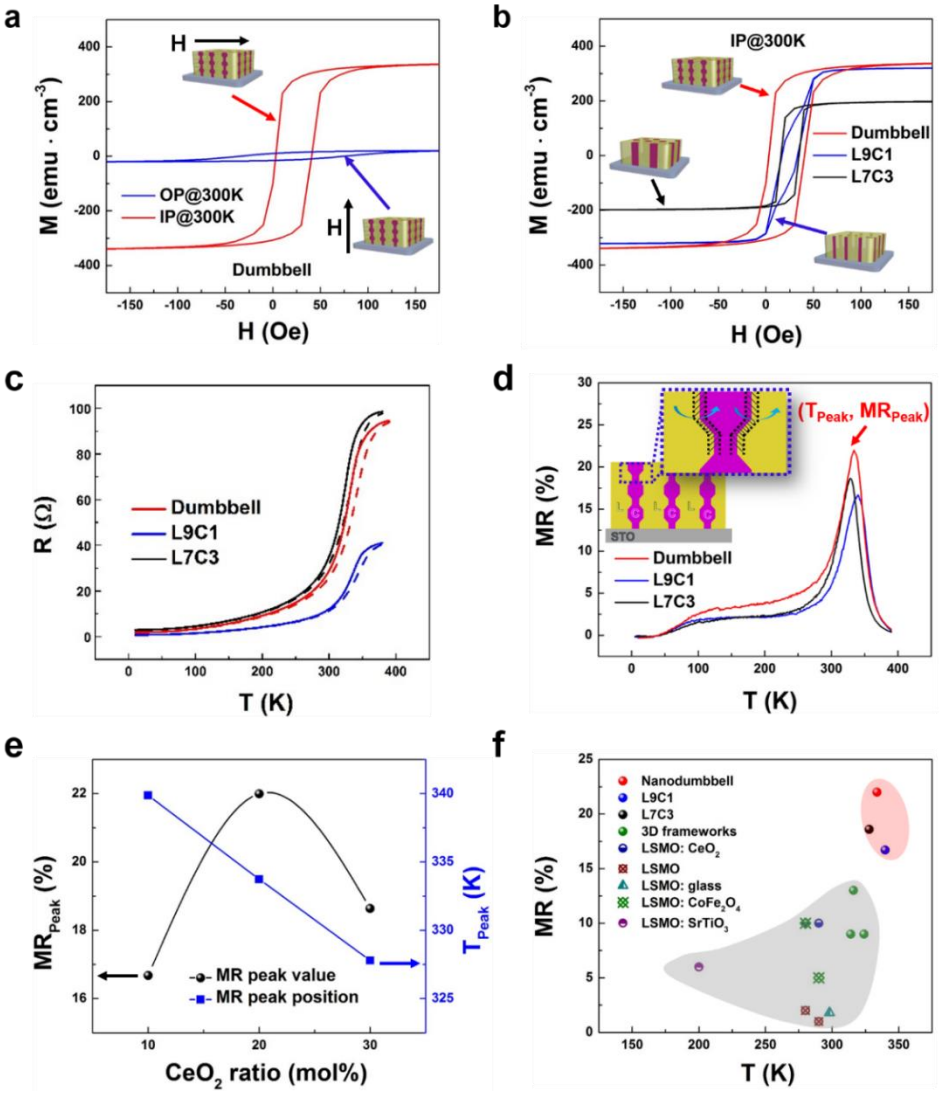

Figure 6.6 (a) Out-of-plane (OP: the applied magnetic field perpendicular to the film surface) and in-plane (IP: the applied magnetic field parallel to the film surface) magnetic hysteresis loops of the nanodumbbell structure VAN thin film measured at 300 K, illustrating the strong anisotropy. (b) IP magnetic hysteresis loops of the L9C1, L7C3, and nanodumbbell structure thin films measured at 300 K. The magnetization here is based on the volume of the LSMO phase, which is roughly calculated according to the film volume and the molar ratio of LSMO. (c) Temperature dependence of resistance (R-T) curves and (d) temperature dependence of magnetoresistance (MR-T) curves for the L9C1, L7C3, and nanodumbbell structure VAN thin films. (e) Evolution of the MR peak value (MR_{Peak} %) and the corresponding temperature (T_{Peak}) with the increasing CeO_2 molar ratio in the L9C1, nanodumbbell structure, and L7C3 VAN thin films. (f) Comparison of the MR peak values of L9C1, L7C3, and nanodumbbell structure nanocomposite thin films with the previously reported LSMO-based composite films above 150 K [77, 122, 130, 131, 135, 138, 144, 183].

This new nanodumbbell structure design not only provides an efficient method to tune the strain of the films, but also achieves a higher degree of property improvements compared with its parent VAN thin films. The magnetic and electrical properties of perovskite oxides are mainly governed by the structure, lattice distortion, strain, and grain boundaries [36, 55, 166]. The tilted interfaces and larger strain give the nanodumbbell structure more advanced magnetic and transport properties (Figure 6.6). The magnetic hysteresis loops in Figure 6.6 (a) show the magnetic anisotropy of the nanodumbbell structure and its preferred magnetic axis along the in-plane direction. Figure 6.6 (b) compares the in-plane hysteresis loops measured for the nanodumbbell structure, L9C1, and L7C3 thin films at 300 K. The magnetization is based on the volume of the LSMO phase in each film. The nanodumbbell structure exhibits the highest saturation magnetization (M_S) of ~337 emu·cm^{-3}, compared with the L9C1 (~320 emu·cm^{-3}) and L7C3 (~197 emu·cm^{-3}) nanocomposites. The origin of this increased Ms is believed to be the enhanced strain tuning enabled by the tilted interfaces in the nanodumbbell structure. The tuning of the Ms in the LSMO-based nanocomposite thin films is associated with the strain control on the LSMO phase. As illustrated in Figure 6.4 (c), the LSMO phase of the three films is under compression out-of-plane compared with the bulk LSMO. The relaxation of the compressive strain of LSMO (Table 6.1) could elongate the center MnO_6 octahedra and the Mn-O bond length, reducing the Mn-O-Mn bond angle and further influencing the Ms, which agrees well with the previous reports [166, 184, 185]. For example, F. Yang et al. reported the decreasing Ms along with the reduction of c/a from 0.987 to 0.962, corresponding to the gradually increased compressive strain in out-of-plane direction [184]. The M_S of the three films evolves coherently with the d_{003}-spacing of the LSMO as seen in Table 6.1.

The temperature dependent resistance (R-T) curves of the three nanocomposite films are plotted in Figure 6.6 (c). The resistance of each film increases with the temperature, demonstrating a typical metallic behavior due to the large portion of LSMO (~70-90 mol%) in the three films. No evident metal-insulator transition temperature is observed. With increasing amounts of CeO_2 in the L9C1, nanodumbbell structure, and L7C3 thin films, the resistance is gradually enhanced over the entire temperature regime. The nanodumbbell structure shows a relatively high resistance, almost similar to that of L7C3. Compared to the L9C1 and L7C3 reference samples, the nanodumbbell structure exhibits highly enhanced magnetotransport properties (Figure 6.6 (d)), which are attributed to the tilted interfaces and various strain states throughout the sample thickness. More specifically, the 3L: 2C pattern along the tilted interfaces largely compresses the LSMO out-of-plane and reduces the Mn-O-Mn bond angles locally, which directly suppresses the double exchange interaction and electron hopping between Mn ions [186, 187]. The 5L: 5C pattern on a few interfaces tends to expand the LSMO lattice in out-of-plane direction and may be not helpful to the magentotransport performances locally. But the 3L: 2C and 7L: 5C patterns dominate in general. The increased magnetic disorder also scatters the carriers more and therefore highly enhances the resistance [126]. The structural distortion and magnetic disruption of magnetic order both boost the colossal magnetoresistive effect in LSMO along the tilted interfaces (the inset of Figure 6.6 (d)) [188]. On the other hand, the mismatch relations along the tilted interfaces broaden the phase boundary region in the nanodumbbell structure, boost the oxygen deficiency, intensify the barrier for carrier migration, and further enhance the magnetotunneling effect [55, 97, 166, 189-191]. The colossal magnetoresistive effect and magnetotunneling effect collectively lead to the highly enhanced magnetotransport properties of the nanodumbbell structure compared to the L9C1 and L7C3 reference samples (Figure 6.6 (d)). The CeO_2 ratio dependence of the MR peak

value (MR_{Peak}) is shown in Figure 6.6 (e) and so is the corresponding peak temperature (T_{Peak}). With the molar ratio of CeO_2 increasing from 10% to 30%, T_{Peak} proportionally decreases from ~340 K to ~328 K in the L9C1, nanodumbbell structure, and L7C3 thin films. The nanodumbbell structure presents the largest MR_{Peak} of ~22%, compared with the L9C1 (~17%) and L7C3 (~19%) VAN counterparts. This improvement of the MR_{Peak} can be explained by the intensified grain boundary effect and obstructed magnetic spin alignment [31, 55]. Consequently, the tilted interfacial coupling has a higher sensitivity in the modulation of the lattice distortion, strain states, and transport properties. With the limited tilted interfacial area, the nanodumbbell structure film has achieved the MR_{Peak} improvement of ~30% and 16% over its parent L9C1 and L7C3 films above room temperature, respectively. Further enhancement could be pursued by increasing the tilted interfacial area and strengthening the strain tuning. Figure 6.6 (f) highlights the superior MR performance of this nanodumbbell structure with the tilted interfaces compared with prior reported LSMO-based composite films. The nanodumbbell structure exhibits the highest MR_{Peak} value (~22%) at the temperature of ~334 K compared to the LSMO-based epitaxial films in the temperature regime above 150 K [77, 122, 130, 131, 135, 138, 144, 183]. Therefore, this hybrid nanocomposite design can be used to develop more promising candidates to advance the next-generation magnetic sensors, storage devices, and spintronics.

6.4.4 Strain-driven growth

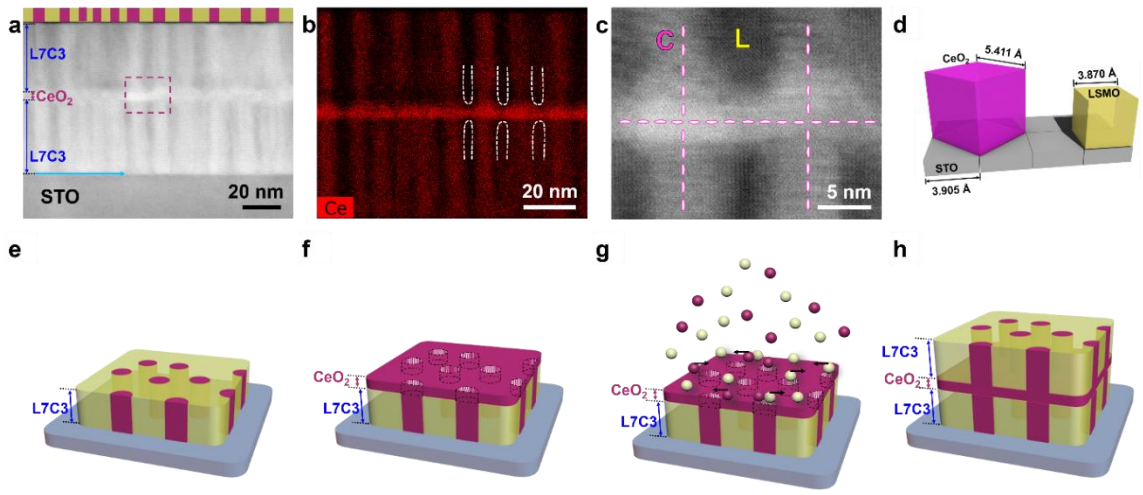

Figure 6.7 (a) Cross-sectional STEM image of the self-assembled three-dimensional (3D) framed thin film interlayered by a single-phase CeO_2 lateral interlayer. The bars on the top mark the distribution of LSMO and CeO_2 phases in the top VAN layer. The purple bars represent LSMO and the yellow ones correspond to CeO_2. (b) EDS mapping of element Ce in the as-constructed 3D framed thin film. (c) High resolution STEM image of the 3D framed thin film at the lateral CeO_2 interlayer, corresponding to the purple dashed rectangular frame in (a). (d) Schematic illustration of the in-plane lattice matching relations of STO (100) || LSMO (100) || CeO_2 (110). Schematic diagrams showing the growth process of the self-assembled 3D framed microstructure with fine alignment of vertical CeO_2 nanopillars: (e) growth of the first L7C3 (molar ratio of LSMO/CeO_2 = 7:3) VAN layer, (f) a lateral CeO_2 interlayer deposited on top of the first VAN layer as a "buffer" layer (the bright spots mark the regions under a different strain status from the rest), (g) depositing the second L7C3 VAN layer onto the lateral CeO_2 interlayer with different strain distribution, (h) the 3D CeO_2 framed microstructure with the vertical CeO_2 nanopillars well aligned in the VAN layers.

Interestingly, all the nanodumbbell-like CeO_2 nanopillars are coaxially grown and perpendicularly oriented to the STO substrate instead of being tilted or curved even though they are generated by alternate growth of L9C1 and L7C3 layers. It was reported that the adatoms favor attaching to their identical composition during the PLD process and thus form those columnar VAN architecture [64]. However, we believe that strain could also play a major role in the orientation/alignment of the nanodumbbell-like and conventional rod-like pillars. Such strain-driven orientation/alignment was demonstrated by interlayering the LSMO-CeO_2 VAN thin film

with a relatively thin CeO_2 interlayer. Figure 6.7 (a)-(c) display the cross-sectional microstructure of this interlayered thin film. A homogeneous CeO_2 interlayer of ~1-2 nm thin connects with the vertical CeO_2 nanopillars from the top and bottom VAN layers, and forms a 3D CeO_2 framework embedded in the LSMO matrix. More importantly, the locations of the CeO_2 nanopillars in the top VAN layer spontaneously match with those in the bottom VAN layer, although the CeO_2 interlayer has interrupted the growth of the bottom VAN layer.

This spontaneous alignment of CeO_2 nanopillars can be explained by a strain-driven nucleation and growth mechanism. According to the lattice matching relationship (Figure 6.7 (d)), CeO_2 unit cell is calculated to be under a tensile strain (1.150%) in-plane when it is stacked on top of LSMO. After the sequential deposition of the bottom VAN layer (Step 1, Figure 6.7 (e)) and the CeO_2 interlayer (Step 2, Figure 6.7 (f)), the uniform coverage of the CeO_2 buffer has prevented the influence of the composition variation across the surface. Only the in-plane strain varies across the homogeneous CeO_2 interlayer due to the underlying VAN layer. The CeO_2 regions on top of LSMO are under tensile strain in-plane, while the CeO_2 areas (marked by white lines) are unstrained or under compression in-plane on top of those CeO_2 nanopillars (as the 5C:7L coupling pattern places the CeO_2 nanopillars in compression in-plane in the bottom VAN layer) (Figure 6.7 (f)). In Step 3 to grow another VAN layer (Figure 6.7 (g)), once the adatoms of LSMO and CeO_2 reach the surface, they diffuse and nucleate preferentially based on the strain variation across the CeO_2 interlayer, resulting in the well aligned CeO_2 nanopillars across the interlayer (Figure 6.7 (h)). Overall strain driven nucleation induces the well aligned coaxial growth of the CeO_2 nanopillars and thus the nanodumbbell architecture in the 3D framework.

The unique nanodumbbell structure with tilted interfaces has efficiently improved the out-of-plane strain of CeO_2 from ~0.203% up to ~0.606%, compared with the conventional VAN

architecture with only vertical interfaces. It inceases the diversity of interfacial coupling and strain tuning type in the epitaxial nanocomposite films. Actually this nanodumbbell structure design can be extended to a broader range of nanocomposite systems and benefit more microstructure- and strain-enhanced functionalities (e.g., ferromagnetism, ferroelectricity, superconductivity, ionic conduction, et al.) in data storage and energy related fields [52]. Moreover, the strain driven nucleation and growth mechanism can be used for heterogeneous pillar stacking growth in future 3D nanocomposite designs with multifunctionalities.

6.5 Conclusion

In this work, the hybrid LSMO-CeO_2 nanocomposite system is taken as a model system to demonstrate the feasibility of forming tilted 2-phase heterointerfaces to accomplish extraordinary level of strain engineering and the related property improvements. By alternating the relative ratio of LSMO:CeO_2 L7C3 and L9C1 in a multilayer fashion, nanodumbbell-like CeO_2 nanopillars are created and vertically aligned in the LSMO matrix. The unique tilted interfaces of this new microstructure enable a different lattice coupling relationship of LSMO and CeO_2 from that of the vertical interfaces and a higher level of strain state has been achieved (e.g., out-of-plane tensile strain of ~0.606% in CeO_2). The ideal alignment of the vertical CeO_2 nanopillars confirms the significance of the strain in the 2-phase nanocomposite nucleation and growth process. Overall, this work provides another degree of design flexibility by producing tilted heterointerfaces for strain tuning and physical property control. The importance of strain in the overall nucleation and growth mechanisms of self-assembled heteroepitaxial nanocomposite thin films further provides design guidelines for new 3D nanocomposite systems for multifunctionalities.

CHAPTER 7. SUMMARY AND FUTURE WORK

In this dissertation, we systematically investigated the correlation of the 3D strain engineering, microstructure, interfaces and functionalities within the self-assembled LSMO-based VAN thin films. VAN architecture can be promoted into multiple types of novel interesting microstructures such as 3D frameworks, heterogeneous frameworks, and nanodumbbell structure, which enables novel interfaces, higher level of strain engineering, and intriguing physical properties. Those advanced VAN architecture provides more opportunities for the fundamental scientific studies and also holds huge promises for the future technology.

First, a novel concept of 3D strain engineering has been enabled within the interlayered LSMO-CeO_2 VAN thin films (so called 3D LSMO-CeO_2 frameworks) by inserting 1-3 CeO_2 (or LSMO) interlayers into LSMO-CeO_2 VAN structures and creating 3D interconnected CeO_2 (or LSMO) scaffolds embedded in the epitaxial thin films. Combining both vertical and lateral interfaces within the films, this new 3D framework design achieves higher level of strain engineering and record high magnetoresistance value in LSMO-based composite thin films. Then, the feasibility of the 3D framework design is demonstrated in a different composite system LSMO-ZnO. Even though ZnO has different crystal structure and growth pattern from CeO_2 when grown on STO substrate, the 3D framework microstructure is still well constructed with 3D interconnected ZnO frames embedded in LSMO matrix. Meanwhile, the interlayer thickness effect is systematically studied on the microstructure, strain states and magnetotransport properties with the average interlayer thickness gradually increasing from ~1 to ~10 nm. The magnetotransport performances of the films are optimized due to the magnetotunneling effect when the average interlayer thickness is controlled at ~2 nm. Meanwhile, the lattice influence of the interlayer is also

studied on the subsequent crystal growth and overall 3D framework microstructure in LSMO-ZnO VAN system by changing the interlayer materials from YSZ to MgO and forming 3D heterogeneous frames embedded. The biaxial matching distance of interlayer is continuously enhanced from 3.63 Å to 4.21 Å. Large lattice mismatch between interlayer and LSMO-ZnO VAN layers induce tilted domain growth in the top VAN layer.

The aforementioned 3D strain engineering approach involves only lateral and vertical interfaces within the films. A novel tilted interfaces are created in the LSMO-CeO_2 nanodumbbell structure via a sequential growth of two different VAN compositions in a multilayer fashion. The tilted interfaces exhibit quite different lattice coupling patterns from the vertical couterparts. The nanodumbbell structure enables highly enhanced magnetic and magnetoresistance performances above room temperature compared with its VAN parent films. Inspired by the vertical architecture and coaxial growth of the nanodumbbell structure, strain-driven nucleation and growth mechanism is further demonstrated by a self-assembled 3D LSMO-CeO_2 framework showing fine vertical pillar registration and alignment.

VAN and its advanced architectures provide a broad playground for scientists and engineers to explore much deeper potentials within well-known materials, and benefit the next generation of functional devices in a wide range of applications, such as electrical, magnetic, optical, mechanical, catalytic, and energy-related systems. More efforts can be devoted to the following aspects:

(1) Ordered growth of the VAN thin films—not only the one achieved with application of external masks or templates and also the spontaneously ordered VAN structures. The ordered VAN growth shows considerable significance in materials design and process. The geometric feature of ordered VAN films can be controlled at microscale and nanoscale, which is quite significant and

helpful to the development of the modern functional devices, such as microelectronic device integration.

(2) This thesis mainly focus on the new microstructure and 3D strain engineering in LSMO-based VAN films and the physical properties. Those interesting VAN microstructure designs can be widely applied to other composite systems, not only the oxide-oxide systems and also a much broader spectrum of other materials systems such as nitride-oxide, oxide-metal, two-dimensional materials system, and even 3-phase composite systems. The physical property investigations of the interesting VAN designs can also be extended to other magnetic, electric, optical, catalytic, mechanical and energy-related applications.

(3) The VAN designs of 3D strain engineering could be used as the templates for small devices with special requirements, since their geometric feature is extraordinarily small (below ~10 nm). For example, the 2 phases in VAN microstructure can be selectively etched and the remaining phase has a densely porous architecture.

(4) The interesting designs studied in this thesis can be applied on various substrates, such as glass and flexible substrates. Moreover, since they contain 3D interconnected heterointerfaces within the films, the 3D framework microstructures can be applied in the free-standing thin film assembly for advanced electronic devices.

(5) The strain-driven growth mechanism deserves further investigations, although it has been demonstrated in the nanodumbbell structure. For example, which one is more dominant between the strain-driven and chemistry-driven growth mechanisms?

REFERENCES

[1] S.A. Chambers, Epitaxial Growth and Properties of Doped Transition Metal and Complex Oxide Films, Adv Mater 22(2) (2010) 219-248.

[2] U. Luders, A. Barthelemy, M. Bibes, K. Bouzehouane, S. Fusil, E. Jacquet, J.P. Contour, J.F. Bobo, J. Fontcuberta, A. Fert, NiFe2O4: A versatile spinel material brings new opportunities for spintronics, Adv Mater 18(13) (2006) 1733-+.

[3] L.W. Martin, Y.H. Chu, R. Ramesh, Advances in the growth and characterization of magnetic, ferroelectric, and multiferroic oxide thin films, Mat Sci Eng R 68(4-6) (2010) Iii-133.

[4] D.G. Schlom, L.-Q. Chen, X. Pan, A. Schmehl, M.A. Zurbuchen, A Thin Film Approach to Engineering Functionality into Oxides, Journal of the American Ceramic Society 91(8) (2008) 2429-2454.

[5] H.U. Habermeier, Thin films of perovskite-type complex oxides, Mater Today 10(10) (2007) 34-43.

[6] Q. Zhao, Z.H. Yan, C.C. Chen, J. Chen, Spinels: Controlled Preparation, Oxygen Reduction/Evolution Reaction Application, and Beyond, Chem Rev 117(15) (2017) 10121-10211.

[7] H. Zheng, J. Wang, S.E. Lofland, Z. Ma, L. Mohaddes-Ardabili, T. Zhao, L. Salamanca-Riba, S.R. Shinde, S.B. Ogale, F. Bai, D. Viehland, Y. Jia, D.G. Schlom, M. Wuttig, A. Roytburd, R. Ramesh, Multiferroic BaTiO3-CoFe2O4 nanostructures, Science 303(5658) (2004) 661-663.

[8] J.M. Rondinelli, S.J. May, J.W. Freeland, Control of octahedral connectivity in perovskite oxide heterostructures: An emerging route to multifunctional materials discovery, Mrs Bull 37(3) (2012) 261-270.

[9] J.H. Haeni, P. Irvin, W. Chang, R. Uecker, P. Reiche, Y.L. Li, S. Choudhury, W. Tian, M.E. Hawley, B. Craigo, A.K. Tagantsev, X.Q. Pan, S.K. Streiffer, L.Q. Chen, S.W. Kirchoefer, J. Levy, D.G. Schlom, Room-temperature ferroelectricity in strained SrTiO3, Nature 430(7001) (2004) 758-761.

[10] H. Yamada, Y. Ogawa, Y. Ishii, H. Sato, M. Kawasaki, H. Akoh, Y. Tokura, Engineered interface of magnetic oxides, Science 305(5684) (2004) 646-648.

[11] M.A. Pena, J.L.G. Fierro, Chemical structures and performance of perovskite oxides, Chem Rev 101(7) (2001) 1981-2017.

[12] F. Sanchez, C. Ocal, J. Fontcuberta, Tailored surfaces of perovskite oxide substrates for conducted growth of thin films, Chemical Society Reviews 43(7) (2014) 2272-2285.

[13] J. Ma, J.M. Hu, Z. Li, C.W. Nan, Recent Progress in Multiferroic Magnetoelectric Composites: from Bulk to Thin Films, Adv Mater 23(9) (2011) 1062-1087.

[14] W. Prellier, M.P. Singh, P. Murugavel, The single-phase multiferroic oxides: from bulk to thin film, J Phys-Condens Mat 17(30) (2005) R803-R832.

[15] J. Wang, J.B. Neaton, H. Zheng, V. Nagarajan, S.B. Ogale, B. Liu, D. Viehland, V. Vaithyanathan, D.G. Schlom, U.V. Waghmare, N.A. Spaldin, K.M. Rabe, M. Wuttig, R. Ramesh, Epitaxial BiFeO3 multiferroic thin film heterostructures, Science 299(5613) (2003) 1719-1722.

[16] W.A. Dunlap-Shohl, Y.Y. Zhou, N.P. Padture, D.B. Mitzi, Synthetic Approaches for Halide Perovskite Thin Films, Chem Rev 119(5) (2019) 3193-3295.

[17] J. Hwang, Z. Feng, N. Charles, X.R. Wang, D. Lee, K.A. Stoerzinger, S. Muy, R.R. Rao, D. Lee, R. Jacobs, D. Morgan, Y. Shao-Horn, Tuning perovskite oxides by strain: Electronic structure, properties, and functions in (electro)catalysis and ferroelectricity, Mater Today (2019).

[18] J.J. Huang, L.G. Li, P. Lu, Z.M. Qi, X. Sun, X.H. Zhang, H.Y. Wang, Self-assembled Co-BaZrO3 nanocomposite thin films with ultra-fine vertically aligned Co nanopillars, Nanoscale 9(23) (2017) 7970-7976.
[19] N. Kaiser, Review of the fundamentals of thin-film growth, Appl Optics 41(16) (2002) 3053-3060.
[20] I. Vrejoiu, M. Alexe, D. Hesse, U. Gosele, Functional Perovskites - From Epitaxial Films to Nanostructured Arrays, Adv Funct Mater 18(24) (2008) 3892-3906.
[21] H.Y. Hwang, Y. Iwasa, M. Kawasaki, B. Keimer, N. Nagaosa, Y. Tokura, Emergent phenomena at oxide interfaces, Nat Mater 11(2) (2012) 103-113.
[22] R. Aso, D. Kan, Y. Shimakawa, H. Kurata, Atomic level observation of octahedral distortions at the perovskite oxide heterointerface, Sci Rep-Uk 3 (2013).
[23] P. Yu, Y.H. Chu, R. Ramesh, Oxide interfaces: pathways to novel phenomena, Materials Today 15(7-8) (2012) 320-327.
[24] J.M. Rondinelli, N.A. Spaldin, Structure and Properties of Functional Oxide Thin Films: Insights From Electronic-Structure Calculations, Adv Mater 23(30) (2011) 3363-3381.
[25] (!!! INVALID CITATION !!! [25]).
[26] R. Ramesh, N.A. Spaldin, Multiferroics: progress and prospects in thin films, Nat Mater 6(1) (2007) 21-29.
[27] T. Miyazaki, N. Tezuka, Giant Magnetic Tunneling Effect in Fe/Al2o3/Fe Junction, J Magn Magn Mater 139(3) (1995) L231-L234.
[28] S.S.P. Parkin, C. Kaiser, A. Panchula, P.M. Rice, B. Hughes, M. Samant, S.H. Yang, Giant tunnelling magnetoresistance at room temperature with MgO (100) tunnel barriers, Nat Mater 3(12) (2004) 862-867.
[29] S. Yuasa, T. Nagahama, A. Fukushima, Y. Suzuki, K. Ando, Giant room-temperature magnetoresistance in single-crystal Fe/MgO/Fe magnetic tunnel junctions, Nat Mater 3(12) (2004) 868-871.
[30] M.N. Baibich, J.M. Broto, A. Fert, F.N. Vandau, F. Petroff, P. Eitenne, G. Creuzet, A. Friederich, J. Chazelas, Giant Magnetoresistance of (001)Fe/(001) Cr Magnetic Superlattices, Phys Rev Lett 61(21) (1988) 2472-2475.
[31] A.P. Chen, Z.X. Bi, C.F. Tsai, J. Lee, Q. Su, X.H. Zhang, Q.X. Jia, J.L. MacManus-Driscoll, H.Y. Wang, Tunable Low-Field Magnetoresistance in (La0.7Sr0.3MnO3)(0.5):(ZnO)(0.5) Self-Assembled Vertically Aligned Nanocomposite Thin Films, Adv Funct Mater 21(13) (2011) 2423-2429.
[32] I. Bakonyi, L. Peter, Electrodeposited multilayer films with giant magnetoresistance (GMR): Progress and problems, Prog Mater Sci 55(3) (2010) 107-245.
[33] H. Kuru, H. Kockar, M. Alper, Giant magnetoresistance (GMR) behavior of electrodeposited NiFe/Cu multilayers: Dependence of non-magnetic and magnetic layer thicknesses, J Magn Magn Mater 444 (2017) 132-139.
[34] L. Piraux, J.M. George, J.F. Despres, C. Leroy, E. Ferain, R. Legras, K. Ounadjela, A. Fert, Giant Magnetoresistance in Magnetic Multilayered Nanowires, Appl Phys Lett 65(19) (1994) 2484-2486.
[35] J. Mathon, A. Umerski, Theory of tunneling magnetoresistance of an epitaxial Fe/MgO/Fe(001) junction, Phys Rev B 63(22) (2001).
[36] A.M. Haghiri-Gosnet, J.P. Renard, CMR manganites: physics, thin films and devices, J Phys D Appl Phys 36(8) (2003) R127-R150.
[37] I. Robinson, R. Harder, Coherent X-ray diffraction imaging of strain at the nanoscale, Nat Mater 8(4) (2009) 291-298.

[38] A. Herklotz, A.T. Wong, T. Meyer, M.D. Biegalski, H.N. Lee, T.Z. Ward, Controlling Octahedral Rotations in a Perovskite via Strain Doping, Sci Rep-Uk 6 (2016).
[39] M.A. Bissett, M. Tsuji, H. Ago, Strain engineering the properties of graphene and other two-dimensional crystals, Phys Chem Chem Phys 16(23) (2014) 11124-11138.
[40] D.G. Schlom, L.Q. Chen, C.J. Fennie, V. Gopalan, D.A. Muller, X.Q. Pan, R. Ramesh, R. Uecker, Elastic strain engineering of ferroic oxides, Mrs Bull 39(2) (2014) 118-130.
[41] C. Si, Z.M. Sun, F. Liu, Strain engineering of graphene: a review, Nanoscale 8(6) (2016) 3207-3217.
[42] H.W. Guo, S. Dong, P.D. Rack, J.D. Budai, C. Beekman, Z. Gai, W. Siemons, C.M. Gonzalez, R. Timilsina, A.T. Wong, A. Herklotz, P.C. Snijders, E. Dagotto, T.Z. Ward, Strain Doping: Reversible Single-Axis Control of a Complex Oxide Lattice via Helium Implantation, Phys Rev Lett 114(25) (2015).
[43] A. Castellanos-Gomez, R. Roldan, E. Cappelluti, M. Buscema, F. Guinea, H.S.J. van der Zant, G.A. Steele, Local Strain Engineering in Atomically Thin MoS2, Nano Lett 13(11) (2013) 5361-5366.
[44] J. Li, Z.W. Shan, E. Ma, Elastic strain engineering for unprecedented materials properties, Mrs Bull 39(2) (2014) 108-117.
[45] R. Mbatang, D.Q. Xue, E. Enriquez, R.H. Yuan, H. Han, P. Dowden, Q. Wang, E. Fohtung, D.Z. Xue, T. Lookman, S.J. Pennycook, A.P. Chen, Enhanced magnetism in lightly doped manganite heterostructures: strain or stoichiometry?, Nanoscale 11(15) (2019) 7364-7370.
[46] S.Y. Yang, D. Prendergast, J.B. Neaton, Strain-Induced Band Gap Modification in Coherent Core/Shell Nanostructures, Nano Lett 10(8) (2010) 3156-3162.
[47] S.A. Dayeh, W. Tang, F. Boioli, K.L. Kavanagh, H. Zheng, J. Wang, N.H. Mack, G. Swadener, J.Y. Huang, L. Miglio, K.N. Tu, S.T. Picraux, Direct Measurement of Coherency Limits for Strain Relaxation in Heteroepitaxial Core/Shell Nanowires, Nano Lett 13(5) (2013) 1869-1876.
[48] D.G. Schlom, L.Q. Chen, C.B. Eom, K.M. Rabe, S.K. Streiffer, J.M. Triscone, Strain tuning of ferroelectric thin films, Annu Rev Mater Res 37 (2007) 589-626.
[49] D. Fuchs, E. Arac, C. Pinta, S. Schuppler, R. Schneider, H.V. von Lohneysen, Tuning the magnetic properties of LaCoO3 thin films by epitaxial strain, Phys Rev B 77(1) (2008).
[50] A.P. Chen, Z.X. Bi, H. Hazariwala, X.H. Zhang, Q. Su, L. Chen, Q.X. Jia, J.L. MacManus-Driscoll, H.Y. Wang, Microstructure, magnetic, and low-field magnetotransport properties of self-assembled (La0.7Sr0.3MnO3)(0.5):(CeO2)(0.5) vertically aligned nanocomposite thin films, Nanotechnology 22(31) (2011).
[51] M.R. Bayati, R. Molaei, R.J. Narayan, J. Narayan, H. Zhou, S.J. Pennycook, Domain epitaxy in TiO2/alpha-Al2O3 thin film heterostructures with Ti2O3 transient layer, Appl Phys Lett 100(25) (2012).
[52] A. Chen, Q. Su, H. Han, E. Enriquez, Q. Jia, Metal Oxide Nanocomposites: A Perspective from Strain, Defect, and Interface, Adv Mater 0(0) 1803241.
[53] K.J. Choi, M. Biegalski, Y.L. Li, A. Sharan, J. Schubert, R. Uecker, P. Reiche, Y.B. Chen, X.Q. Pan, V. Gopalan, L.Q. Chen, D.G. Schlom, C.B. Eom, Enhancement of ferroelectricity in strained BaTiO3 thin films, Science 306(5698) (2004) 1005-1009.
[54] W.R. Zhang, R. Ramesh, J.L. MacManus-Driscoll, H.Y. Wang, Multifunctional, self-assembled oxide nanocomposite thin films and devices, Mrs Bull 40(9) (2015) 736-745.
[55] H. Yang, Z.E. Cao, X. Shen, T. Xian, W.J. Feng, J.L. Jiang, Y.C. Feng, Z.Q. Wei, J.F. Dai, Fabrication of 0-3 type manganite/insulator composites and manipulation of their magnetotransport properties, J Appl Phys 106(10) (2009).

[56] A. Llordes, A. Palau, J. Gazquez, M. Coll, R. Vlad, A. Pomar, J. Arbiol, R. Guzman, S. Ye, V. Rouco, F. Sandiumenge, S. Ricart, T. Puig, M. Varela, D. Chateigner, J. Vanacken, J. Gutierrez, V. Moshchalkov, G. Deutscher, C. Magen, X. Obradors, Nanoscale strain-induced pair suppression as a vortex-pinning mechanism in high-temperature superconductors, Nat Mater 11(4) (2012) 329-336.

[57] D. Mukherjee, N. Bingham, M. Hordagoda, M.H. Phan, H. Srikanth, S. Witanachchi, P. Mukherjee, Influence of microstructure and interfacial strain on the magnetic properties of epitaxial Mn3O4/La0.7Sr0.3MnO3 layered-composite thin films, J Appl Phys 112(8) (2012).

[58] A.P. Chen, F. Khatkhatay, W. Zhang, C. Jacob, L. Jiao, H. Wang, Strong oxygen pressure dependence of ferroelectricity in BaTiO3/SrRuO3/SrTiO3 epitaxial heterostructures, J Appl Phys 114(12) (2013).

[59] O.I. Lebedev, J. Verbeeck, G. Van Tendeloo, O. Shapoval, A. Belenchuk, V. Moshnyaga, B. Damashcke, K. Samwer, Structural phase transitions and stress accommodation in (La0.67Ca0.33MnO3)(1-x):(MgO)(x) composite films, Phys Rev B 66(10) (2002).

[60] V. Moshnyaga, B. Damaschke, O. Shapoval, A. Belenchuk, J. Faupel, O.I. Lebedev, J. Verbeeck, G. Van Tendeloo, M. Mucksch, V. Tsurkan, R. Tidecks, K. Samwer, Structural phase transition at the percolation threshold in epitaxial (La0.7Ca0.3MnO3)(1-X):(MgO)(X) nanocomposite films, Nat Mater 2(4) (2003) 247-252.

[61] W.R. Zhang, A.P. Chen, Z.K. Bi, Q.X. Jia, J.L. MacManus-Driscoll, H.Y. Wang, Interfacial coupling in heteroepitaxial vertically aligned nanocomposite thin films: From lateral to vertical control, Curr Opin Solid St M 18(1) (2014) 6-18.

[62] N. Dix, R. Muralidharan, J.M. Rebled, S. Estrade, F. Peiro, M. Varela, J. Fontcuberta, F. Sanchez, Selectable Spontaneous Polarization Direction and Magnetic Anisotropy in BiFeO3-CoFe2O4 Epitaxial Nanostructures, Acs Nano 4(8) (2010) 4955-4961.

[63] J.L. MacManus-Driscoll, Self-Assembled Heteroepitaxial Oxide Nanocomposite Thin Film Structures: Designing Interface-Induced Functionality in Electronic Materials, Adv Funct Mater 20(13) (2010) 2035-2045.

[64] A.P. Chen, Z.X. Bi, Q.X. Jia, J.L. MacManus-Driscoll, H.Y. Wang, Microstructure, vertical strain control and tunable functionalities in self-assembled, vertically aligned nanocomposite thin films, Acta Mater 61(8) (2013) 2783-2792.

[65] X.K. Ning, Z.J. Wang, Z.D. Zhang, Controllable Self-Assembled Microstructures of La0.7Ca0.3MnO3:NiO Nanocomposite Thin Films and Their Tunable Functional Properties, Adv Mater Interfaces 2(15) (2015).

[66] D. Fuks, S. Dorfman, S. Piskunov, E.A. Kotomin, Ab initio thermodynamics of BacSr(1-c)TiO3 solid solutions, Phys Rev B 71(1) (2005).

[67] S. Park, Y. Horibe, T. Asada, L.S. Wielunski, N. Lee, P.L. Bonanno, S.M. O'Malley, A.A. Sirenko, A. Kazimirov, M. Tanimura, T. Gustafsson, S.W. Cheong, Highly aligned epitaxial nanorods with a checkerboard pattern in oxide films, Nano Lett 8(2) (2008) 720-724.

[68] J.L. MaCmanus-Driscoll, P. Zerrer, H.Y. Wang, H. Yang, J. Yoon, A. Fouchet, R. Yu, M.G. Blamire, Q.X. Jia, Strain control and spontaneous phase ordering in vertical nanocomposite heteroepitaxial thin films, Nat Mater 7(4) (2008) 314-320.

[69] S.C. Liao, P.Y. Tsai, C.W. Liang, H.J. Liu, J.C. Yang, S.J. Lin, C.H. Lai, Y.H. Chu, Misorientation Control and Functionality Design of Nanopillars in Self-Assembled Perovskite-Spinel Heteroepitaxial Nanostructures, Acs Nano 5(5) (2011) 4118-4122.

[70] H.M. Zheng, F. Straub, Q. Zhan, P.L. Yang, W.K. Hsieh, F. Zavaliche, Y.H. Chu, U. Dahmen, R. Ramesh, Self-assembled growth of BiFeO3-CoFe2O4 nanostructures, Adv Mater 18(20) (2006) 2747-+.
[71] Z.G. Wang, Y.X. Li, R. Viswan, B.L. Hu, V.G. Harris, J.F. Li, D. Viehland, Engineered Magnetic Shape Anisotropy in BiFeO3-CoFe2O4 Self-Assembled Thin Films, Acs Nano 7(4) (2013) 3447-3456.
[72] H. Zheng, Q. Zhan, F. Zavaliche, M. Sherburne, F. Straub, M.P. Cruz, L.Q. Chen, U. Dahmen, R. Ramesh, Controlling self-assembled perovskite-spinel nanostructures, Nano Lett 6(7) (2006) 1401-1407.
[73] I. Levin, J.H. Li, J. Slutsker, A.L. Roytburd, Design of self-assembled multiferroic nanostructures in epitaxial films, Adv Mater 18(15) (2006) 2044-+.
[74] Y.S. Kim, J. Song, C. Hwang, X. Wang, H. Wang, J.L. MacManus-Driscoll, H.K. Song, S. Cho, Nanoporous Films and Nanostructure Arrays Created by Selective Dissolution of Water-Soluble Materials, Adv Sci 5(11) (2018).
[75] W.R. Zhang, A.P. Chen, F. Khatkhatay, C.F. Tsai, Q. Su, L. Jiao, X.H. Zhang, H.Y. Wang, Integration of Self-Assembled Vertically Aligned Nanocomposite (La0.7Sr0.3MnO3)(1-x):(ZnO)(x) Thin Films on Silicon Substrates, Acs Appl Mater Inter 5(10) (2013) 3995-3999.
[76] F. Khatkhatay, A.P. Chen, J.H. Lee, W.R. Zhang, H. Abdel-Raziq, H.Y. Wang, Ferroelectric Properties of Vertically Aligned Nanostructured BaTiO3-CeO2 Thin Films and Their Integration on Silicon, Acs Appl Mater Inter 5(23) (2013) 12541-12547.
[77] M. Fan, W.R. Zhang, F. Khatkhatay, L.G. Li, H.Y. Wang, Enhanced tunable magnetoresistance properties over a wide temperature range in epitaxial (La0.7Sr0.3MnO3)(1-x):(CeO2)(x) nanocomposites, J Appl Phys 118(6) (2015).
[78] R. Zhao, W.W. Li, J.H. Lee, E.M. Choi, Y. Liang, W. Zhang, R.J. Tang, H.Y. Wang, Q.X. Jia, J.L. MacManus-Driscoll, H. Yang, Precise Tuning of (YBa2Cu3O7-delta)(1-x):(BaZrO3)(x) Thin Film Nanocomposite Structures, Adv Funct Mater 24(33) (2014) 5240-5245.
[79] A.P. Chen, M. Weigand, Z.X. Bi, W.R. Zhang, X.J. Lu, P. Dowden, J.L. MacManus-Driscoll, H.Y. Wang, Q.X. Jia, Evolution of microstructure, strain and physical properties in oxide nanocomposite films, Sci Rep-Uk 4 (2014).
[80] W.R. Zhang, A.P. Chen, J. Jian, Y.Y. Zhu, L. Chen, P. Lu, Q.X. Jia, J.L. MacManus-Driscoll, X.H. Zhang, H.Y. Wang, Strong perpendicular exchange bias in epitaxial La0.7Sr0.3MnO3:BiFeO3 nanocomposite films through vertical interfacial coupling, Nanoscale 7(33) (2015) 13808-13815.
[81] W.R. Zhang, L.G. Li, P. Lu, M. Fan, Q. Su, F. Khatkhatay, A.P. Chen, Q.X. Jia, X.H. Zhang, J.L. MacManus-Driscoll, H.Y. Wang, Perpendicular Exchange-Biased Magnetotransport at the Vertical Heterointerfaces in La0.7Sr0.3MnO3:NiO Nanocomposites, Acs Appl Mater Inter 7(39) (2015) 21646-21651.
[82] D. Dijkkamp, T. Venkatesan, X.D. Wu, S.A. Shaheen, N. Jisrawi, Y.H. Minlee, W.L. Mclean, M. Croft, Preparation of Y-Ba-Cu Oxide Superconductor Thin-Films Using Pulsed Laser Evaporation from High-Tc Bulk Material, Appl Phys Lett 51(8) (1987) 619-621.
[83] H.S. Kwok, J.P. Zheng, S. Witanachchi, P. Mattocks, L. Shi, Q.Y. Ying, X.W. Wang, D.T. Shaw, Growth of Highly Oriented Cds Thin-Films by Laser-Evaporation Deposition, Appl Phys Lett 52(13) (1988) 1095-1097.
[84] R.K. Singh, J. Narayan, Pulsed-Laser Evaporation Technique for Deposition of Thin-Films - Physics and Theoretical-Model, Phys Rev B 41(13) (1990) 8843-8859.

[85] S.R.C. McMitchell, Research Update: New possibilities for the nanoscale engineering of complex oxide thin films, Apl Mater 3(6) (2015).
[86] M.S. Tillack, D.W. Blair, S.S. Harilal, The effect of ionization on cluster formation in laser ablation plumes, Nanotechnology 15(3) (2004) 390-403.
[87] M.N.R. Ashfold, F. Claeyssens, G.M. Fuge, S.J. Henley, Pulsed laser ablation and deposition of thin films, Chem Soc Rev 33(1) (2004) 23-31.
[88] M.G. Blamire, J.L. MacManus-Driscoll, N.D. Mathur, Z.H. Barber, The Materials Science of Functional Oxide Thin Films, Adv Mater 21(38-39) (2009) 3827-3839.
[89] M.A. Moram, M.E. Vickers, X-ray diffraction of III-nitrides, Rep Prog Phys 72(3) (2009).
[90] X. Zhu, R. Birringer, U. Herr, H. Gleiter, X-Ray-Diffraction Studies of the Structure of Nanometer-Sized Crystalline Materials, Phys Rev B 35(17) (1987) 9085-9090.
[91] A.K. Zak, W.H.A. Majid, M.E. Abrishami, R. Yousefi, X-ray analysis of ZnO nanoparticles by Williamson-Hall and size-strain plot methods, Solid State Sci 13(1) (2011) 251-256.
[92] L.L. Fan, S. Chen, Z.L. Luo, Q.H. Liu, Y.F. Wu, L. Song, D.X. Ji, P. Wang, W.S. Chu, C. Gao, C.W. Zou, Z.Y. Wu, Strain Dynamics of Ultrathin VO2 Film Grown on TiO2 (001) and the Associated Phase Transition Modulation, Nano Lett 14(7) (2014) 4036-4043.
[93] S. Pereira, M.R. Correia, E. Pereira, K.P. O'Donnell, E. Alves, A.D. Sequeira, N. Franco, I.M. Watson, C.J. Deatcher, Strain and composition distributions in wurtzite InGaN/GaN layers extracted from x-ray reciprocal space mapping, Appl Phys Lett 80(21) (2002) 3913-3915.
[94] Q. Wang, J. Bai, Y.P. Gong, T. Wang, Influence of strain relaxation on the optical properties of InGaN/GaN multiple quantum well nanorods, J Phys D Appl Phys 44(39) (2011).
[95] Z.L. Wang, Transmission electron microscopy of shape-controlled nanocrystals and their assemblies, J Phys Chem B 104(6) (2000) 1153-1175.
[96] Y.Y. Zhu, C. Ophus, J. Ciston, H.Y. Wang, Interface lattice displacement measurement to 1 pm by geometric phase analysis on aberration-corrected HAADF STEM images, Acta Mater 61(15) (2013) 5646-5663.
[97] Y. Lu, X.W. Li, G.Q. Gong, G. Xiao, A. Gupta, P. Lecoeur, J.Z. Sun, Y.Y. Wang, V.P. Dravid, Large magnetotunneling effect at low magnetic fields in micrometer-scale epitaxial La0.67Sr.033MnO3 tunnel junctions, Phys Rev B 54(12) (1996) R8357-R8360.
[98] A.S. Bhalla, R.Y. Guo, R. Roy, The perovskite structure - a review of its role in ceramic science and technology, Mater Res Innov 4(1) (2000) 3-26.
[99] J. Junquera, P. Ghosez, Critical thickness for ferroelectricity in perovskite ultrathin films, Nature 422(6931) (2003) 506-509.
[100] S. Jin, T.H. Tiefel, M. Mccormack, R.A. Fastnacht, R. Ramesh, L.H. Chen, Thousandfold Change in Resistivity in Magnetoresistive La-Ca-Mn-O Films, Science 264(5157) (1994) 413-415.
[101] Y. Moritomo, A. Asamitsu, H. Kuwahara, Y. Tokura, Giant magnetoresistance of manganese oxides with a layered perovskite structure, Nature 380(6570) (1996) 141-144.
[102] E. Dagotto, T. Hotta, A. Moreo, Colossal magnetoresistant materials: The key role of phase separation, Phys Rep 344(1-3) (2001) 1-153.
[103] Y. Maeno, H. Hashimoto, K. Yoshida, S. Nishizaki, T. Fujita, J.G. Bednorz, F. Lichtenberg, Superconductivity in a Layered Perovskite without Copper, Nature 372(6506) (1994) 532-534.
[104] H.Y. Hwang, S.W. Cheong, N.P. Ong, B. Batlogg, Spin-Polarized Intergrain Tunneling in $La_{2/3}Sr_{1/3}MnO_3$, Phys Rev Lett 77(10) (1996) 2041-2044.
[105] M. Uehara, S. Mori, C.H. Chen, S.W. Cheong, Percolative phase separation underlies colossal magnetoresistance in mixed-valent manganites, Nature 399(6736) (1999) 560-563.

[106] J.M. Rondinelli, S.J. May, J.W. Freeland, Control of octahedral connectivity in perovskite oxide heterostructures: An emerging route to multifunctional materials discovery, Mrs Bull 37(03) (2012) 261-270.
[107] A. Chen, J.-M. Hu, P. Lu, T. Yang, W. Zhang, L. Li, T. Ahmed, E. Enriquez, M. Weigand, Q. Su, H. Wang, J.-X. Zhu, J.L. MacManus-Driscoll, L.-Q. Chen, D. Yarotski, Q. Jia, Role of scaffold network in controlling strain and functionalities of nanocomposite films, Science Advances 2(6) (2016).
[108] S.A. Harrington, J.Y. Zhai, S. Denev, V. Gopalan, H.Y. Wang, Z.X. Bi, S.A.T. Redfern, S.H. Baek, C.W. Bark, C.B. Eom, Q.X. Jia, M.E. Vickers, J.L. MacManus-Driscoll, Thick lead-free ferroelectric films with high Curie temperatures through nanocomposite-induced strain, Nat Nanotechnol 6(8) (2011) 491-495.
[109] V. Moshnyaga, B. Damaschke, O. Shapoval, A. Belenchuk, J. Faupel, O.I. Lebedev, J. Verbeeck, G. van Tendeloo, M. Mucksch, V. Tsurkan, R. Tidecks, K. Samwer, Structural phase transition at the percolation threshold in epitaxial (La0.7Ca0.3MnO3)1-x:(MgO)x nanocomposite films, Nat Mater 2(4) (2003) 247-252.
[110] W. Zhang, A. Chen, Z. Bi, Q. Jia, J.L. MacManus-Driscoll, H. Wang, Interfacial coupling in heteroepitaxial vertically aligned nanocomposite thin films: From lateral to vertical control, Current Opinion in Solid State and Materials Science 18(1) (2014) 6-18.
[111] J. Huang, J.L. MacManus-Driscoll, H. Wang, New epitaxy paradigm in epitaxial self-assembled oxide vertically aligned nanocomposite thin films, J Mater Res (2017) 1-13.
[112] M. Fan, B. Zhang, H. Wang, J. Jian, X. Sun, J. Huang, L. Li, X. Zhang, H. Wang, Self-Organized Epitaxial Vertically Aligned Nanocomposites with Long-Range Ordering Enabled by Substrate Nanotemplating, Adv Mater (2017) 1606861-n/a.
[113] H. Yang, Z.E. Cao, X. Shen, T. Xian, W.J. Feng, J.L. Jiang, Y.C. Feng, Z.Q. Wei, J.F. Dai, Fabrication of 0-3 type manganite/insulator composites and manipulation of their magnetotransport properties, J Appl Phys 106(10) (2009) 104317.
[114] J.C. Yang, H.J. Liu, Y.H. Chu, Mesocrystal-embedded functional oxide systems, Mrs Commun 6(3) (2016) 167-181.
[115] S. Lee, J.L. MacManus-Driscoll, Research Update: Fast and tunable nanoionics in vertically aligned nanostructured films, Apl Materials 5(4) (2017).
[116] X. Sun, Q. Li, J.C. Jiang, Y.B. Mao, Morphology-tunable synthesis of ZnO nanoforest and its photoelectrochemical performance, Nanoscale 6(15) (2014) 8769-8780.
[117] X. Sun, Q. Li, Y.N. Lu, Y.B. Mao, Three-dimensional ZnO@MnO2 core@shell nanostructures for electrochemical energy storage, Chem Commun 49(40) (2013) 4456-4458.
[118] Z.N. Yu, L. Tetard, L. Zhai, J. Thomas, Supercapacitor electrode materials: nanostructures from 0 to 3 dimensions, Energ Environ Sci 8(3) (2015) 702-730.
[119] C.W. Cheng, H.J. Fan, Branched nanowires: Synthesis and energy applications, Nano Today 7(4) (2012) 327-343.
[120] Y.C. Qiu, K.Y. Yan, H. Deng, S.H. Yang, Secondary Branching and Nitrogen Doping of ZnO Nanotetrapods: Building a Highly Active Network for Photoelectrochemical Water Splitting, Nano Lett 12(1) (2012) 407-413.
[121] M. Fan, W.R. Zhang, F. Khatkhatay, L.G. Li, H.Y. Wang, Enhanced tunable magnetoresistance properties over a wide temperature range in epitaxial (La0.7Sr0.3MnO3)(1-x):(CeO2)(x) nanocomposites, J Appl Phys 118(6) (2015) 6.

[122] X.K. Ning, Z.J. Wang, Z.D. Zhang, Large, Temperature-Tunable Low-Field Magnetoresistance in La0.7Sr0.3MnO3:NiO Nanocomposite Films Modulated by Microstructures, Adv Funct Mater 24(34) (2014) 5393-5401.
[123] A.P. Chen, Z.X. Bi, H. Hazariwala, X.H. Zhang, Q. Su, L. Chen, Q.X. Jia, J.L. MacManus-Driscoll, H.Y. Wang, Microstructure, magnetic, and low-field magnetotransport properties of self-assembled (La0.7Sr0.3MnO3)(0.5):(CeO2)(0.5) vertically aligned nanocomposite thin films, Nanotechnology 22(31) (2011) 6.
[124] O.I. Lebedev, J. Verbeeck, G. Van Tendeloo, O. Shapoval, A. Belenchuk, V. Moshnyaga, B. Damashcke, K. Samwer, Structural phase transitions and stress accommodation in $(La_{0.67}Ca_{0.33}MnO_3)_{1-x}$:$(MgO)_x$ composite films, Phys Rev B 66(10) (2002) 104421.
[125] K.H. Ahn, T. Lookman, A.R. Bishop, Strain-induced metal-insulator phase coexistence in perovskite manganites, Nature 428(6981) (2004) 401-404.
[126] A.J. Millis, Lattice effects in magnetoresistive manganese perovskites, Nature 392(6672) (1998) 147-150.
[127] S.A. Koster, V. Moshnyaga, K. Samwer, O.I. Lebedev, G. van Tendeloo, O. Shapoval, A. Belenchuk, Doping of interfaces in (La0.7Sr0.3MnO3)(1-x):(MgO)(x) composite films, Appl Phys Lett 81(9) (2002) 1648-1650.
[128] S.J. Zhu, J. Yuan, B.Y. Zhu, F.C. Zhang, B. Xu, L.X. Cao, X.G. Qiu, B.R. Zhao, P.X. Zhang, Exchange bias effect and enhanced magnetoresistance in La0.67Sr0.33MnO3/SrTiO3 superlattices, Appl Phys Lett 90(11) (2007).
[129] L. Li, X.Q. Zhang, L. Li, X.F. Zhai, C.G. Zeng, Magnetoresistance of single-crystalline La0.67Sr0.33MnO3/MgO nanorod arrays, Solid State Commun 171 (2013) 46-49.
[130] A.P. Chen, W.R. Zhang, J. Jian, H.Y. Wang, C.F. Tsai, Q. Su, Q.X. Jia, J.L. MacManus-Driscoll, Role of boundaries on low-field magnetotransport properties of La0.7Sr0.3MnO3-based nanocomposite thin films, J Mater Res 28(13) (2013) 1707-1714.
[131] C.H. Yan, Z.G. Xu, T. Zhu, Z.M. Wang, F.X. Cheng, Y.H. Huang, C.S. Liao, A large low field colossal magnetoresistance in the La0.7Sr0.3MnO3 and CoFe2O4 combined system, J Appl Phys 87(9) (2000) 5588-5590.
[132] M. Staruch, C. Cantoni, M. Jain, Systematic study of magnetotransport properties and enhanced low-field magnetoresistance in thin films of La0.67Sr0.33MnO3 + Mg(O), Appl Phys Lett 102(6) (2013).
[133] M. Staruch, H.Y. Gao, P.X. Gao, M. Jain, Low-Field Magnetoresistance in La0.67Sr0.33MnO3:ZnO Composite Film, Advanced Functional Materials 22(17) (2012) 3591-3595.
[134] B.S. Kang, H. Wang, J.L. MacManus-Driscoll, Y. Li, Q.X. Jia, I. Mihut, J.B. Betts, Low field magnetotransport properties of (La0.7Sr0.3MnO3)(0.5):(ZnO)(0.5) nanocomposite films, Appl Phys Lett 88(19) (2006).
[135] C. Kwon, Q.X. Jia, Y. Fan, M.F. Hundley, D.W. Reagor, J.Y. Coulter, D.E. Peterson, Large magnetoresistance in La0.7Sr0.3MnO3/SrTiO3/La0.7Sr0.3MnO3 ramp-edge junctions, Appl Phys Lett 72(4) (1998) 486-488.
[136] J. Li, Q. Huang, Z.W. Li, L.P. You, S.Y. Xu, C.K. Ong, Enhanced magnetoresistance in Ag-doped granular La2/3Sr1/3MnO3 thin films prepared by dual-beam pulsed-laser deposition, J Appl Phys 89(11) (2001) 7428-7430.
[137] S. Nazemi, M. Pourfath, E.A. Soleimani, H. Kosina, The effect of oxide shell thickness on the structural, electronic, and optical properties of Si-SiO2 core-shell nano-crystals: A (time dependent)density functional theory study, J Appl Phys 119(14) (2016).

[138] X. Sun, J.J. Huang, J. Jian, M. Fan, H. Wang, Q. Li, J.L. Mac Manus-Driscoll, P. Lu, X.H. Zhang, H.Y. Wang, Three-dimensional strain engineering in epitaxial vertically aligned nanocomposite thin films with tunable magnetotransport properties, Mater Horiz 5(3) (2018) 536-544.
[139] G. Panchal, D.K. Shukla, R.J. Choudhary, V.R. Reddy, D.M. Phase, The effect of oxygen stoichiometry at the interface of epitaxial BaTiO3/La0.7Sr0.3MnO3 bilayers on its electronic and magnetic properties, J Appl Phys 122(8) (2017).
[140] S.R. Singamaneni, W. Fan, J.T. Prater, J. Narayan, Magnetic properties of BaTiO3/La0.7Sr0.3MnO3 thin films integrated on Si(100), J Appl Phys 116(22) (2014).
[141] L. Yin, Q. Zhang, W.B. Mi, X.X. Wang, Strain-controlled interfacial magnetization and orbital splitting in La2/3Sr1/3MnO3/tetragonal BiFeO3 heterostructures, J Appl Phys 120(16) (2016).
[142] D. Barrionuevo, N. Ortega, A. Kumar, R. Chatterjee, J.F. Scott, R.S. Katiyar, Thickness dependent functional properties of PbZr0.52Ti0.48O3/La0.67Sr0.33MnO3 heterostructures, J Appl Phys 114(23) (2013).
[143] J.J. Huang, J.L. MacManus-Driscoll, H.Y. Wang, New epitaxy paradigm in epitaxial self-assembled oxide vertically aligned nanocomposite thin films, J Mater Res 32(21) (2017) 4054-4066.
[144] M. Fan, B. Zhang, H. Wang, J. Jian, X. Sun, J.J. Huang, L.G. Li, X.H. Zhang, H.Y. Wang, Self-Organized Epitaxial Vertically Aligned Nanocomposites with Long-Range Ordering Enabled by Substrate Nanotemplating, Adv Mater 29(23) (2017).
[145] S. Cho, C. Yun, S. Tappertzhofen, A. Kursumovic, S. Lee, P. Lu, Q.X. Jia, M. Fan, J. Jian, H.Y. Wang, S. Hofmann, J.L. MacManus-Driscoll, Self-assembled oxide films with tailored nanoscale ionic and electronic channels for controlled resistive switching, Nat Commun 7 (2016).
[146] A.P. Chen, J.M. Hu, P. Lu, T.N. Yang, W.R. Zhang, L.G. Li, T. Ahmed, E. Enriquez, M. Weigand, Q. Su, H.Y. Wang, J.X. Zhu, J.L. MacManus-Driscoll, L.Q. Chen, D. Yarotski, Q.X. Jia, Role of scaffold network in controlling strain and functionalities of nanocomposite films, Sci Adv 2(6) (2016).
[147] V. Moshnyaga, B. Damaschke, O. Shapoval, A. Belenchuk, J. Faupel, O.I. Lebedev, J. Verbeeck, G. Van Tendeloo, M. Mucksch, V. Tsurkan, R. Tidecks, K. Samwer, Structural phase transition at the percolation threshold in epitaxial (La0.7Ca0.3MnO3)(1-x):(MgO)(x) nanocomposite films (vol 2, pg 247, 2003), Nature Materials 4(1) (2005) 103-103.
[148] M. Fan, H. Wang, S. Misra, B. Zhang, Z.M. Qi, X. Sun, J.J. Huang, H.Y. Wang, Microstructure, Magnetic, and Magnetoresistance Properties of La0.7Sr0.3MnO3:CuO Nanocomposite Thin Films, Acs Appl Mater Inter 10(6) (2018) 5779-5784.
[149] Q. Li, X. Sun, K. Lozano, Y.B. Mao, Dependence of Photoelectrochemical Properties on Geometry Factors of Interconnected "Caterpillar-like" ZnO Networks, Electrochim Acta 222 (2016) 232-245.
[150] Q. Li, X. Sun, K. Lozano, Y.B. Mao, Facile and Scalable Synthesis of "Caterpillar-like" ZnO Nanostructures with Enhanced Photoelectrochemical Water-Splitting Effect, J Phys Chem C 118(25) (2014) 13467-13475.
[151] A.P. Chen, W.R. Zhang, F. Khatkhatay, Q. Su, C.F. Tsai, L. Chen, Q.X. Jia, J.L. MacManus-Driscoll, H. Wang, Magnetotransport properties of quasi-one-dimensionally channeled vertically aligned heteroepitaxial nanomazes (vol 102, 093114, 2013), Appl Phys Lett 104(6) (2014).
[152] Y. Zhu, A. Chen, H. Zhou, W. Zhang, J. Narayan, J.L. MacManus-Driscoll, Q. Jia, H. Wang, M.-D.J. L., F.S. R., J.Q. X., W. H., S. A., C. L., M. B., H.M. E., M.M. P., P.D. E., Research Updates: Epitaxial strain relaxation and associated interfacial reconstructions: The driving force for creating new structures with integrated functionality, APL Materials 1(5) (2013) 050702.

[153] X. Weng, M. Hennes, A. Coati, A. Vlad, Y. Garreau, M. Sauvage-Simkin, E. Fonda, G. Patriarche, D. Demaille, F. Vidal, Y. Zheng, Ultrathin Ni nanowires embedded in SrTiO3: Vertical epitaxy, strain relaxation mechanisms, and solid-state amorphization, Phys Rev Mater 2(10) (2018).
[154] J. MacManus-Driscoll, A. Suwardi, A. Kursumovic, Z.X. Bi, C.F. Tsai, H.Y. Wang, Q.X. Jia, O.J. Lee, New strain states and radical property tuning of metal oxides using a nanocomposite thin film approach, Apl Materials 3(6) (2015).
[155] V. Schuler, F.J. Bonilla, D. Demaille, A. Coati, A. Vlad, Y. Garreau, M. Sauvage-Simkin, A. Novikova, E. Fonda, S. Hidki, V. Etgens, F. Vidal, Y.L. Zheng, Huge metastable axial strain in ultrathin heteroepitaxial vertically aligned nanowires, Nano Res 8(6) (2015) 1964-1974.
[156] X. Sun, Q. Li, J. Huang, J. Jian, P. Lu, X. Zhang, J.L. MacManus-Driscoll, H. Wang, Strain and property tuning of the 3D framed epitaxial nanocomposite thin films via interlayer thickness variation, J Appl Phys 125(8) (2019) 082530.
[157] A. Chen, Z. Harrell, P. Lu, E. Enriquez, L. Li, B. Zhang, P. Dowden, C. Chen, H. Wang, J.L. MacManus-Driscoll, Q. Jia, Strain Enhanced Functionality in a Bottom-Up Approach Enabled 3D Super-Nanocomposites, Adv Funct Mater 0(0) 1900442.
[158] V. Garcia, M. Bibes, L. Bocher, S. Valencia, F. Kronast, A. Crassous, X. Moya, S. Enouz-Vedrenne, A. Gloter, D. Imhoff, C. Deranlot, N.D. Mathur, S. Fusil, K. Bouzehouane, A. Barthelemy, Ferroelectric Control of Spin Polarization, Science 327(5969) (2010) 1106-1110.
[159] Q. Su, D. Yoon, Z. Sisman, F. Khatkhatay, Q.X. Jia, A. Manthiram, H.Y. Wang, Vertically aligned nanocomposite La0.8Sr0.2MnO3-delta/Zr0.92Y0.08O1.96 thin films as electrode/electrolyte interfacial layer for solid oxide reversible fuel cells, Int J Hydrogen Energ 38(36) (2013) 16320-16327.
[160] Q. Su, D. Yoon, A.P. Chen, F. Khatkhatay, A. Manthiram, H.Y. Wang, Vertically aligned nanocomposite electrolytes with superior out-of-plane ionic conductivity for solid oxide fuel cells, J Power Sources 242 (2013) 455-463.
[161] A.P. Chen, Z.X. Bi, C.F. Tsai, L. Chen, Q. Su, X.H. Zhang, H.Y. Wang, Tilted Aligned Epitaxial La0.7Sr0.3MnO3 Nanocolumnar Films with Enhanced Low-Field Magnetoresistance by Pulsed Laser Oblique-Angle Deposition, Cryst Growth Des 11(12) (2011) 5405-5409.
[162] A. Gaur, G.D. Varma, Magnetoresistance behaviour of La0.7Sr0.3MnO3/NiO composites, Solid State Commun 139(6) (2006) 310-314.
[163] S. Karmakar, S. Taran, B.K. Chaudhuri, H. Sakata, C.P. Sun, C.L. Huang, H.D. Yang, Study of grain boundary contribution and enhancement of magnetoresistance in La0.67Ca0.33MnO3/V2O5 composites, J Phys D Appl Phys 38(20) (2005) 3757-3763.
[164] B.X. Huang, Y.H. Liu, R.Z. Zhang, Xiaobo-Yuan, C.J. Wang, L.M. Mei, Low-field MR behaviour in La0.67Ca0.33MnO3/ZrO2 composite system, J Phys D Appl Phys 36(16) (2003) 1923-1927.
[165] L.E. Hueso, J. Rivas, F. Rivadulla, M.A. Lopez-Quintela, Magnetoresistance in manganite/alumina nanocrystalline composites, J Appl Phys 89(3) (2001) 1746-1750.
[166] Z.X. Bi, E. Weal, H.M. Luo, A.P. Chen, J.L. MacManus-Driscoll, Q.X. Jia, H.Y. Wang, Microstructural and magnetic properties of (La0.7Sr0.3MnO3)(0.7):(Mn3O4)(0.3) nanocomposite thin films, J Appl Phys 109(5) (2011).
[167] J.M. De Teresa, A. Barthelemy, A. Fert, J.P. Contour, R. Lyonnet, F. Montaigne, P. Seneor, A. Vaures, Inverse tunnel magnetoresistance in Co/SrTiO3/La0.7Sr0.3MnO3: New ideas on spin-polarized tunneling, Phys Rev Lett 82(21) (1999) 4288-4291.

[168] J.M. De Teresa, A. Barthelemy, A. Fert, J.P. Contour, F. Montaigne, P. Seneor, Role of metal-oxide interface in determining the spin polarization of magnetic tunnel junctions, Science 286(5439) (1999) 507-509.
[169] C.R. Zhu, G. Wang, B.L. Liu, X. Marie, X.F. Qiao, X. Zhang, X.X. Wu, H. Fan, P.H. Tan, T. Amand, B. Urbaszek, Strain tuning of optical emission energy and polarization in monolayer and bilayer MoS2, Phys Rev B 88(12) (2013).
[170] H.J. Conley, B. Wang, J.I. Ziegler, R.F. Haglund, S.T. Pantelides, K.I. Bolotin, Bandgap Engineering of Strained Monolayer and Bilayer MoS2, Nano Lett 13(8) (2013) 3626-3630.
[171] S.G. Sarwat, M. Tweedie, B.F. Porter, Y. Zhou, Y. Sheng, J. Mol, J. Warner, H. Bhaskaran, Revealing Strain-Induced Effects in Ultrathin Heterostructures at the Nanoscale, Nano Lett 18(4) (2018) 2467-2474.
[172] R.X. Fei, L. Yang, Strain-Engineering the Anisotropic Electrical Conductance of Few-Layer Black Phosphorus, Nano Lett 14(5) (2014) 2884-2889.
[173] C.W. Bark, D.A. Felker, Y. Wang, Y. Zhang, H.W. Jang, C.M. Folkman, J.W. Park, S.H. Baek, H. Zhou, D.D. Fong, X.Q. Pan, E.Y. Tsymbal, M.S. Rzchowski, C.B. Eom, Tailoring a two-dimensional electron gas at the LaAlO3/SrTiO3 (001) interface by epitaxial strain, P Natl Acad Sci USA 108(12) (2011) 4720-4724.
[174] M.R. Falvo, G.J. Clary, R.M. Taylor, V. Chi, F.P. Brooks, S. Washburn, R. Superfine, Bending and buckling of carbon nanotubes under large strain, Nature 389(6651) (1997) 582-584.
[175] A. Ohtomo, H.Y. Hwang, A high-mobility electron gas at the LaAlO3/SrTiO3 heterointerface, Nature 427(6973) (2004) 423-426.
[176] J.P. Locquet, J. Perret, J. Fompeyrine, E. Machler, J.W. Seo, G. Van Tendeloo, Doubling the critical temperature of La1.9Sr0.1CuO4 using epitaxial strain, Nature 394(6692) (1998) 453-456.
[177] S.J. May, J.W. Kim, J.M. Rondinelli, E. Karapetrova, N.A. Spaldin, A. Bhattacharya, P.J. Ryan, Quantifying octahedral rotations in strained perovskite oxide films, Phys Rev B 82(1) (2010).
[178] A. Vailionis, H. Boschker, W. Siemons, E.P. Houwman, D.H.A. Blank, G. Rijnders, G. Koster, Misfit strain accommodation in epitaxial ABO(3) perovskites: Lattice rotations and lattice modulations, Phys Rev B 83(6) (2011).
[179] J. Chakhalian, A.J. Millis, J. Rondinelli, Whither the oxide interface, Nat Mater 11(2) (2012) 92-94.
[180] J.J. Huang, A. Gellatly, A. Kauffmann, X. Sun, H.Y. Wang, Exchange Bias Effect along Vertical Interfaces in La0.7Sr0.3 MnO3:NiO Vertically Aligned Nanocomposite Thin Films Integrated on Silicon Substrates, Cryst Growth Des 18(8) (2018) 4388-4394.
[181] X.M. Ma, Z.L. Liao, L. Li, P. Gao, Atomic Structure and Chemistry of Self-Assembled Nanopillar Composite Oxides, Adv Mater Interfaces 4(13) (2017).
[182] H. Yang, H.Y. Wang, J. Yoon, Y.Q. Wang, M. Jain, D.M. Feldmann, P.C. Dowden, J.L. MacManus-Driscoll, Q.X. Jia, Vertical Interface Effect on the Physical Properties of Self-Assembled Nanocomposite Epitaxial Films (vol 21, pg 3794, 2009), Adv Mater 21(40) (2009) 3969-3969.
[183] S. Gupta, R. Ranjit, C. Mitra, P. Raychaudhuri, R. Pinto, Enhanced room-temperature magnetoresistance in La0.7Sr0.3MnO3-glass composites, Appl Phys Lett 78(3) (2001) 362-364.
[184] F. Yang, N. Kemik, M.D. Biegalski, H.M. Christen, E. Arenholz, Y. Takamura, D. E., Strain engineering to control the magnetic and magnetotransport properties of La0.67Sr0.33MnO3 thin films, Appl Phys Lett 97(9) (2010) 092503.

[185] F. Tsui, M.C. Smoak, T.K. Nath, C.B. Eom, M.A. J., L.P. B., S.B. I., Strain-dependent magnetic phase diagram of epitaxial La0.67Sr0.33MnO3 thin films, Appl Phys Lett 76(17) (2000) 2421-2423.
[186] H.L. Ju, K.M. Krishnan, D. Lederman, Evolution of strain-dependent transport properties in ultrathin La0.67Sr0.33MnO3 films, J Appl Phys 83(11) (1998) 7073-7075.
[187] H.Y. Hwang, S.W. Cheong, P.G. Radaelli, M. Marezio, B. Batlogg, Lattice Effects on the Magnetoresistance in Doped Lamno3, Phys Rev Lett 75(5) (1995) 914-917.
[188] H.S. Wang, E. Wertz, Y.F. Hu, Q. Li, D.G. Schlom, Role of strain in magnetotransport properties of Pr(0.67)Sr(0.33)MnO(3) thin films, J Appl Phys 87(10) (2000) 7409-7414.
[189] J.R. Petrie, H. Jeen, S.C. Barron, T.L. Meyer, H.N. Lee, Enhancing Perovskite Electrocatalysis through Strain Tuning of the Oxygen Deficiency, J Am Chem Soc 138(23) (2016) 7252-7255.
[190] C. Becher, L. Maurel, U. Aschauer, M. Lilienblum, C. Magen, D. Meier, E. Langenberg, M. Trassin, J. Blasco, I.P. Krug, P.A. Algarabel, N.A. Spaldin, J.A. Pardo, M. Fiebig, Strain-induced coupling of electrical polarization and structural defects in SrMnO3 films, Nat Nanotechnol 10(8) (2015) 661-665.
[191] J.R. Petrie, C. Mitra, H. Jeen, W.S. Choi, T.L. Meyer, F.A. Reboredo, J.W. Freeland, G. Eres, H.N. Lee, Strain Control of Oxygen Vacancies in Epitaxial Strontium Cobaltite Films, Adv Funct Mater 26(10) (2016) 1564-1570.